



**GPR INVESTIGATION AT THE ARCHAEOLOGICAL SITE OF PLASI,  
ATTIKI, GREECE**

**TEODORA BLAGOEVA**

Thesis submitted for the obtainment of a  
**Bachelor Degree in Geology and Geoenvironment**

**Supervisor:** Assist. Prof. Dr. Ioannis Alexopoulos

**JULY 2020**

**ATHENS**

## Acknowledgements

*“The possession of knowledge does not kill the sense of wonder and mystery. There is always more mystery.”*

— Anais Nin

I would like to start by thanking my supervisor Prof. Ioannis Alexopoulos for passing on to me his knowledge and experience, whilst also guiding me in this project. This study would not have been possible if it wasn't for his advice and support, the information he provided and the skills in the field that he helped me acquire.

I would also like to thank Prof. Nikolaos Voulgaris for his support and for the technical expertise he provided by managing and processing the huge amounts of data that were acquired. His help was crucial to this project and its end results.

Special thanks to Prof. Giannis Papadatos, who manages the university's excavation site at Plasi, Marathon. The access to the site, the supporting information and documents he provided about the study area and its history were essential for developing this survey.

I also deeply appreciate the help and guidance provided by Dr. Spiridonas Dilalos, geologist-geophysicist (MSc). His knowledge and experience had a significant impact on this study, not only during field measurements, but also during the processing of the data and evaluation of the end results.

I would also like to acknowledge the work of the whole team that worked together so hard on this project and thank them deeply for their cooperation and patience during the fieldwork measurements. This team includes geologist Georgia Mitsika, master student, and my fellow students Thanos Petras, Ioanna Panagiotopoulou, Giannis Giannopoulos and Nikos Vitopoulos.

Last, but not least, I would like to express my endless gratitude and appreciation to my family and loved ones who have supported me in every way possible throughout this journey.

## Abstract

The archaeological site of Plasi, property of the university's Department of History and Archaeology, is situated in the municipality of Marathon. Excavations at the site started in 1970 aiming to find the extent of the ancient remains, which proved to have a significant time range dating from the end of the Neolithic era (3.500-3.000 BC) to the Roman period (31BC-324AD). The excavations were renewed in 2014 and later, in 2018, a collaboration was formed between the Department of History and Archaeology and the Department of Geology and Geoenvironment to advise site-selection for future excavation and unravel the remains hidden beneath the surface.

A Ground Penetrating Radar (GPR) survey was conducted near an existing excavation at the site in order to deduce potential continuation of the current findings and to map the possible structure of the remains. The data was acquired during the period June-September 2019. It was then processed and analyzed to create 2D horizontal slices (radargrams), fence diagrams and 3D volume-depth slices in order to interpret the data and assert the location of possible archaeological remains of interest. The survey showed the existence of numerous anomalies that could depict the continuity of the actual findings but an expansion of the excavation site is needed to ensure this theory.

## Περίληψη

Ο αρχαιολογικός χώρος του Πλάσι, ιδιοκτησία του Τμήματος Ιστορίας και Αρχαιολογίας του ΕΚΠΑ, βρίσκεται στον δήμο Μαραθώνα. Οι ανασκαφές στον χώρο ξεκίνησαν το 1970 με σκοπό να βρουν την έκταση των αρχαίων λειψάνων, τα οποία αποδείχτηκαν να έχουν σημαντική χρονική εξάπλωση που χρονολογείται από το τέλος της Νεολιθικής εποχής (3.500-3.000π.Χ.) έως τη Ρωμαϊκή περίοδο (31π.Χ.-324μ.Χ.). Οι ανασκαφές ανανεώθηκαν το 2014 και αργότερα, το 2018, δημιουργήθηκε συνεργασία μεταξύ του Τμήματος Ιστορίας και Αρχαιολογίας και του Τμήματος Γεωλογίας και Γεωπεριβάλλοντος με σκοπό την παροχή συμβουλών για την επιλογή τοποθεσίας μελλοντικών ανασκαφών με αποτέλεσμα να αποκαλυφθούν τα αρχαιολογικά κατάλοιπα κρυμμένα κάτω από την επιφάνεια.

Πραγματοποιήθηκε μια έρευνα χρησιμοποιώντας τη μέθοδο γεωραντάρ (Ground Penetrating Radar) κοντά σε εκσκαφή με ήδη υπάρχοντα ευρήματα με σκοπό να μελετηθεί η πιθανή συνέχειά τους και να χαρτογραφηθεί η πιθανή δομή των λειψάνων. Τα δεδομένα αποκτήθηκαν κατά την περίοδο Ιουνίου-Σεπτεμβρίου 2019. Στη συνέχεια, υποβλήθηκαν σε επεξεργασία και αναλύθηκαν για τη δημιουργία δισδιάστατων οριζόντιων τομών (ραδιογραφήματα) και τρισδιάστατων οριζοντιογραφιών όγκου-βάθους για την ερμηνεία των δεδομένων και την εξακρίβωση της θέσης των πιθανών αρχαιολογικών υπολειμμάτων. Η έρευνα έδειξε την ύπαρξη πολυάριθμων ανωμαλιών που θα μπορούσαν να απεικονίσουν τη συνέχεια των πραγματικών ευρημάτων, αλλά απαιτείται επέκταση του χώρου ανασκαφής για να διασφαλιστεί αυτή η θεωρία.

## Table of Contents

|  |      |
|--|------|
| Acknowledgements .....                               | i    |
| Abstract .....                                       | ii   |
| Περίληψη.....  | iii  |
| List of Figures.....                                 | vi   |
| List of Tables.....                                  | vii  |
| Abbreviations .....                                  | viii |
| 1. Introduction.....                                 | 1    |
| 1.1. Background.....                                 | 1    |
| 1.2. Study Area .....                                | 1    |
| 1.2.1. Location .....                                | 1    |
| 1.2.2. Geology.....                                  | 3    |
| 1.2.3. Archaeological History.....                   | 4    |
| 2. Ground Penetrating Radar (GPR) .....              | 6    |
| 2.1. Introduction.....                               | 6    |
| 2.1.1. Basic operation .....                         | 6    |
| 2.1.2. Brief historical evolution .....              | 7    |
| 2.1.3. Current applications .....                    | 8    |
| 2.2. Basic principles and laws .....                 | 8    |
| 2.2.1. Maxwell's equations.....                      | 9    |
| 2.2.2. Constitutive equations .....                  | 10   |
| 2.2.3. Velocity, attenuation and impedance .....     | 11   |
| 2.2.4. Refraction, reflection and transmission ..... | 13   |
| 2.3. Equipment and data acquisition parameters.....  | 17   |
| 2.3.1. Antennas.....                                 | 17   |
| 2.3.2. Data acquisition parameters .....             | 19   |
| 2.4. Data processing .....                           | 22   |
| 2.4.1. Dewow.....                                    | 22   |
| 2.4.2. Background removal.....                       | 23   |
| 2.4.3. Bandpass frequency .....                      | 24   |
| 2.4.4. Time zero correction .....                    | 25   |
| 2.4.5. Spectral whitening.....                       | 26   |
| 2.4.6. Deconvolution .....                           | 27   |
| 2.4.7. Migration.....                                | 27   |

|        |                                   |    |
|--------|-----------------------------------|----|
| 2.4.8. | Hilbert transform (Envelope)..... | 28 |
| 2.5.   | Data representation .....         | 29 |
| 3.     | Data Acquisition .....            | 30 |
| 3.1.   | Equipment .....                   | 30 |
| 3.2.   | Methodology .....                 | 30 |
| 3.3.   | Measurement parameters .....      | 33 |
| 4.     | Data Processing .....             | 34 |
| 4.1.   | 2D radargram sections .....       | 34 |
| 4.1.1. | Subtract-mean (dewow).....        | 34 |
| 4.1.2. | Background removal.....           | 34 |
| 4.1.3. | Bandpass frequency .....          | 35 |
| 4.1.4. | Start time correction .....       | 35 |
| 4.1.5. | Spectral whitening.....           | 36 |
| 4.1.6. | Deconvolution .....               | 36 |
| 4.1.7. | F-k migration (Stolt).....        | 36 |
| 4.1.8. | Envelope .....                    | 36 |
| 4.2.   | Volume-depth slices .....         | 37 |
| 5.     | Results and Conclusions .....     | 39 |
|        | References.....                   | 48 |
|        | Additional Bibliography .....     | 50 |
|        | Appendix.....                     | 51 |

## List of Figures

|  |    |
|--|----|
| <b>Figure 1. 1:</b> Map of the Marathon municipality.....  | 2  |
| <b>Figure 1. 2:</b> Satellite image of the Marathon municipality .....   | 2  |
| <b>Figure 1. 3:</b> Drone image of the archaeological site of Plasi.....   | 3  |
| <b>Figure 1. 4:</b> Geological map of the Marathon basin area .....  | 4  |
| <b>Figure 1. 5:</b> Image from the 1970 site excavations .....   | 5  |
|  |    |
| <b>Figure 2. 1:</b> Visual display of GPR basic operation .....  | 6  |
| <b>Figure 2. 2:</b> Visual representation of the different forms of presenting GPR collected data ...                                      | 7  |
| <b>Figure 2. 3:</b> Visualization of the data acquisition process.....   | 7  |
| <b>Figure 2. 4:</b> Visual representation of Maxwell’s equations.....  | 10 |
| <b>Figure 2. 5:</b> Alteration of the velocity and attenuation in a simple medium with non-<br>dispersive physical properties .....        | 12 |
| <b>Figure 2. 6:</b> Visualization of wave refraction due to a subsurface discontinuity .....   | 14 |
| <b>Figure 2. 7:</b> Image depicting the two vector-field components (TE & TM) that Em waves are<br>comprised.....                          | 16 |
| <b>Figure 2. 8:</b> Visualization of EM wave transmission.....   | 16 |
| <b>Figure 2. 9:</b> Different shapes of antennas.....  | 17 |
| <b>Figure 2. 10:</b> Visualization of signal transmission of an antenna.....   | 18 |
| <b>Figure 2. 11:</b> Antennas frequently used in geoarchaeological surveys.....  | 19 |
| <b>Figure 2. 12:</b> Image depicting an example of survey lines at a study area .....  | 22 |
| <b>Figure 2. 13:</b> Image of a raw reflection profile (radargram) .....   | 22 |
| <b>Figure 2. 14:</b> Visualization of the dewow filter .....   | 23 |
| <b>Figure 2. 15:</b> Radargram before and after applying the background removal filter.....  | 24 |
| <b>Figure 2. 16:</b> Reflection profile before and after the application of bandpass frequency filter<br>.....                             | 24 |
| <b>Figure 2. 17:</b> Selection of the bandpass frequency filtering parameters.....   | 25 |
| <b>Figure 2. 18:</b> Example of time zero correction selection done on an individual trace .....   | 26 |
| <b>Figure 2. 19:</b> Comparison of the effect on a radargram of a bandpass filter and of a spectral<br>whitening filter .....              | 26 |
| <b>Figure 2. 20:</b> The effects of the deconvolution filter .....   | 27 |
| <b>Figure 2. 21:</b> Visualization of how hyperbola reflections derive.....  | 28 |
| <b>Figure 2. 22:</b> Examples of migration.....  | 28 |
| <b>Figure 2. 23:</b> Example of a Hilbert transform (envelope) on radargram.....   | 29 |
| <b>Figure 2. 24:</b> Image depicting the different forms of GPR data representation .....  | 30 |
|  |    |
| <b>Figure 3. 1:</b> Map that shows the excavation next to the study area and the grid of GPR lines<br>that was chosen for this study ..... | 31 |
| <b>Figure 3. 2:</b> Images from the data acquisition process .....   | 32 |
| <b>Figure 3. 3:</b> Measuring GPS coordinates of the start and end point of the GPR lines .....  | 33 |
|  |    |
| <b>Figure 4. 1:</b> Example of a raw reflection profile (up) and the result of applying dewow (down)<br>.....                              | 34 |
| <b>Figure 4. 2:</b> The results of applying background removal (down) after the dewow filter (up)  | 35 |

|   |    |
|---|----|
| <b>Figure 4. 3:</b> The top reflection profile corresponds to the background removal filter, whilst the middle is the result of bandpass frequency application and the bottom has start time correction. .... | 35 |
| <b>Figure 4. 4:</b> The effect of spectral whitening on the radargram (up) followed by the result of deconvolution applied to it (down).....  | 36 |
| <b>Figure 4. 5:</b> Application of the migration filter on the data (up) and finally the envelope filter (down) .....   | 37 |
| <b>Figure 4. 6:</b> Diagram showing the distribution of the envelope amplitude with depth .....   | 38 |
| <b>Figure 4. 7:</b> 20-30cm Volume-depth slice .....  | 38 |
| <br>  |    |
| <b>Figure 5. 1:</b> Fence diagram of the reflection profiles recorded in the NE direction .....   | 39 |
| <b>Figure 5. 2:</b> Fence diagram of the reflection profiles recorded in the SE direction.....  | 40 |
| <b>Figure 5. 3:</b> Fence diagram of the radargrams recorded in both NE and SE directions.....  | 41 |
| <b>Figure 5. 4:</b> 10-20cm Volume-depth slice .....  | 42 |
| <b>Figure 5. 5:</b> 20-30cm Volume-depth slice .....  | 43 |
| <b>Figure 5. 6:</b> 30-40cm Volume-depth slice .....  | 44 |
| <b>Figure 5. 7:</b> 40-50cm Volume-depth slice .....  | 45 |
| <b>Figure 5. 8:</b> 50-60cm Volume-depth slice .....  | 46 |

## List of Tables

|   |    |
|---|----|
| <b>Table 1:</b> Exemplary dielectric constant (K), electrical conductivity ( $\sigma$ ), velocity (v) and attenuation (a) of known geological materials ..... | 13 |
| <b>Table 2:</b> Examples of maximum depth penetration depending on the center frequency .....   | 19 |
| <b>Table 3:</b> Exemplary time windows according to the desired depth and type of material the signal penetrates .....  | 20 |
| <b>Table 4:</b> Typical sampling intervals according to the center frequency .....  | 20 |
| <b>Table 5:</b> Description of the parameters used for GPR data acquisition.....  | 33 |

## Abbreviations

**GPR:** Ground penetrating radar

**GPS:** Ground positioning system

**EM:** Electromagnetic

**TE:** Transverse electric field

**TM:** Transverse magnetic field

# 1. Introduction

## 1.1. Background

The Ground Penetrating Radar (GPR) method is a non-destructive remote sensing geophysical method which uses pulses of electromagnetic (EM) 'radar' waves that penetrate the ground. The electromagnetic fields are used to probe lossy dielectric materials to detect structures and changes in the material properties within the materials (Davis & Annan, 1989). When the wave encounters an obstacle with different properties a part of it reflects back to the surface and its characteristics (amplitude, wavelength, travel time) are recorded for further analysis. The inclusion of geophysical analysis within geological and archaeological studies has occurred more recently and is becoming to make an impact in many research projects (Campana & Piro, 2009).

The survey in this report concentrates on processing and analyzing the data acquired at the archaeological site of Plasi in the municipality of Marathon. The location of the survey was chosen in close proximity to an existing excavation which unraveled the existence of ancient wall remains. The data was acquired during the period July-September 2019 using a shielded antenna with a center frequency of 250MHz. A total of 72 GPR profiles were recorded in both X (NE) and Y (SE) directions with a profile separation of 0,5m. The collected data was then processed using ReflexW by Sandmeier.

## 1.2. Study Area

### 1.2.1. Location

The archaeological site of Plasi, as mentioned above, is situated in the municipality of Marathon, which is part of the eastern region of Attica. The Marathon municipality is bordered with Grammatiko on the north, Nea Makri on the south and on the east of the municipality are Kapandriti and Stamata. The excavation site is situated in close proximity to the coastline, in the center of the Marathon plain, more specifically, between the riverbed of the Haradros stream on the east and the Skoupa stream on the west, both branches of the Inois river (Figures 1 & 2). It is also worth mentioning that the site is in remarkable closeness to two of the most famous archaeological sites in the area: the Marathon Tomb (1,5km NE) and the Trophy of the Battle of Marathon (2km SW).

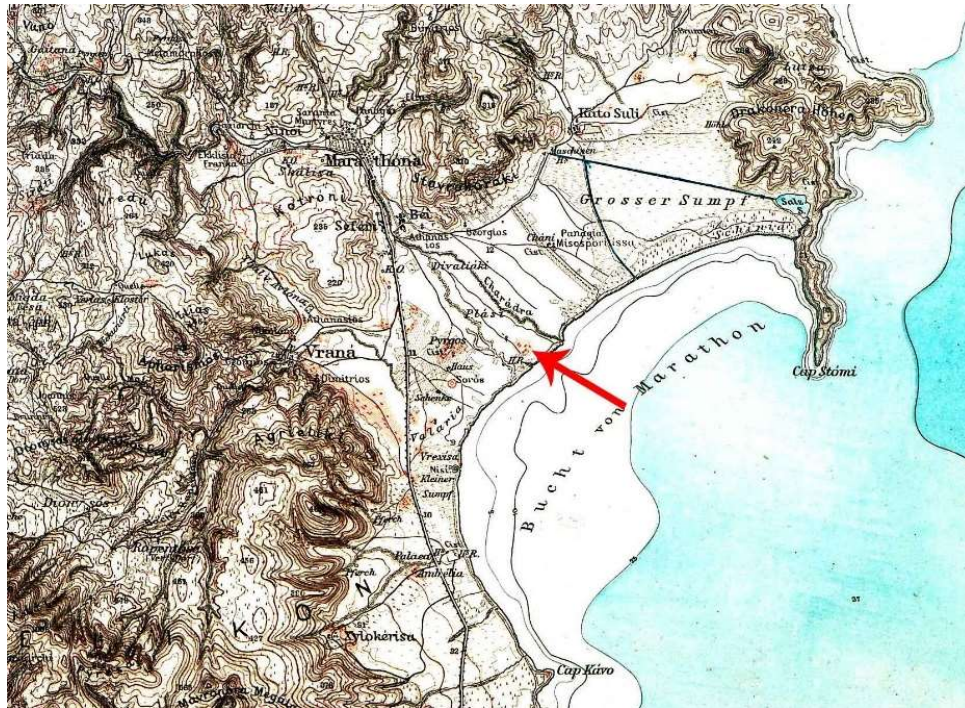


**Figure 1. 1:** Map of the Marathon municipality. The red arrow indicates the location of the Plasi site  
 (Source: Curtius-Kaupert 1881)

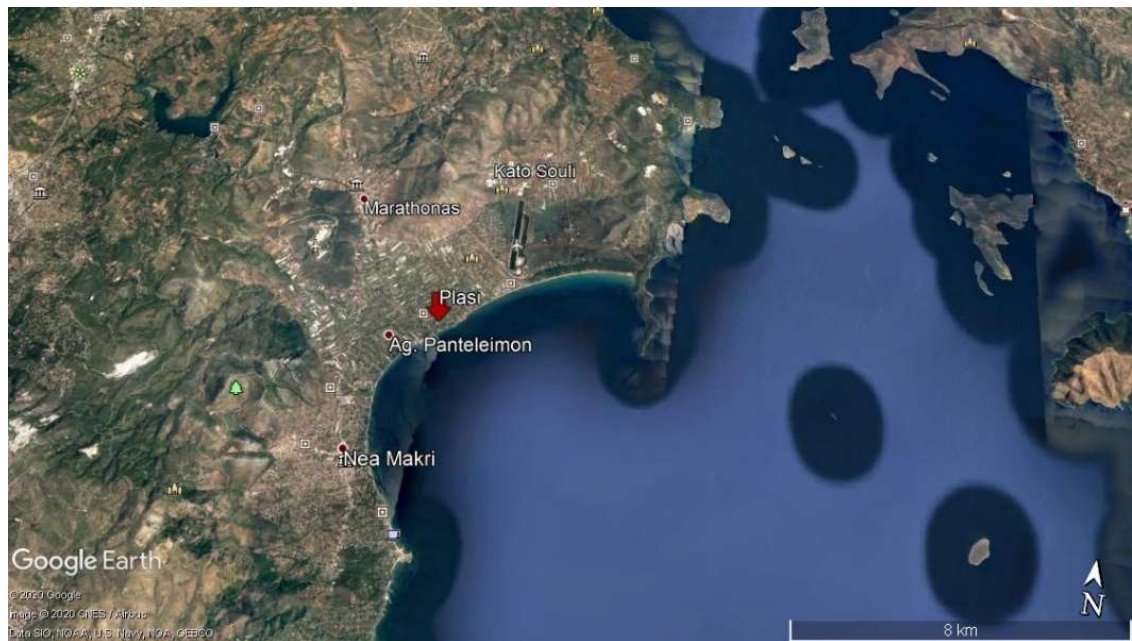


**Figure 1. 2:** Satellite image of the Marathon municipality. The red arrow indicates the location of the Plasi site  
 (Source: Google Earth)



**Figure 1. 3:** Drone image of the archaeological site of Plasi. The areas marked with a black dashed line indicate the existing excavations. The area marked with a red dashed line indicate the location of the study area in this project

### 1.2.2. Geology

The geological background of the area is commonly characterized as complex (Bodechtel & Papadeas, 1968, Lozios, 1993). In general, the Marathon area and the one surrounding it is part of the NE Attica zone. This zone is described as a “relatively autochthonous” metamorphic sequence (Lozios, 1993), which can be identified by a post-volcanic-sedimentary sequence at its base (L. Triassic and older) followed by a carbonate sequence in the middle part (L. Triassic – L. Cretaceous), comprised mostly of different phases of marble, and meta-flysch rocks in the upper part (Eocene). According to Lozios (1993) the metamorphic sequence contains marbles (E. Cretaceous), schists (M. Cretaceous), marbles (L. Cretaceous) and schists (Jurassic).

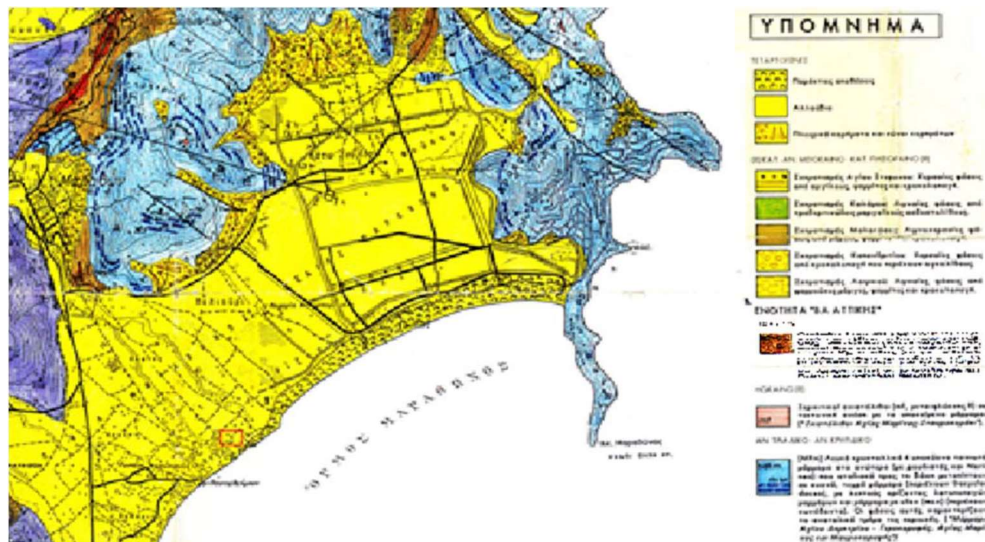


Figure 1. 4: Geological map of the Marathon basin area (Source: Lozios, 1993)

A considerable part of the area, including the study area, is covered with Post-Alpine (Quaternary) formations. These formations consist mainly of clastic sediments that are a result of aggradation from the Inois river. These sediments extend along the coastline (Figure 1.3) in a SW-NE direction with a length of approximately 8,5km and 2,5km of width measured from the shoreline inwards. These can be distinguished into four major groups (Lozios, 1993):

- Alluvial deposits (Holocene) – brown clayey-sandy materials with scattered gravel-sized clasts and terra rossa
- Talus slopes (Pleistocene) – also comprised of alluvial deposits of brownish-red color
- Terrestrial deposits (Pleistocene) – old deposits of terra rossa and fine-grained materials from older talus slopes
- Lacustrine deposits (Middle-Upper Miocene)

### 1.2.3. Archaeological History

The Plasi excavation site was first established in 1970 by Euthimios Mastrokostas and Spiridonas Marinatos. It was found unintentionally, but turned out to offer abundant artefacts from a wide range of periods. Altogether 8 different occupation phases were identified. The oldest ancient objects found were ceramics from the Neolithic era (3.500-3.000 BC). Following this era, artefacts were found covering the full extent of the Bronze Age:

- 1) Early Bronze Age (3.000-2.000 BC) attested by building and fortification remains
- 2) Middle Bronze Age (2.000-1.700 BC) attested by a large construction, a ceramic kiln and buildings (Figure 1.4)
- 3) Late Bronze Age (1.700-1.600 BC) attested by a burial ground with casket-shaped tombs (Figure 1.4)
- 4) Mycenaean Period (last phase of the Bronze Age 1.400-1.200 BC) attested by construction remains

Findings from the Geometric period follow with Protogeometric style house remains (1.100-900 BC) and tombs (900-700 BC). From the Archaic period (700-480 BC) the boundaries of a sanctuary were found. Also, different building remains and ceramics were found from the Classical Greek period (480-323 BC), the Hellenistic period (323-31 BC), the Roman period (31 BC-324 AD) and the Early Christian period (324 AD).



α. Πλάσι. Τὸ «ἀνάκτορον» ἐκ ΝΑ.· εἰς τὸ μέσον ὄρατος μέγας κιβωτόσχημος τάφος· εἰς τὸ βάθος ἄνω δεξιᾷ κεῖται ὁ κεραμεικὸς κλίβανος.

*Figure 1. 5: Image from the 1970 site excavations showing part of the burial ground and the ceramic kiln on the right in the background (Source: <http://www.arch.uoa.gr>)*

These findings were of great importance, since they confirm the continuous existence of human settlements throughout time. The results of the excavation were never thoroughly studied, but the land was purchased for further exploration.

The excavation site of Plasi was reestablished in 2014 with the intention of uncovering the initial findings so they can be systematically studied and organized. This action resulted in confirming some of the previous findings, but also questioning the accuracy of part of them and the discovery of new remains.

It is important to mention that the excavation site near the study area is comprised of wall remains that are thought to be part of a fortification structure. The linear artefacts vary in width from 0.20-1.00m and their main direction of extension is SW-NE and NW-SE. These archaeological remains are considered to represent the Copper Age (Chalcolithic), although no ceramics from that period were found to solidify this theory.

## 2. Ground Penetrating Radar (GPR)

### 2.1. Introduction

There are a number of factors that need to be taken in consideration before overtaking a GPR survey. In order to do so, one has to be able to understand the basic operation of the method, the science behind it and the way GPR has evolved over the last decades. This will not only help for better understanding the physical principles, but it is also imperative for a successful survey.

#### 2.1.1. Basic operation

The Ground penetrating radar (GPR) is a remote-sensing geophysical method that is rather contemporary, or at least in terms of the degree of application. It is favored for its non-destructive nature, its utilization on a variety of materials, range of depth and its ability to cover large study areas for a short amount of time and at a lower cost (Dojack, 2012). The method essentially utilizes electromagnetic (EM) waves to explore the subsurface. These radio waves are emitted from a transmitter with a specific central frequency. When the EM wave encounters a change in the physical and/or chemical properties of the materials it penetrates, which affect the dielectric properties of the given material, the wave is modified and a part of it reflects to the surface where it is recorded by a receiver (Figure 2.1)(Annan, 2009). The data is recorded in the form of traces or A-scans (Figure 2.2a), each of which represent the total waveform of all waves collected at one surface location (Dojack, 2012). When data is recorded along a continuous line, that creates an array of A-scans, also called a B-scan (Figure 2.2b), which can produce a variety of images that display the anomalies found in the material in the vertical and horizontal dimensions (Figure 2.3) (Annan, 2009, Conyers, 2004).

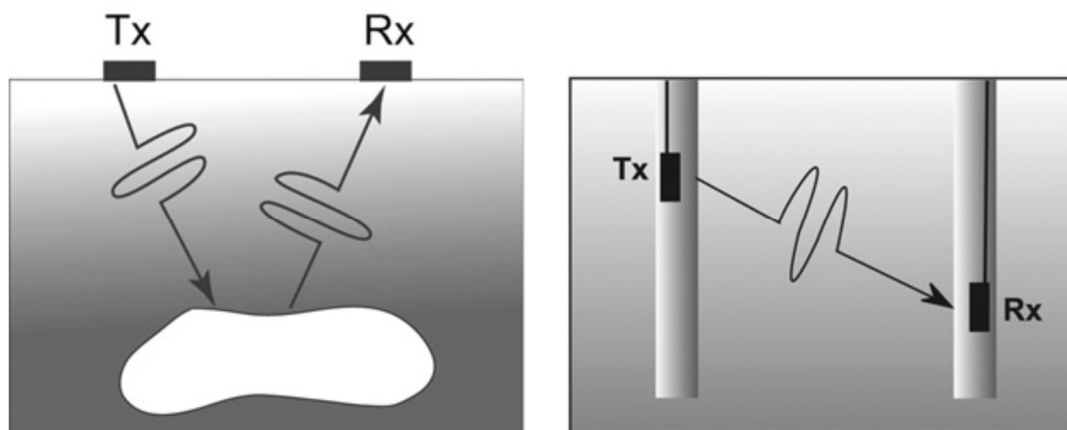


**Figure 2. 1:** Visual display of GPR basic operation. The first is more common, using a transmitter (Tx) that emits the EM waves, and a receiver (Rx), that records the energy of the wave reflected back from an object. The second example represents the same principle, except it measures the energy transmitted through the material, without encountering any obstacles (Source: Annan,2009)

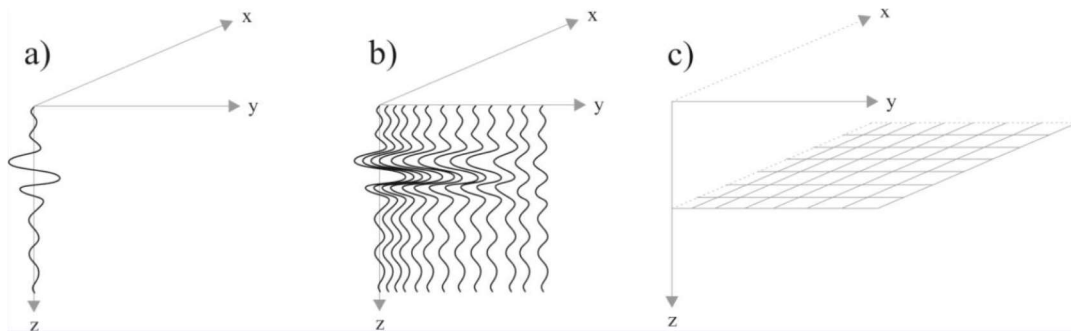


**Figure 2. 2:** Visual representation of the different forms of presenting GPR collected data. a) represents a single trace or waveform called an A-scan b) represents consecutive traces that were recorded along a continuous line and is called a B-scan c) represents a horizontal layer in the data that has a fixed position on the z-axis and is called a C-scan (Source: Bendetto et al., 2017)

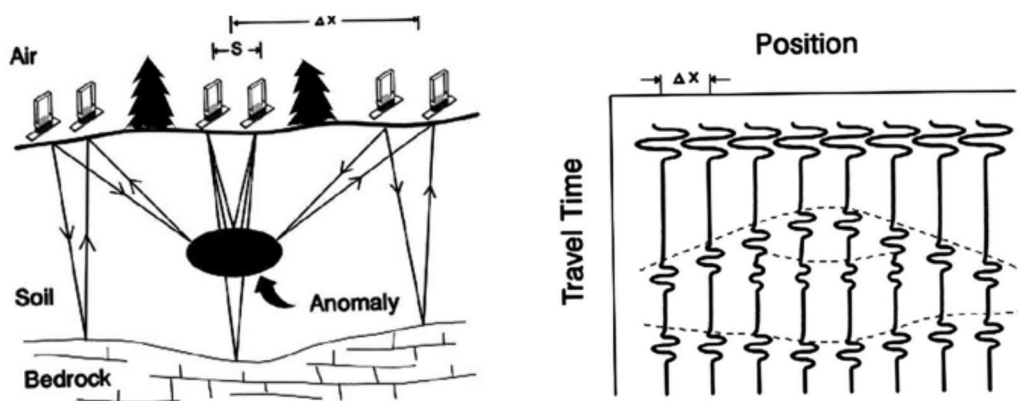


**Figure 2. 3:** Visualization of the data acquisition process. In the first image we can see the path of the transmitted wave and the path of the wave that reflects off of obstacles. The second image depicts the data that the receiver records, a multitude of traces along a line, the sum of which generates a cross sectional image of the data, or B-scan (Source: Annan, 2003)

### 2.1.2. Brief historical evolution

The study of radio wave dispersion dates all the way back to the 1900s. During that time and until 1950 there is evidence of research on the subject, but no account for conducting measurements that survey the ground (Annan, 2003). The first record of someone undertaking the task of using EM waves to assess subsurface characteristics was in 1956 and it consisted of calculating the depth of a water table (El Said, 1956). In the early 1960s studies were taken further, by using radio waves to scan polar ice sheets and glaciers (Waite & Shmidt, 1961, Bailey et al., 1964, Bentley, 1964, Walford, 1964). Interest in the GPR method started to grow over the next decade. In 1974 the first GPR manufacturer emerged, called Geophysical Survey Systems Inc. (Morey, 1974). Knowledge on the method started expanding and with it its applications. In 1978 the first experiments of testing radio waves in an archaeological site were made (Dolphin et al., 1978). During the 1980s new equipment manufacturers appeared and the application span expanded. Some of the new fields the method was incorporated in include road investigations, tunnel detection in military areas, land contamination and soil classification (Annan, 2003). But it was not until the 1990s that the GPR method blossomed. The knowledge of the method grew and so did the development of new and more complex technology, two factors paved the road to colossal progress. New equipment was produced, that was more reliable and more user-friendly. The world of programming also played a significant role by developing programs and software for managing the big amounts of data,

processing the results and reproducing them in 2D and 3D images. By applying these innovations to study cases in all the fields previously mentioned, perception and results were improved.

### 2.1.3. Current applications

Since the beginning of its development, the ground penetrating radar method has gone a long way. Originally, the use of GPR was established upon surveying natural geological materials, but presently it is thought to be equally efficient on human-made materials such as wood, concrete and asphalt (Annan, 2009). Today, it can essentially be used to explore any hidden objects in the subsurface, given that the conditions meet the method's requirements. Some of these requirements include: 1) the lack of metal objects in the ground, since they would reflect radio waves completely and obscure anything beneath them; 2) the objects that are targeted in the study must have different EM properties from their surrounding environment; 3) the existence of an adequate antenna frequency in order to achieve the detection of the depth and size of the target that is sought; 4) the lack of moisture and water, as they affect the measurements and are a cause of deception (Utsi, 2017). Nevertheless, these requirements are not as restrictive as it may seem and for that reason the application span remains substantial. Nowadays, the GPR method is most frequently applied in:

- 1) Environmental studies, such as:
  - a) Soils, peatlands and biomonitoring (Doolittle & Butnor, 2009)
  - b) Water resource research (Slater & Comas, 2009)
  - c) Contaminant mapping (Redman, 2009)
- 2) Earth science studies, such as:
  - a) Aeolian dune sands (Bristow, 2009)
  - b) Coastal environments (Buynevich, Jol & FitzGerald, 2009)
  - c) Glaciers and ice sheets (Arcone, 2009)
- 3) Engineering and societal applications, such as:
  - a) Transportation (roads and bridge deck) (Saarenketo, 2009, Utsi, 2017)
  - b) Security (Utsi, 2017)
  - c) Structural engineering (Utsi, 2017)
  - d) Landmine and unexploded ordnance (Yarovoy, 2009, Utsi, 2017)
  - e) Archaeometry (Goodman, Piro, et al., 2009, Conyers, 2016)
  - f) Forensics (Utsi, 2017)

For the purpose of this study, the main focus will be the use of GPR in Archaeometry. For this reason the remaining above-mentioned applications will not be analyzed further. For additional information on the subject see references.

## 2.2. Basic principles and laws

The fundamentals of the GPR method can be described by the electromagnetic theory. In order to understand the physics behind electromagnetic phenomena, Maxwell's equations provide the mathematical model to describe electric and magnetic fields. Whereas to perceive the affect that external forces, such as EM fields, have on different materials the constitutive equations best describe and quantify that affect (Annan, 2009). In addition, because of the wave nature of the EM fields, wave propagation on surfaces dividing different mediums also constitutes an essential part of understanding GPR.

### 2.2.1. Maxwell's equations

James Maxwell was a physicist and mathematician who used a group of separate known laws, which assembled together came to be the very base of how electric and magnetic fields interact, propagate and the affect other objects have on them. The mathematical equations that describe this concept are:

$$\nabla \cdot \bar{D} = q \quad (2.1) \text{ Gauss' Law}$$

$$\nabla \cdot \bar{B} = 0 \quad (2.2) \text{ Gauss' Law of Magnetism}$$

$$\nabla \times \bar{E} = -\frac{\partial \bar{B}}{\partial t} \quad (2.3) \text{ Faraday's Law}$$

$$\nabla \times \bar{H} = \frac{\partial \bar{D}}{\partial t} + \bar{J} \quad (2.4) \text{ Ampere's Law}$$

Where:

$\bar{D}$  – electric displacement vector (C/m<sup>2</sup>)

$q$  – electric charge density (C/m<sup>3</sup>)

$\bar{B}$  – magnetic flux density vector (T)

$\bar{E}$  – electric field strength vector (V/m)

$\bar{H}$  – magnetic field intensity vector (A/m)

$\bar{J}$  – electric current density vector (A/m<sup>2</sup>)

To comprehend in a more uncomplicated manner what these laws represent an explanation is required. Gauss' law is essentially based on the fact that charges of the same sign repel each other and on the contrary, charges of the opposite sign attract each other. In other words, the divergence (measure of how fields flow away or towards an object) of an electric field (electric displacement vector) around a point is equal to its electric charge density. For example, if there is a small positive charge this indicates that the electric field goes away from the charge (Figure 2.4a) and if there is a small negative charge this means that the electric field moves towards the charge. If a charge does not exist, then the divergence is also zero and a field distribution is not possible. The second law, Gauss' law of magnetism, states that the divergence of the magnetic flux density equals zero, which indicates that an isolated magnetic charge does not exist, therefore magnetic monopoles by themselves do not attract or repel each other (Figure 2.4b). Faraday's law indicates that the curl (measure of how fields wrap around an object) of the electric field strength vector equals the time rate of change of the magnetic flux density vector. This implies that if a magnetic field changes through time (through a loop) it is going to generate an electric field that spins around it and vice versa (Figure 2.4c). The last law, Ampere's law, states that the curl of the magnetic field intensity vector is equal to the sum of the time rate of the electric displacement vector and the electric current density vector. This confirms that a flowing electric current density vector is capable of generating a magnetic field that rotates around it (Figure 2.4d). The same statement is true for an electric flux density vector that changes through time, that is, it also generates a magnetic field that circles the electric field. These four laws were proven by experiments, but it was Maxwell who unified them and connected the dots, forming the origins of the

electromagnetic theory. These equations are also evidence that light is an EM wave, therefore it acts in accordance with the laws of optics.

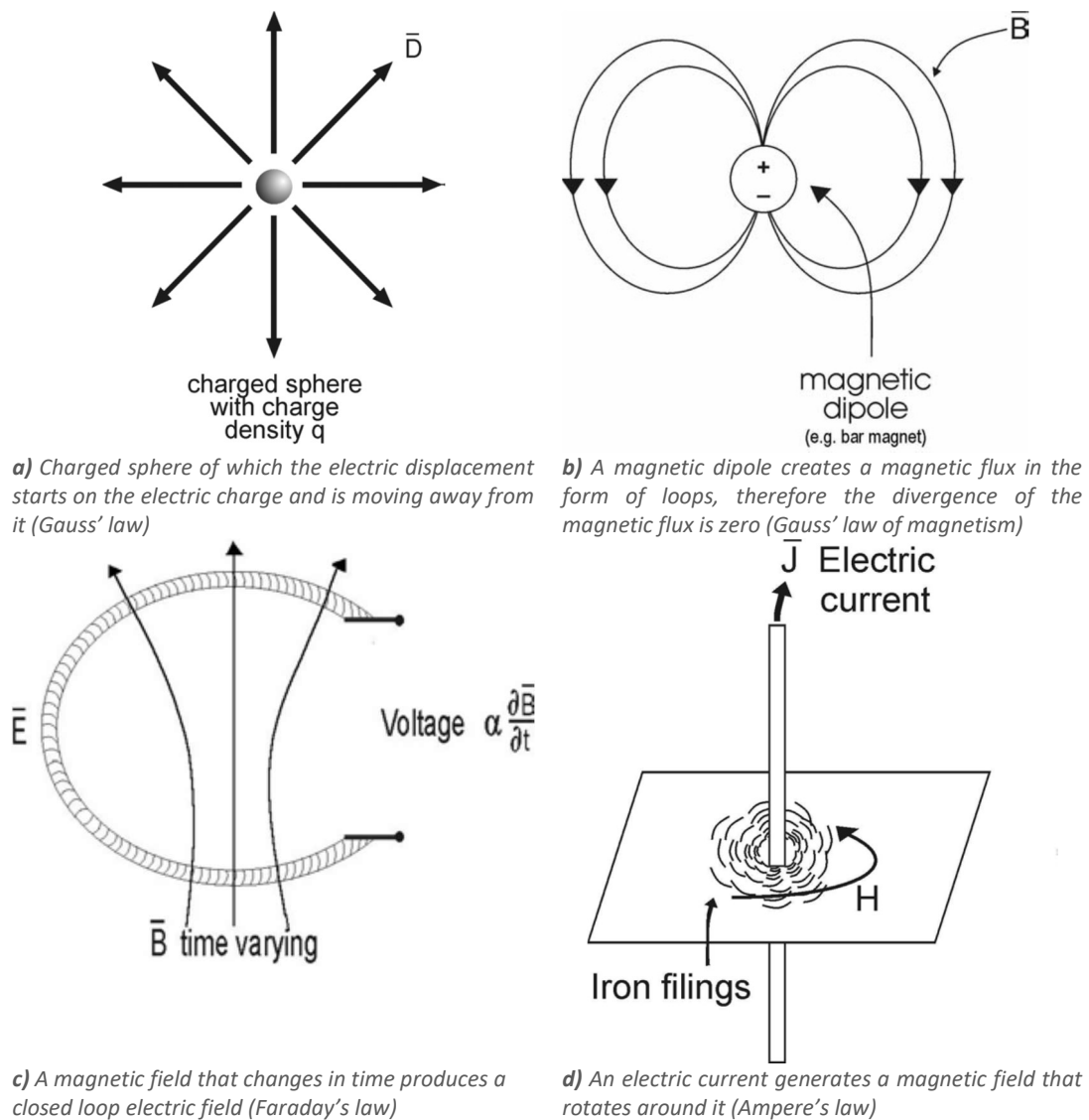


Figure 2. 4: Visual representation of Maxwell's equations (Source: Annan, 2003)

### 2.2.2. Constitutive equations

The constitutive equations basically represent physical quantities that measure the reaction of a material that is exposed to an external force, such as a field, and they are unique for each material. The equations relevant for understanding GPR are the following:

$$\vec{J} = \sigma \vec{E} \tag{2.5}$$

$$\vec{D} = \epsilon \vec{E} \tag{2.6}$$

$$\vec{B} = \mu \vec{H} \tag{2.7}$$

Where:

$\tilde{\sigma}$  - electric conductivity

$\tilde{\epsilon}$  - dielectric permittivity

$\tilde{\mu}$  – magnetic permeability

Electric conductivity can be described as the capacity of a material to conduct an external electrical current. It quantifies how strongly the charge of the current is capable of flowing through a certain material. Therefore, for high values of  $\sigma$  the electrical current is “captured” in that material, impeding it to go any further. On the contrary, lower values aid energy dissipation (Annan, 2009), allowing the electrical current to penetrate deeper.

Dielectric permittivity quantifies the ability of a material to get polarized by an applied electric field. Polarization is a phenomenon that is caused by the displacement of charge in a way that forms an electric dipole. High values of  $\epsilon$  mean that the material is more prone to polarization, therefore it is capable of storing bigger amounts of energy, preventing energy dissipation. Dielectric permittivity is associated with another quantity, which is more commonly used in GPR, called the relative dielectric permittivity (RDP) or dielectric constant:

$$K = \frac{\epsilon}{\epsilon_0} \quad (2.8)$$

Where  $\epsilon_0$  is the permittivity of vacuum ( $8.89 \times 10^{-12}$  F/m)

The dielectric constant is a useful tool in GPR because it can be used to determine the wavelength and wave velocity in a certain material. The equation that associates these quantities is:

$$K = \left(\frac{c}{v}\right)^2 \quad (2.9)$$

Where:

$v$  – wave velocity in a certain material (m/ns)

$c$  – speed of light equal to 0.2998 m/ns

From the equation (2.9) it can be concluded that for high values of  $K$  the wave velocity would appear to have lower values and accordingly a smaller wavelength. Practically, this means that the RDP can be used to estimate the depth of penetration of EM waves.

Magnetic permeability measures the capability of a material to get magnetized by an induced magnetic field. Magnetization is the equivalent term for polarization, accordingly it describes the formation of magnetic dipole moments. Respectively, high values of permeability define materials that are susceptible to magnetization, which as a result obstructs signal penetration.

### 2.2.3. Velocity, attenuation and impedance

Given the wave nature of radar waves, some of the fundamental properties of wave propagation include velocity ( $v$ ), attenuation ( $\alpha$ ) and impedance ( $Z$ ) (Annan, 2003). Mathematically these quantities can be described by the following equations:

$$v = \frac{1}{\sqrt{\epsilon \cdot \mu}} \quad (2.10)$$

$$\alpha = \sqrt{\frac{\mu}{\varepsilon}} \cdot \frac{\sigma}{2} \quad (2.11)$$

$$Z = \sqrt{\frac{\mu}{\varepsilon}} \quad (2.12)$$

All these features are dependent on the specific properties of a given material. The velocity of wave propagation is mainly determined by the dielectric permittivity and magnetic permeability of a material. Attenuation is a term used to express the gradual loss of energy of a wave after it has passed through a component with different properties. It is measured according to the dielectric permittivity, magnetic permeability and conductivity of a material. Impedance is another quantity used to measure the resistance of a certain material to an electric charge flow when an external electric field is applied. These wave properties are easily described if we consider that the conductivity, permittivity and permeability are fixed quantities for a given medium and that the wave varies in time in the form of a sine wave (Annan, 2009). The alteration of the velocity and attenuation depending on the frequency ( $f$ ) can be seen in Figure 2.5.

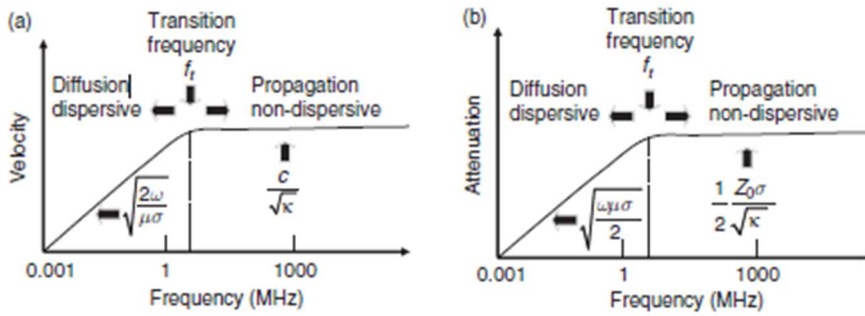


**Figure 2. 5:** Alteration of the velocity and attenuation in a simple medium with non-dispersive physical properties (where  $\omega=2\pi f$ ,  $c$  and  $Z_0$  are the velocity and impedance in vacuum) (Source Annan, 2009)

Figure 2.5 also displays the behavior of wave properties. For low frequencies, they are determined by the value of the angular frequency ( $\sqrt{\omega}$ ), which leads to diffusion. For higher frequencies, frequency no longer determines the wave properties, instead they are dependent on the relative permittivity and electrical conductivity, which leads to wave propagation (Annan, 2009). Achieving wave propagation is one of the main goals of GPR, therefore calculating the limit between diffusion and propagation, also called transition frequency ( $f_t$ ) plays a significant role. Mathematically the transition frequency can be defined in the following manner:

$$f_t = \frac{\sigma}{2\pi\varepsilon} \quad (2.13)$$

Above this frequency, the velocity and attenuation maintain a fixed value, meaning that propagation is achievable without dispersion (Annan, 2009). In this case, the previously mentioned equations  $v$ ,  $\alpha$  and  $Z$  can be reshaped in the following way:

$$v = \frac{c}{\sqrt{\kappa}} \quad (2.14)$$

$$\alpha = Z_0 \cdot \frac{\sigma}{2 \cdot \sqrt{\kappa}} \quad (2.15)$$

$$Z = \frac{Z_0}{\sqrt{\kappa}} \quad (2.16)$$

Where:

$c$  - speed of light equal to 0.2998 m/ns

$Z_0$  – impedance of free space equal to 377  $\Omega$

**Table 1:** Exemplary dielectric constant ( $\kappa$ ), electrical conductivity ( $\sigma$ ), velocity ( $v$ ) and attenuation ( $\alpha$ ) of known geological materials (Source: Annan, 2003)

| Material        | $\kappa$ | $\sigma$<br>(mS/m) | $v$<br>(m/ns) | $\alpha$<br>(dB/m) |
|-----------------|----------|--------------------|---------------|--------------------|
| Air             | 1        | 0                  | 0.30          | 0                  |
| Distilled water | 80       | 0.01               | 0.033         | $2 \times 10^{-3}$ |
| Fresh water     | 80       | 0.5                | 0.033         | 0.1                |
| Sea water       | 80       | $3 \times 10^3$    | 0.01          | $10^3$             |
| Dry sand        | 3-5      | 0.01               | 0.15          | 0.01               |
| Saturated sand  | 20-30    | 0.1-1.0            | 0.06          | 0.03-0.3           |
| Limestone       | 4-8      | 0.5-2.0            | 0.12          | 0.4-1.0            |
| Shales          | 5-15     | 1-100              | 0.09          | 1-100              |
| Silts           | 5-30     | 1-100              | 0.07          | 1-100              |
| Clays           | 5-40     | 2-1000             | 0.06          | 1-300              |
| Granite         | 4-6      | 0.01-1.0           | 0.13          | 0.01-1.0           |
| Dry salt        | 5-6      | 0.01-1.0           | 0.13          | 0.01-1.0           |
| Ice             | 3-4      | 0.01               | 0.16          | 0.01               |

#### 2.2.4. Refraction, reflection and transmission

The main purpose of conducting a GPR survey is to collect data of reflected wave signals in order to determine the location of a desired object. For that reason, it is crucial to understand how EM waves move through mediums with different properties. In this section the laws of refraction, reflection and transmission will be discussed. Only the basic concepts needed to understand GPR operation will be explained.

The term refraction refers to the phenomenon where a signal is transmitted in a medium and it encounters a discontinuity, or in other words, a medium with different properties, and part of the wave is reflected back to the surface, while another part of it penetrates the second medium changing its direction of propagation due to differences in properties. This process is best described mathematically by Snell's law. Snell's law states that a plane wave propagating in medium 1, with propagation vector  $k_1$ , will reach the discontinuity with an angle of incidence  $\vartheta_1$ . When the wave continues its course in medium 2, with propagation vector  $k_2$ , the propagation angle must change to  $\vartheta_2$ , also known as the refraction angle (Figure 2.6). Furthermore, this law asserts that the horizontal component of the propagation vector should be equal for each medium, which gives the origins of the equations:

$$k_1 \cdot \sin \theta_1 = k_2 \cdot \sin \theta_2 \quad (2.17)$$

$$v_2 \cdot \sin \theta_1 = v_1 \cdot \sin \theta_2 \quad (2.18)$$

Where:

$k$  – wave propagation vector

$v$  – wave propagation velocity

In addition, when the propagation velocity of the wave in medium 1 is greater than the propagation velocity of the wave in medium 2 and the angle of incidence is big enough, this may cause the phenomenon known as critical refraction, meaning that the wave will refract in medium 2 with a refraction angle  $\vartheta_2 = 90^\circ$ , therefore parallel to the discontinuity. The angle  $\vartheta_1$  in the case where  $\vartheta_2 = 90^\circ$  is also known as the critical angle ( $\vartheta_c$ ) and it describes the value of the angle of incidence beyond which only reflection of the wave is possible.

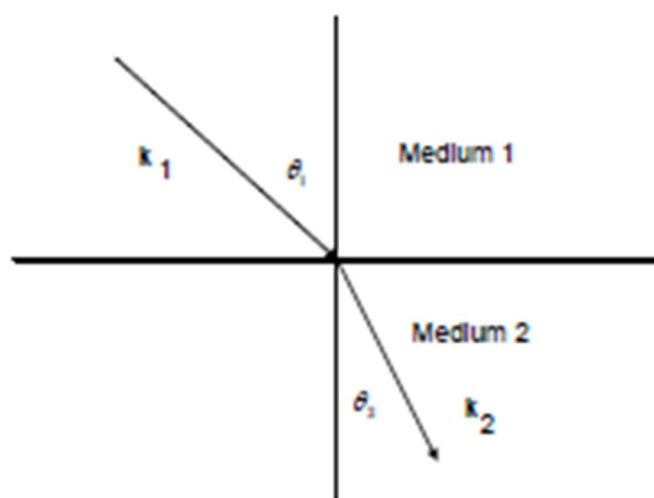


**Figure 2. 6:** Visualization of wave refraction due to a subsurface discontinuity  
(Source: Annan, 2003)

To understand the importance of the concept of refraction in GPR it helps to visualize medium 1 as air (the gap between the antenna and the ground) and medium 2 as the ground that will be investigated. Wave propagation velocity in air will always be larger than the wave propagation velocity of the explored environment, as a result of which the signal will penetrate the ground in a more vertical manner (Annan, 2003).

The principles of reflection and transmission of electromagnetic waves can be easily described mathematically by the Fresnel coefficients (Annan, 2003). They aim to explain and estimate the changes in amplitude of an EM field as it encounters discontinuities in its path. When a vector-field wave comes across a flat surface it can be divided into two vector components, called transverse electric field (TE) and transverse magnetic field (TM) (Figure 2.7). By doing so, the Fresnel coefficients of reflection ( $R$ ) and transmission ( $T$ ) can be related in the following way:

$$I + R \cdot I = T \cdot I \quad (2.19)$$

Where:

$I$  – field strength

$R$  – reflected field

$T$  – transmitted field

This equation is applied for each vector-field separately, due to the different behavior of TE and TM fields. Additionally, in order to estimate R and I some requirements need to be satisfied, such as Snell's law, the TE and TM fields need to be continuous along the surface and the electric current and magnetic flux density need to be equal on each side of the discontinuity. When these are fulfilled, the following equations for the reflection and transmission coefficients derive:

$$R_{TE} = \frac{Y_1 \cdot \cos \theta_1 - Y_2 \cdot \cos \theta_2}{Y_1 \cdot \cos \theta_1 + Y_2 \cdot \cos \theta_2} \quad (2.20)$$

$$R_{TM} = \frac{Z_1 \cdot \cos \theta_1 - Z_2 \cdot \cos \theta_2}{Z_1 \cdot \cos \theta_1 + Z_2 \cdot \cos \theta_2} \quad (2.21)$$

$$T_{TE} = 1 + R_{TE} \quad (2.22)$$

$$T_{TM} = 1 + R_{TM} \quad (2.23)$$

Where:

$Y_i$  – admittance of the material ( $Y_i = 1/Z_i$ )

$Z_i$  – impedance of the material

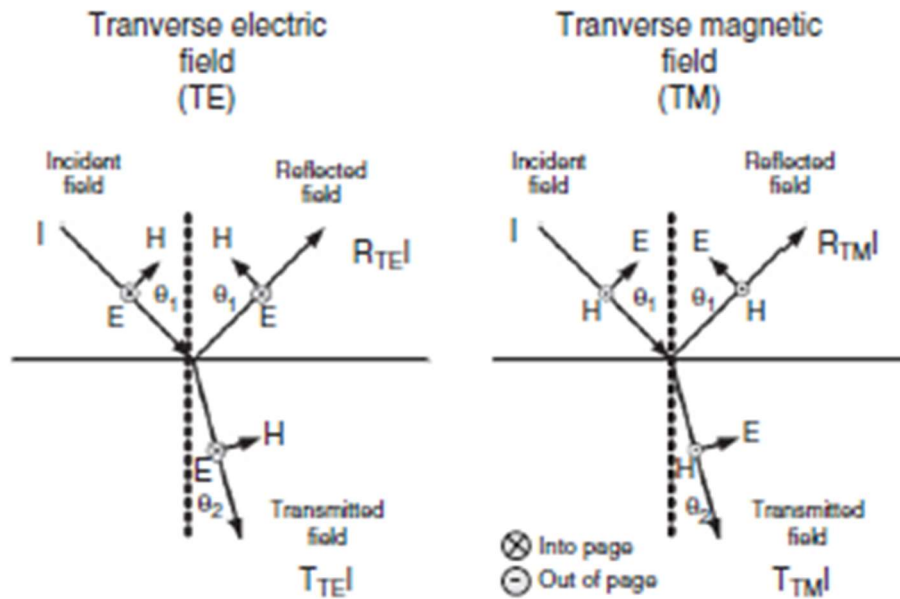


Figure 2. 7: Image depicting the two vector-field components (TE & TM) that EM waves are comprised of and their behavior once they encounter a planar discontinuity (Source Annan, 2009)

When referring to EM transmission it is also necessary to call attention to wave transmission from the antenna. The antenna emits radio signals in the form of a cone (Figure 2.8) which expands as the signal penetrates deeper into the subsurface (Conyers, 2004). The size and shape of the cone in which the waves are transmitted varies depending mainly on the properties of the subsurface and the center frequency of the antenna. The consequence of the cone-shaped signal propagation is the formation of an area between recordings where no data is acquired (Figure 2.8), also known as the shadow zone. It is an important factor to take in consideration during data acquisition, which will be determined by the target of the study.

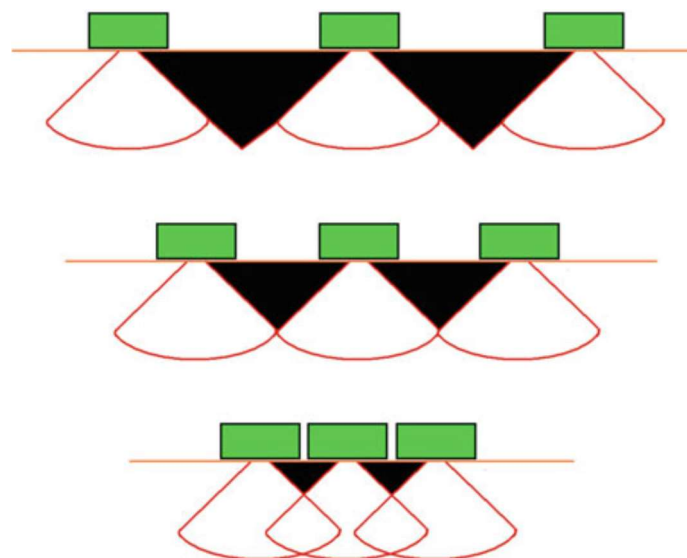


Figure 2. 8: Visualization of EM wave transmission from the antenna in the form of a cone and of the shadow zone that is formed between recordings (Source: Goodman & Piro, 2013)

## 2.3. Equipment and data acquisition parameters

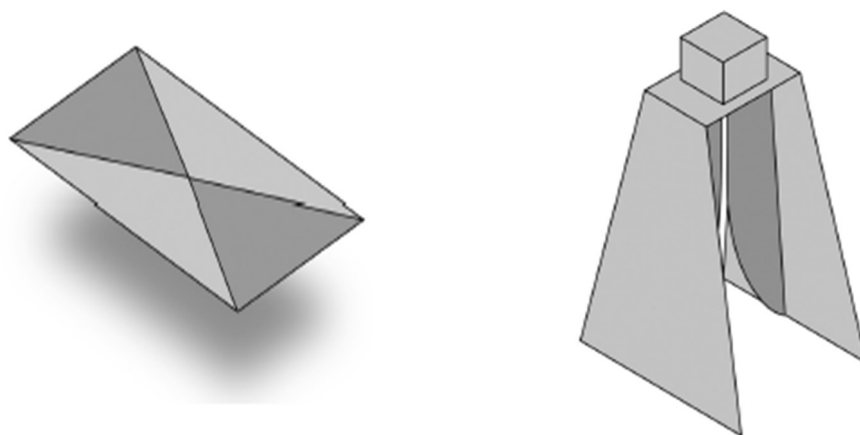
The key to a successful GPR study lies in the proper design of the survey. This includes mainly the selection of the right equipment, more specifically the ideal antenna frequency for the specific purpose, and the appropriate data acquisition parameters, also regarding the specific target.

### 2.3.1. Antennas

Antennas may come in different shapes and sizes and though their design does not concern the person using it, it is important to understand their operation considering that it may influence the data acquisition process.

Primarily, antennas can be categorized into monostatic and bistatic. A normal GPR consists of one transmit antenna and one receive antenna. When the same antenna has the function of a transmitter, as well as a receiver the system is described as monostatic. These types of systems are convenient in terms of size, since they require only one antenna. Another advantage of the system is that the data does not require correction caused by the gap between the transmitter and the receiver, because it is non-existent. A disadvantage is that the system functions at a slower pace, due to the inherent delay in time it takes for the antenna to adjust its function from a transmitter to a receiver (Utsi, 2017). Bistatic systems are comprised of two separate antennas that operate accordingly as a transmitter and as a receiver, thus affecting the size of the system, which tends to be bigger. As opposed to the monostatic systems, they do not have a built-in time delay which results in faster performance. Despite this advantage, the data does require the correction due to the gap between antennas previously mentioned.

Antennas can also be categorized according to their shape. The shape of the antenna affects the transmission of the signal, in an attempt to minimize any unwanted secondary effects on the signal. The most frequently used shapes are bowties, horns and snakes (Utsi, 2017). The bowtie shaped antenna is usually preferred for ground-coupled systems, hence the plane shape of its design (Figure 2.9a). It has no limitations referring to different frequencies. The horn antenna (Figure 2.9b) is usually used in surveys that require signal travelling through air. It is commonly designed for utilization in regard of higher frequencies (>1GHz) (Utsi, 2017). Lastly, snake antennas are intended for low-frequency studies. Their shape is prolonged and slim with the intention of dealing with difficult terrain.



a) *Bowtie shaped antenna*

b) *Horn shaped antenna*

**Figure 2. 9:** Different shapes of antennas (Source: Utsi, 2017)

Another significant type of antenna classification involves shielding. Ideally, the signal that is transmitted from the antenna would be restricted to the direction and area it is appointed to, but wave radiation is not linear. Instead, waves are emitted in all directions (Figure 2.10). Depending on the environment, this phenomenon could interfere significantly with the results of the recorded data. This created the necessity to design a “shield” that would limit the emission of EM waves only in the desirable direction. As a result, a new category of antennas emerged: shielded and unshielded. The advantages of the shielded antennas include maximizing the energy transmitted in the desirable direction, minimizing the diversion of the signal into the air and minimizing the impact of external noise on the recorded data. Despite these benefits, in some cases the shield could prove to be unfavorable. There is always the possibility that the shield does not fully enclose the antenna, as a result some waves could flow through it. In some circumstances, if the study area is secluded and not much noise pollution is possible, maximum penetration depth could be achieved without the use of a shield (Annan, 2003).

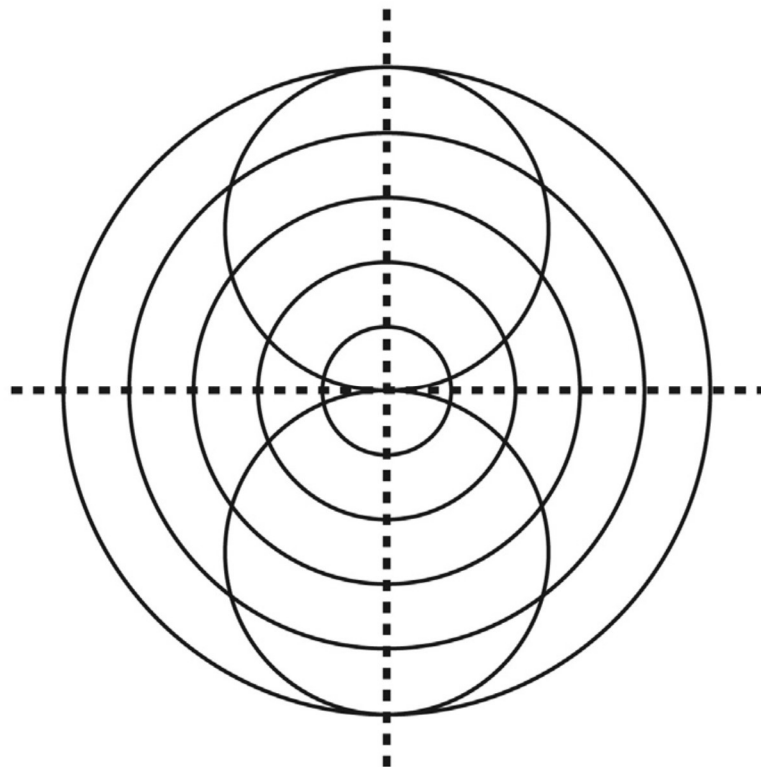


*Figure 2. 10:* Visualization of signal transmission of an antenna (Source: Utsi, 2017)

Another category of antennas and the most crucial for a survey is in regards to their center frequency. Nowadays, GPR antennas exist with center frequencies ranging from 10-1000MHz. The center frequency ( $f_c$ ) is the main factor that determines the maximum depth penetration and the resolution of the recorded data (Table 2). It is important to point out that the energy the antenna transmits is not confined to the center frequency, considering that GPR emits in broad band. The real range of transmission frequencies is typically between one half and two times the  $f_c$ .

**Table 2:** Examples of maximum depth penetration depending on the center frequency (Source: Annan, 2003)

| Depth (m) | Center frequency (MHz) |
|-----------|------------------------|
| 0.5       | 1000                   |
| 1.0       | 500                    |
| 2.0       | 200                    |
| 7.0       | 100                    |
| 10.0      | 50                     |
| 30.0      | 25                     |
| 50.0      | 10                     |

In geoarchaeological surveys the most frequently used antennas propagate radar waves in center frequencies ranging from 10-900 MHz (Figure 2.11). The high-frequencies antenna, such as the 900 MHz, provide the best resolution, but are restrictive in terms of depth, therefore they are only good for shallow targets (Conyers, 2016). As the frequency of the antenna decreases, the propagation depth increases, but the resolution also decreases. This is why it is important to have a clear background of the target that is being explored.



**Figure 2. 11:** Antennas frequently used in geoarchaeological surveys (Source: Conyers, 2016)

### 2.3.2. Data acquisition parameters

Data acquisition parameters can be classified into two major groups. The first group includes input parameters concerning the equipment that will be used for the survey. These involve the time window, the sampling interval, samples per trace, the step size and stacking. Nowadays, many GPR systems have these parameters built-in, but it is important to understand the role they play when data is collected. The second group includes transect planning, which consists of transect spacing and orientation. Both groups are completely dependent on the application and mainly the dimensions and depth of the target that is being inspected. The adequate estimation of these parameters is essential in order to achieve the best resolution of data and successfully locate the hidden object.

- 1) The **time window ( $W$ )** can be described as the total time that is needed for the receiver to collect two-way travel time data. According to Conyers (2004) the minimum value should be equal to the time that is needed for the signal to reach the

maximum desired depth. Annan (2003) suggests that a more precise estimation could be achieved using the expression:

$$W = 1.3 \frac{2d}{v} \quad (2.24)$$

Where:

$W$  – length of time window (ns)

$d$  – maximum desired depth (m)

$v$  – minimum wave propagation velocity (m/ns)

**Table 3:** Exemplary time windows according to the desired depth and type of material the signal penetrates (Source: Adopted from Annan, 2003)

| Depth (m) | Rock | Wet Soil | Dry Soil |
|-----------|------|----------|----------|
| 0.5       | 12   | 24       | 10       |
| 1         | 25   | 50       | 20       |
| 2         | 50   | 100      | 40       |
| 5         | 120  | 250      | 100      |
| 10        | 250  | 500      | 200      |
| 20        | 500  | 1000     | 400      |
| 50        | 1250 | 2500     | 1000     |
| 100       | 2500 | 5000     | 2000     |

- 2) The **sampling interval ( $t$ )** can be defined as the amount of time between two points on a recorded waveform. This time interval should act in accordance with the Nyquist frequency concept, meaning that its maximum value should not surpass half the period of the highest frequency signal (Annan, 2003). Its value can be estimated using the equation:

$$t = \frac{1000}{6f_c} \quad (2.25)$$

Where:

$t$  – sampling interval (ns)

$f_c$  – center frequency (MHz)

**Table 4:** Typical sampling intervals according to the center frequency (Source: Adopted from Annan, 2003)

| Antenna Center Frequency (MHz) | Maximum Sampling Interval (ns) |
|--------------------------------|--------------------------------|
| 10                             | 16.70                          |
| 20                             | 8.30                           |
| 50                             | 3.30                           |
| 100                            | 1.67                           |
| 200                            | 0.83                           |
| 500                            | 0.33                           |
| 1000                           | 0.17                           |

- 3) The **samples per trace ( $S$ )** term characterizes the number of samples (recorded pulses) necessary to create a single reflected waveform (Conyers, 2004). This specification is relevant for the resolution of the collected data, the bigger the amount of samples per trace, the better the resolution of the recorded trace. Usually, high-frequency

antennas demand a higher number of samples per trace (Conyers, 2004), which would also suggest a bigger time window interval, since the two parameters are codependent (Equation 2.26). The number of samples per trace can be estimated by using the relationship:

$$S = \frac{W}{t} \quad (2.26)$$

Where:

$S$  – samples per trace

$W$  – time window (ns)

$t$  – sampling interval (ns)

- 4) The **step size**, also known as the spatial sampling interval, defines the distance between consecutive trace recordings along the selected line. This parameter depends mainly on the center frequency of the antenna and the relative permittivity of the explored mediums. According to Annan (2003) the step size should not exceed the Nyquist sampling interval:

$$\Delta x = \frac{c}{4f_c\sqrt{K}} = \frac{75}{f_c\sqrt{K}} \text{ (in m)} \quad (2.27)$$

Where:

$f_c$  – antenna center frequency (MHz)

$K$  – relative dielectric permittivity

This criteria needs to be fulfilled especially in circumstances where the target is not parallel to the ground (Annan, 2003). It is safe to say that a smaller step size provides better resolution, but it must be noted that it increases the data volume, as well as the recording time.

- 5) **Stacking** is a term used to define the number of repetitive recordings (stacks) the GPR system completes at the same position, in order to assert the average waveform, thus increasing the quality and resolution of the data. The higher the number of stacks, the better the resolution, but this also slows down the data acquisition process. Usually the number of stacks is 4, 16, 32 and 64 (Dojack, 2012).
- 6) **Transect spacing** is the distance between the consecutive GPR lines (Figure2.12). The selection of said distance is important not only for the resolution of the collected data, but also for detecting the dimensions of the target. As previously mentioned, the GPR transmits signal in the shape of a cone (Figure2.8), therefore if the targets are small and the distance between transects too big, discovering the target might be impossible. For that reason, the depth and dimensions of the sought target need to be taken in consideration if they are known in advance. Surveys that were conducted to test the quality of different transect spacing, show that a spacing of 0.5m and less is more suitable for accurate subsurface exploration (Neubauer et al., 2002, Orlando, 2017).
- 7) **Transect orientation** is the direction of the transects that is chosen (Figure2.12) and it is as important as transect spacing for the same reasons. Studies have shown that when exploring prolonged targets (i.e. buried walls) it is important that the direction of the GPR lines is perpendicular to the object in order to measure more accurately its location and dimensions (Neubauer et al., 2002, Orlando, 2017).

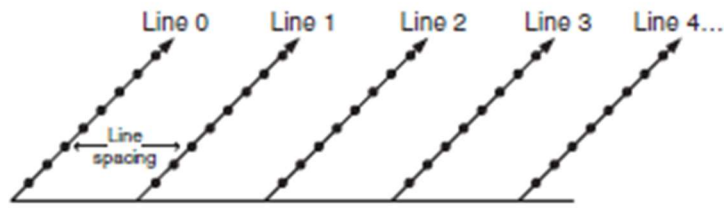


Figure 2. 12: Image depicting an example of survey lines at a study area (Source: Annan, 2009)

## 2.4. Data processing

Processing the recorded GPR data is an inevitable and necessary step with the sole purpose of enhancing the recorded signal and minimizing external noise, so it can be displayed in a manner that can be interpreted. This is not an easy endeavor, due to the fact that every survey is unique and has its own requirements. Most commonly the processing procedure is based on experience, nevertheless it is an unwritten guideline that the fewer filters applied to the data, the better (Utsi, 2017). In this section only the most frequently applied filters will be described in order to understand the effect they have on data. As previously mentioned, the display of GPR data can be done in several ways (Figure 2.2), but the most common way is in the form of a B-scan. This type of presentation is also known as a reflection profile or radargram and is the primary data output file of GPR systems (Figure 2.13). The initial radargram is a raw (unedited) version of the signal response. It is from this point onward that the editing process begins. The existing filters are applied to each trace individually or to the entire profile. The most prevalent filters include dewow, background removal, bandpass frequency, start time correction, spectral whitening, deconvolution, migration and Hilbert transform (Annan, 2009, Dojack, 2012, Goodman & Piro, 2013, Utsi 2017).

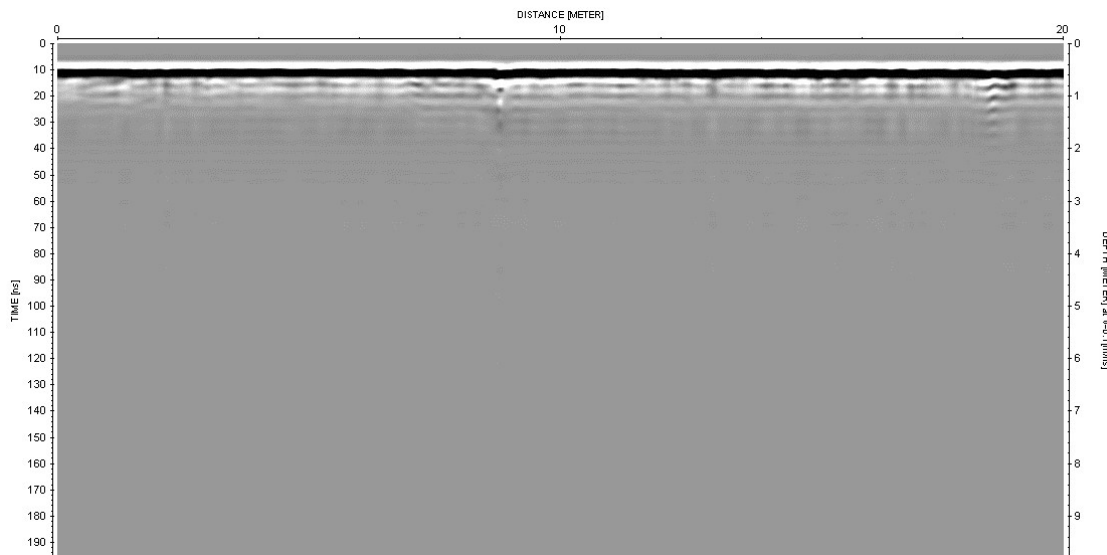
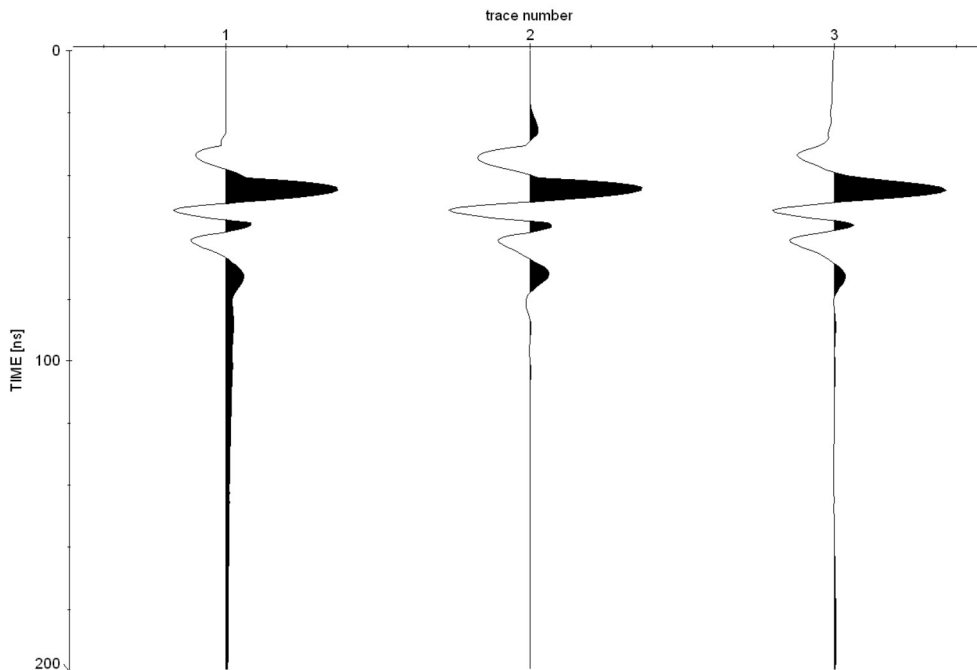


Figure 2. 13: Image of a raw reflection profile (radargram)

### 2.4.1. Dewow

A significant part of GPR data contains a considerable amount of very low-frequency energy as a result of inductive fields or even equipment restrictions (Sandmeier). This energy can be easily recognized in a trace, as it appears as a continuous disruption either below or above the

trace's baseline (Figure 2.14). This signal is also known as the “wow” effect (Annan, 2009). One of the first steps in processing radargrams is removing it, hence the “dewow” filter. The application of this filter is done on each trace individually and within the time domain. First it estimates a running mean value for each value of each trace, which is then subtracted from the central point (Sandmeier). This results in clearing away the unwanted low-frequency energy (Figure 2.14).



**Figure 2. 14:** Visualization of the dewow filter. The first signal displays the raw (unedited) trace; the second trace is the result after applying the dewow filter; the third trace is the result of an applied bandpass filter (Source: Sandmeier)

#### 2.4.2. Background removal

It is a common phenomenon of constant noise infiltrating the raw reflection profiles. This type of noise is also known as clutter and can be easily recognized as it forms continuous horizontal reflections across the radargrams (Figure 2.15) (Goodman & Piro, 2013). The background removal filter is applied to remove this type of noise. This filter measures the average pulse of the entire amount of traces, which is then subtracted from each trace individually. This filter's implementation is not ideal in the case where the target is parallel to the ground, as it may recognize those reflections as noise and cut them out (Goodman & Piro, 2013). The background removal filter has the same end result regardless of the order it is applied in.

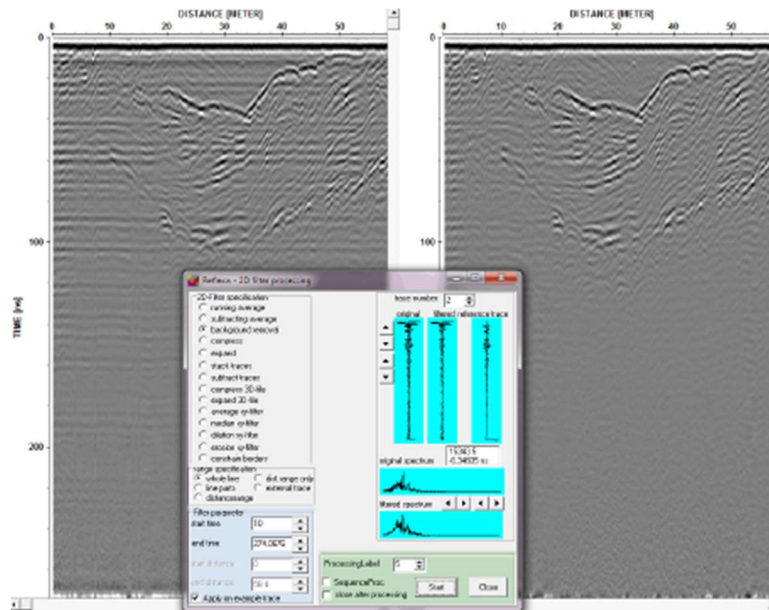


**Figure 2.15:** Radargram before applying the background removal filter (left) and after applying it (right) (Source: Sandmeier)

### 2.4.3. Bandpass frequency

Bandpass frequency is a filter used to exclude frequencies that are not a part of the bandwidth of the GPR antenna by using the Fourier transform. Therefore, it uses high-pass and low-pass filters to refine the radargram of noise from the undesired frequencies (Figure 2.16). In order to apply this filter the operator must choose manually the high-pass band, the peak frequency and the low-pass band on a characteristic trace (Figure 2.17). The filter is then applied with the chosen parameters to each trace individually. The high-pass band removes the lower frequencies from the spectrum, which may contain noise from the ground-wave and other human sources (Bendetto et al., 2017). The low-pass band removes the undesired high frequencies from the spectrum, which are commonly caused by external electromagnetic interference.

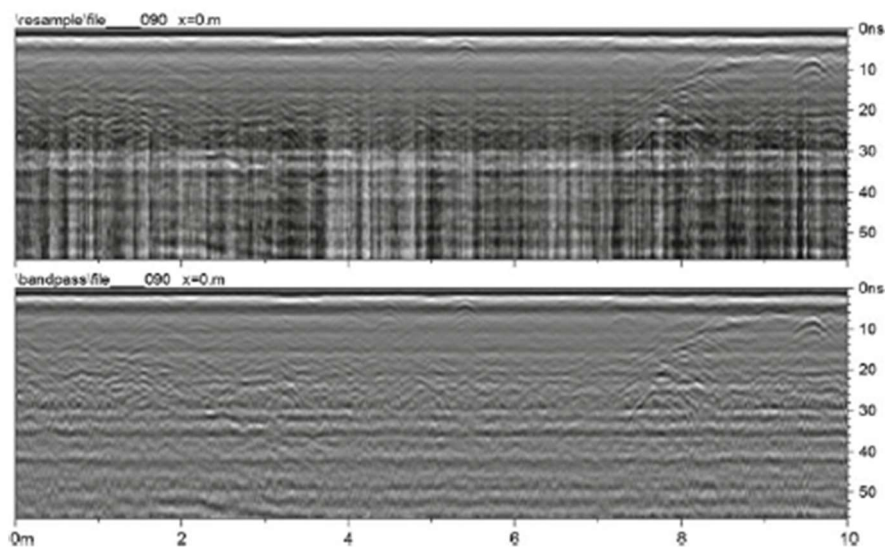


**Figure 2.16:** Reflection profile before the application of bandpass frequency filter (up) and after its implementation (down) (Source: Goodman & Piro, 2013)

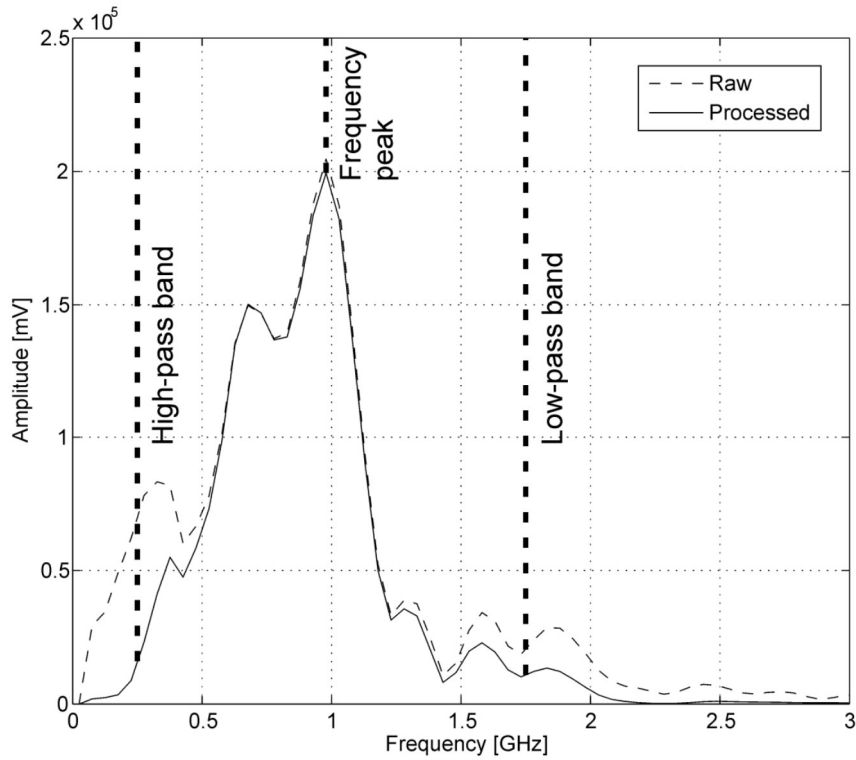


**Figure 2.17:** Selection of the bandpass frequency filtering parameters (range of desired frequencies). The dashed line represents the raw trace and the continuous line represents the filtered trace (Source: Bendetto et al., 2017)

#### 2.4.4. Time zero correction

Time zero correction is a filter necessary for depth accuracy. It aims to adjust the radargram to the actual time when the first signal response of the subsurface is observed. Usually, a delay in signal penetration is always present, due to internal transmission and a possible gap between the antenna and the ground. If the time zero correction is not applied the depth of the targets will be overestimated. The correct time zero is generally thought to start after the monochrome line above the direct signal, but for the sake of accuracy it is better to inspect each trace to detect the exact time of the first response (Figure 2.18) (Utsi, 2017).

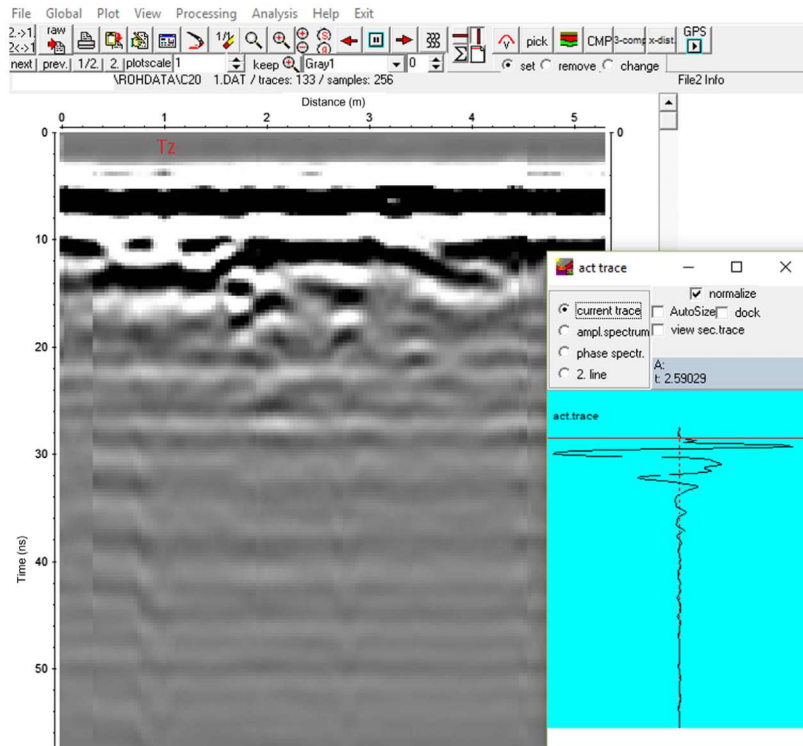


**Figure 2. 18:** Example of time zero correction selection done on an individual trace (Source: Utsi, 2017)

#### 2.4.5. Spectral whitening

Another common filter that functions as an alternative for bandpass filtering is the spectral whitening filter. This filter essentially transforms the recorded signal into the spectral domain using the Fourier transform. After this transformation the real and imaginary spectral amplitudes are normalized and the magnitudes of all the spectral frequencies are set to 1 (Goodman & Piro, 2013). The effect of spectral whitening is to create a more distinct image of the reflections by balancing singles and creating more equally distributed gained pulses (Figure 2.19). This result is achieved primarily by the changes in the phase of the signal and not because of changes in the gain between frequencies (Goodman & Piro, 2013).

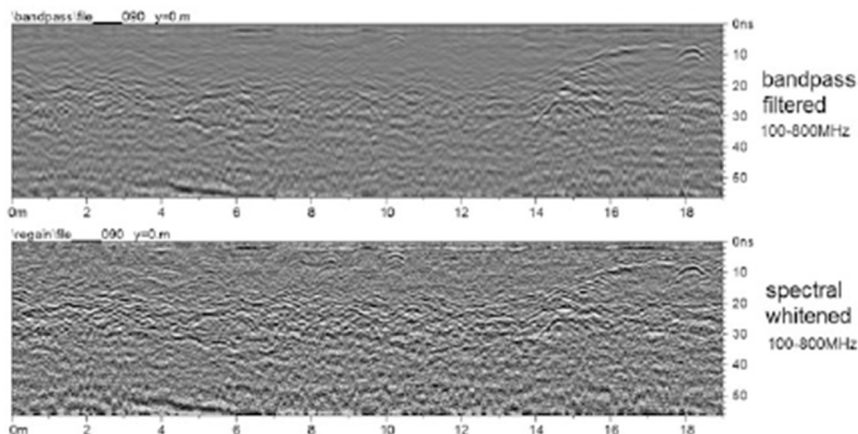


**Figure 2. 19:** Comparison of the effect on a radargram of a bandpass filter (up) as opposed to the effect of a spectral whitening filter (down) (Source: Goodman & Piro, 2013)

#### 2.4.6. Deconvolution

The deconvolution filter aims to improve resolution by maximizing bandwidth and reducing pulse dispersion (Annan, 2009). It can be characterized as an inverse temporal filter that compresses the recorded signals (Dojack, 2012). It is most frequently used in cases where multiple reflections (consistent horizontal bands) are observed in the radargram. It is also a convenient tool for reducing the influence the transmitted pulse has on the data (Goodman & Piro, 2013). The ultimate goal of filtering a reflection profile is to get a clear image that represents the structure of the subsurface and the targets that are being investigated, therefore if an impulse response of the antenna is observed on a shallow reflector, the ringing effect of the reflection might conceal any deeper targets. By using the deconvolution filter it is possible to decrease the intensity of this reflection and eliminate the ringing in order to examine any deeper reflections (Figure 2.20) (Goodman & Piro, 2013).

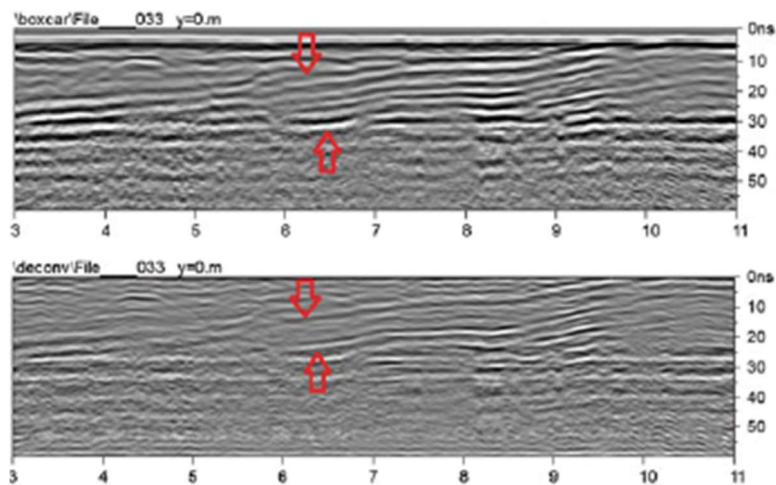


**Figure 2. 20:** The effects of the deconvolution filter before (up) and after (down) it has been applied to the radargram. The red arrows indicate the existence of an interface structure that was not visible before the implementation of the filter (Source: Goodman & Piro, 2013)

#### 2.4.7. Migration

Migration is a filter used to mathematically collapse hyperbolas into single points (Utsi, 2017). Hyperbolic reflections are formed due to the broad band transmission of the antenna, which sends signals in a different range of frequencies. As a result, when the GPR system is moving across a line, greater two-way travel times are recorded as the antenna moves away from the target, thus the hyperbolic shape of the reflection (Figure 2.21). In these cases, the migration filter is necessary to accurately locate the position of the target. The implementation of this filter is particularly useful in the events where the primary targets have a linear shape, but it is not always necessary, as it may also cause undesired results (Utsi, 2017). In addition, in order to use migration it is essential to know the velocity of signal propagation in the specific material (Annan, 2009). The effect the input of the wrong velocity has on the filter is shown in Figure 2.22.

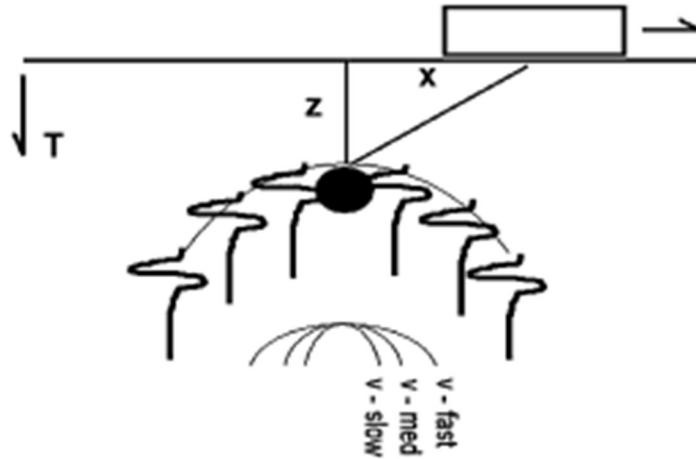


Figure 2. 21: Visualization of how hyperbola reflections derive (Source: Goodman & Piro, 2013)

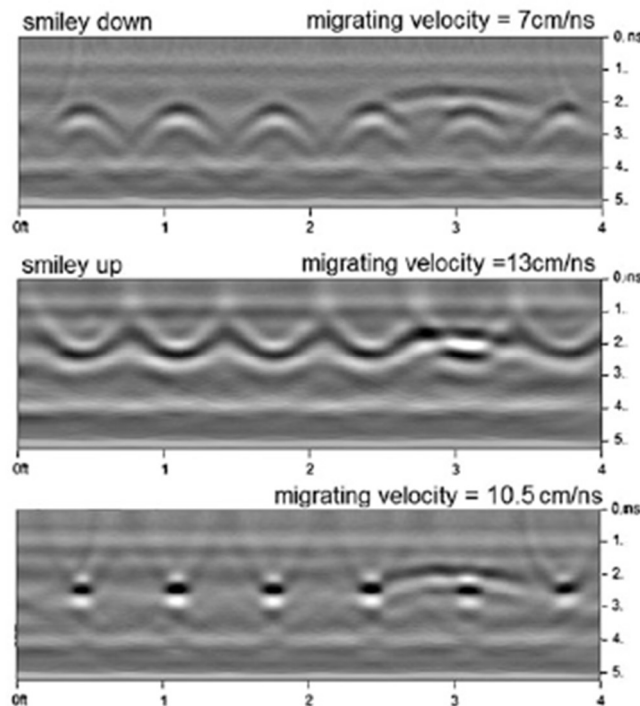
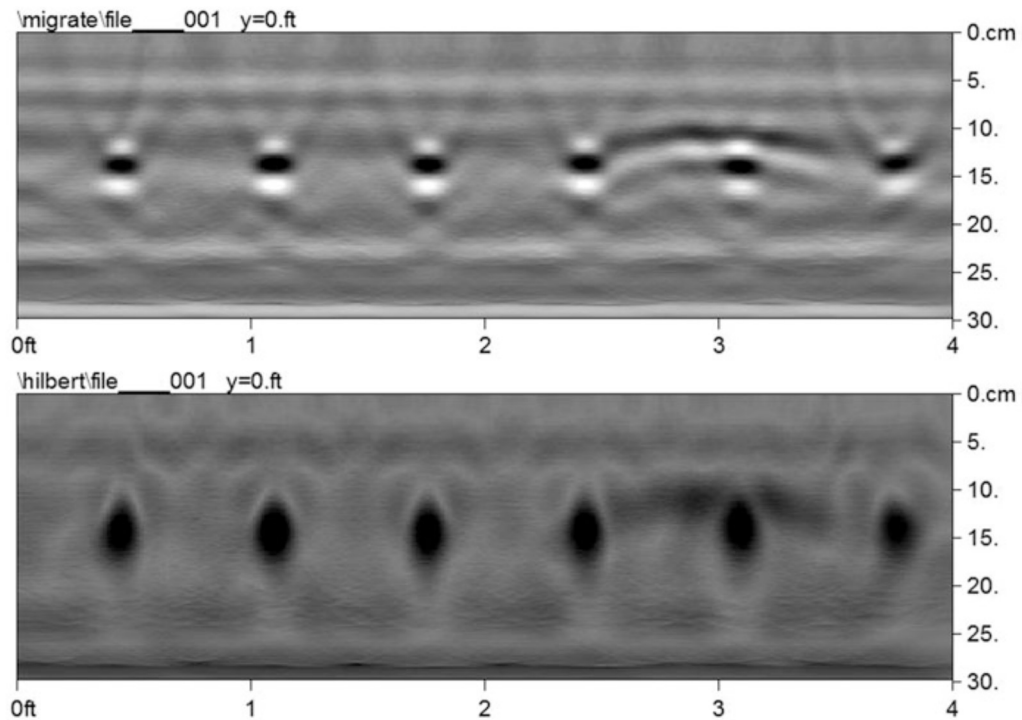


Figure 2. 22: Examples of migration when the input velocity is too low (first diagram), too high (second diagram) and accurate (third diagram) (Source: Goodman & Piro, 2013)

#### 2.4.8. Hilbert transform (Envelope)

Another useful processing filter is the one that displays the envelope of radar signals. The envelope can be characterized as the absolute value of the pulse, as a result this enhances the image of the reflection profile by displaying the results plainly as strong or weak reflections. The application of the envelope on recorded data is achieved using the Hilbert transform. In mathematical terms, this means that first of all the Fourier transform of the radar pulse is performed, which as a result shifts the negative frequencies by 90°, and then an inverse Fourier transform is made (Goodman & Piro, 2013). This action creates a signal that is

completely in the positive domain, hence representing the envelope of the recorded data. The end result is a clearer image that demonstrates the structure of the subsurface in the form of single positive reflections (Figure 2.23) (Goodman & Piro, 2013).



**Figure 2. 23:** Example of a Hilbert transform (envelope) on radargram with previously applied migration (Source: Goodman & Piro, 2013)

## 2.5. Data representation

A brief reference on how GPR data can be displayed was made in the introduction (Figure 2.2). More specifically, GPR data can be represented in the following forms:

- 1) **A-scan (Amplitude-scan)** – it represents a 1D depiction of a single trace response and is characterized by the waveform of the radar pulse (Figure 2.24).
- 2) **B-scan (Brightness-scan)** – it consists of a 2D depiction composed of a sequence of traces (A-scans) along a line. It is also known as a radargram or reflection profile that visualizes the amplitude of a response analogous to a certain depth. As previously mentioned, it is the format on which processing is done (Figure 2.24).
- 3) **C-scan (Contrast-scan)** – it is a 3D image representation that emerges from gridding subsequent B-scans and then processing them in a manner that displays reflection amplitudes for a specific depth range. They are also known as amplitude slice-maps and volume-depth slices (Figure 2.24). It is generally accepted that any type of interpretation is mainly done on C-scans.

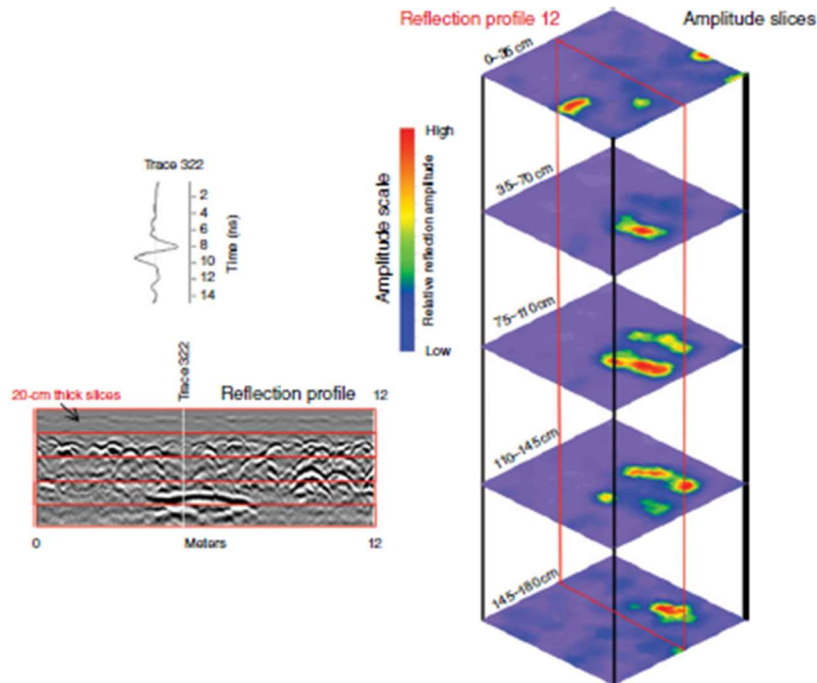


**Figure 2. 24:** Image depicting the different forms of GPR data representation. In the upper right corner is an A-scan (trace), below it is a B-scan (reflection profile) and on the left a C-scan (amplitude slices) (Source: Conyers, 2016)

### 3. Data Acquisition

Designing a GPR survey of an archaeological site takes time and needs to take in consideration all the factors mentioned in the theory and then apply them to the specific case. Examples should be taken from different GPR surveys for geoarchaeology, especially if they were done in similar environments. In order to achieve data acquisition of high quality the most important steps to undertake are the correct choice of equipment, a thorough design of the grid in the study area and the appropriate data acquisition parameters.

#### 3.1. Equipment

The equipment that was used in this study includes a monostatic system with a shielded antenna with center frequency of 250MHz provided by MALÅ Geoscience. The system was positioned on top of a cart in order to facilitate movement. A computer console was also connected to the system with the purpose of storing the collected data.

#### 3.2. Methodology

The study area consists of a region with dimensions 20m×15m and is situated in close proximity to an existing archaeological excavation that contains wall remains (Figure 3.1). The archaeological findings of said excavation provided useful information on the dimensions and orientation of the targets for this study. Before the actual data acquisition process a grid was designed (Figure 3.1.). For optimal ground coverage a transect spacing of 0.5m was chosen. The main factor that influenced the transect orientation is the orientation of the remains found in the excavation. It is considered that the most precise estimation of GPR target locations is done when the transect orientation is perpendicular to the target, therefore a SE and NE direction was selected.

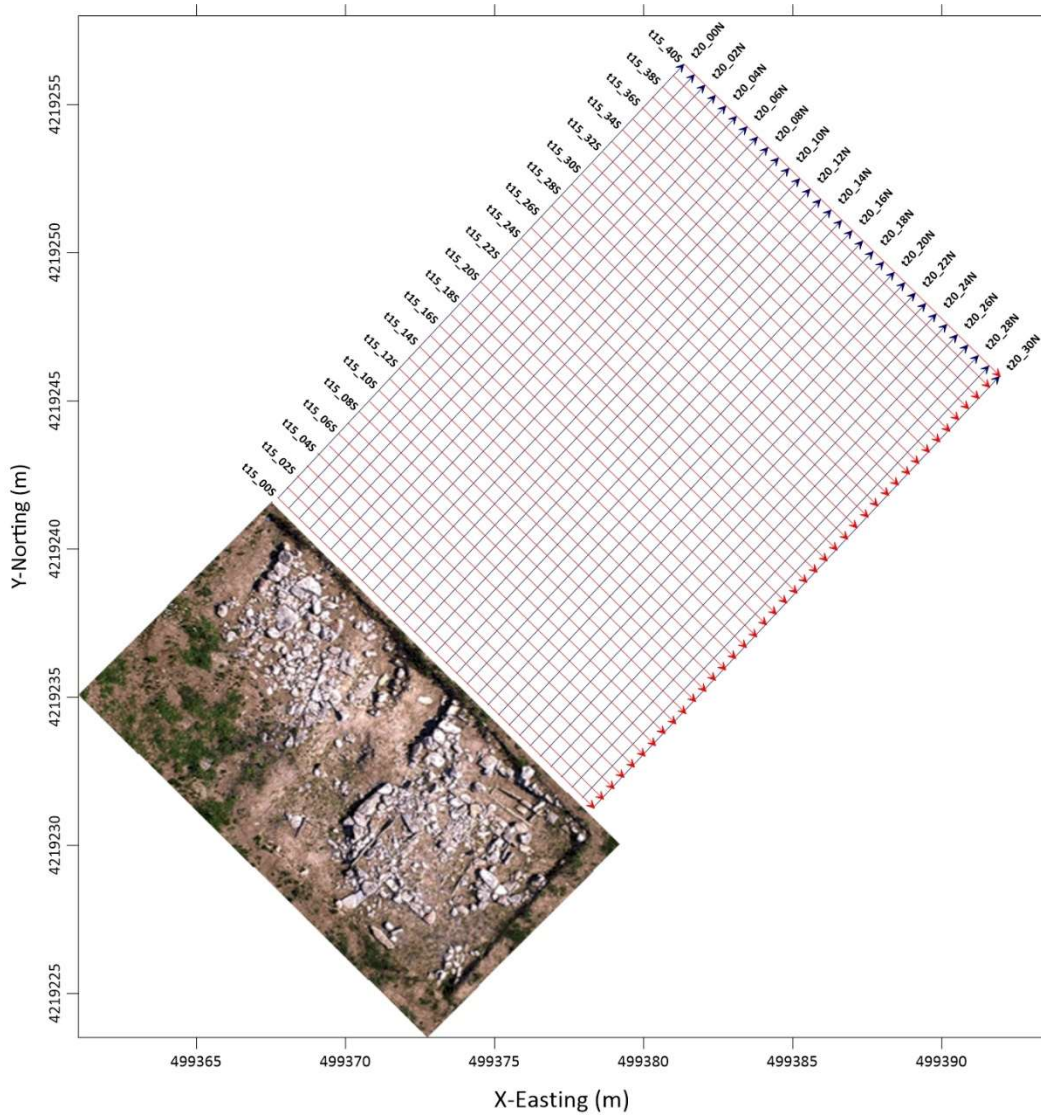


**Figure 3.1:** Map that shows the excavation next to the study area and the grid of GPR lines that was chosen for this study. A total of 72 GPR lines were recorded, 41 in SE direction (red lines) and 31 in NE direction (blue lines)

The next step in the process of planning the study was to create the actual transect lines at the study area by accurately measuring the distance and lining the grid lines using a rope (Figure 3.2). Since the equipment that was used did not possess a built-in GPS system, in order to georeference the data later in the process, the coordinates of the start and end point of each transect line were measured using a separate GPS system (Figure 3.3).



*Figure 3.2: Images from the data acquisition process*



**Figure 3.3:** Measuring GPS coordinates of the start and end point of the GPR lines

After completing the grid design and measuring the GPS coordinates, the GPR survey could begin. A total of 72 GPR lines were carried out, 41 of those had a length of 15m and were recorded in a SE direction and the remaining 31 had a length of 20m and were recorded in a NE direction (Figure 3.1).

### 3.3. Measurement parameters

The measurement parameters assigned to the GPR system can be seen in Table 5. They were determined taking into account the theory previously mentioned.

**Table 5:** Description of the parameters used for GPR data acquisition

| Parameter         | Value   |
|-------------------|---------|
| Center frequency  | 250 MHz |
| Time window       | 196ns   |
| Samples per trace | 512     |
| Step size         | 0.02    |
| Stacking          | 16      |
| Transect spacing  | 0.50m   |

## 4. Data Processing

The processing of data is an inevitable step in order to enhance the signal and achieve the main goal of this survey, locating the archaeological remains. For the specific study, this procedure will be broken down into three main categories that will contain the three main chosen types for GPR data representation. These categories are 2D radargram section processing and processing required for the creation of volume-depth slices.

### 4.1. 2D radargram sections

The processing of the reflection profiles was completed using ReflexW Version 7.5.8 provided by Sandmeier geophysical software. Based on the experience of previous studies and some personal experimenting with the filters the most appropriate processing flow was selected. The processing steps consist of the filters dewow, start time (time zero) correction, background removal, bandpass frequency, spectral whitening, deconvolution, f-k migration (Stolt) and envelope. For interpretation purposes the same filters were applied on all the radargrams

#### 4.1.1. Subtract-mean (dewow)

As previously mentioned, the dewow filter is used to remove very low-frequency energy from the reflection profile that does not provide any type of information. In this case low-frequency energy was observed in the upper part, but mainly in the lower part of the signal, due to attenuation. The filter requires the input of a time window parameter, which was set to 4ns. The results after applying the filter can be seen in Figure 4.1.

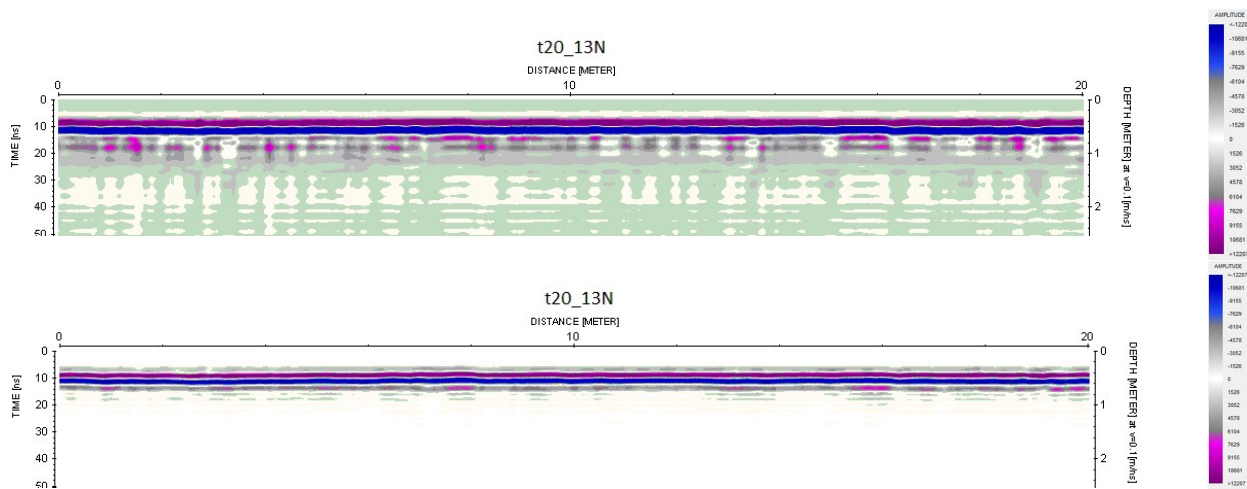


Figure 4. 1: Example of a raw reflection profile (up) and the result of applying dewow (down)

#### 4.1.2. Background removal

This filter aims to remove any additional noise, most commonly clutter. Although, initially the effect of clutter was not observed completely through the whole range of data, after applying the filter a signal enhancement was noticed, so it was concluded to add this filter to the processing steps. The input of parameters is not necessary, it was applied to the full extent of the profile, but if desired it can be applied to a specific time/depth. The results of this step are shown in Figure 4.2.

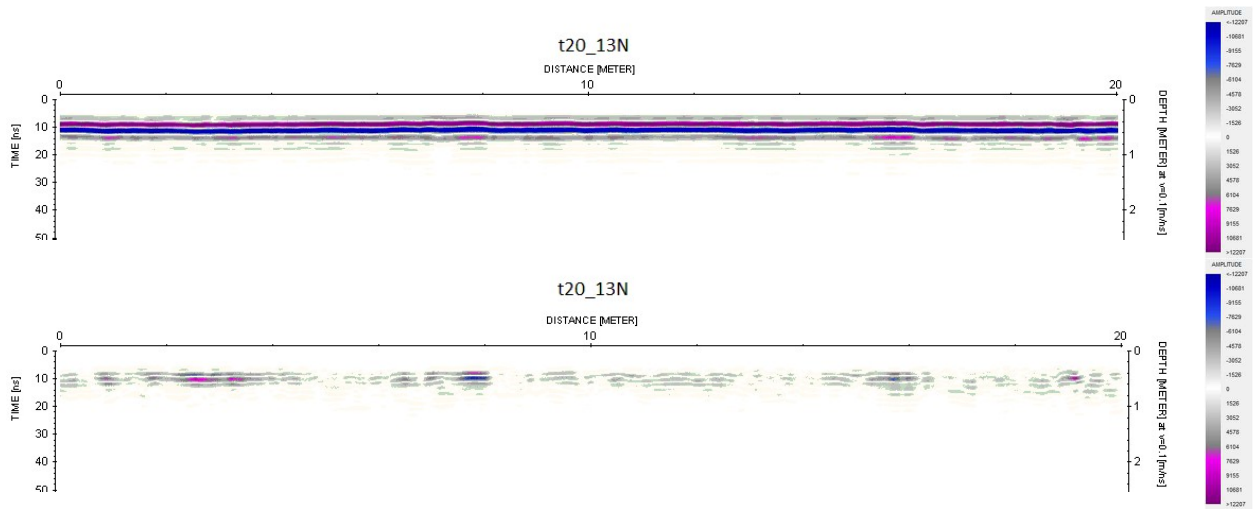


Figure 4. 2: The results of applying background removal (down) after the dewow filter (up)

#### 4.1.3. Bandpass frequency

Bandpass frequency was applied in order to remove any noise that was outside the bandwidth range of the antenna, in other words noise from external sources. This filter requires that the parameters are chosen by the operator. After thorough examination of the traces the chosen frequencies were a lower cutoff of 23MHz, a lower plateau of 161 MHz, an upper plateau of 238 MHz and an upper cutoff of 583 MHz. The result can be seen in Figure 4.3.

#### 4.1.4. Start time correction

After examining the most part of the traces to confirm that the time delay was equal in all of them, the start time correction was chosen to be -4ns (Figure 4.3), which corresponds to the first signal response observed in each trace.

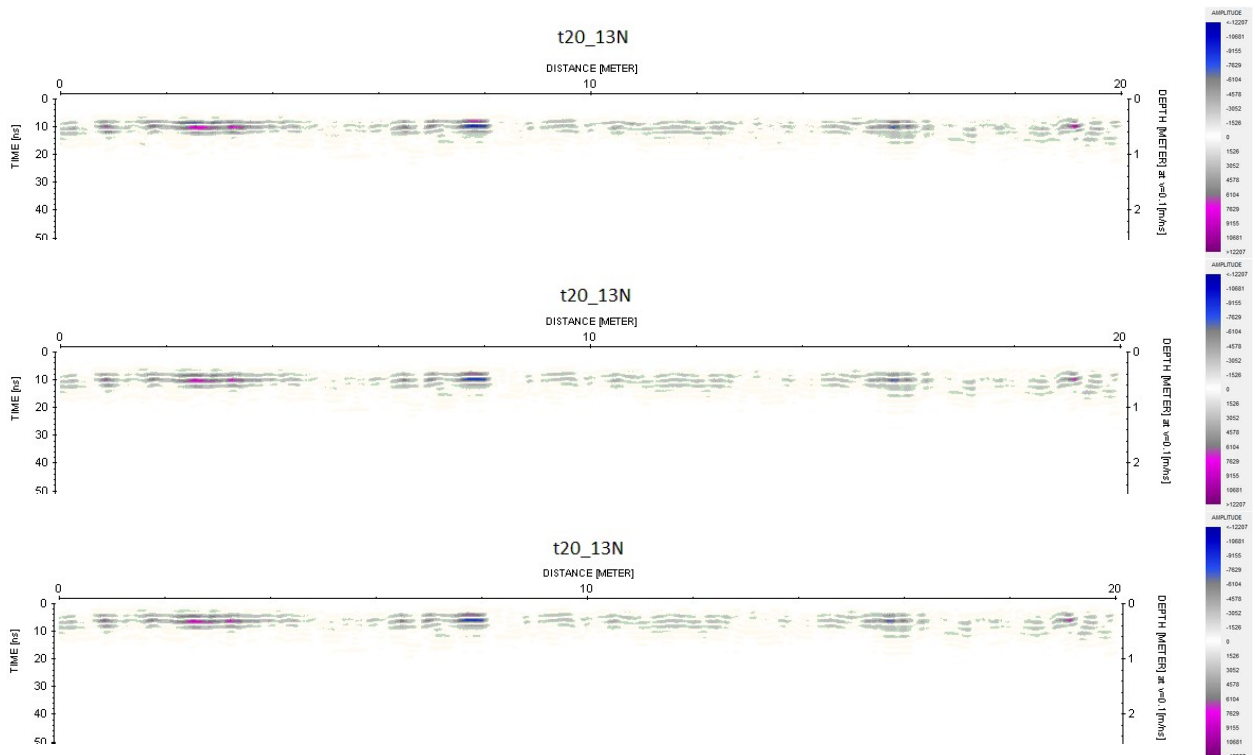


Figure 4. 3: The top reflection profile corresponds to the background removal filter, whilst the middle is the result of bandpass frequency application and the bottom has start time correction.

#### 4.1.5. Spectral whitening

Spectral whitening was applied to create more equally distributed gained pulses. The input parameters chosen were a start frequency of 606 MHz and an end frequency of 1297 MHz. At first the results of applying this filter were not thought to be ideal (Figure 4.4). An experiment was done, which excluded this filter, but by following through the next steps of processing (deconvolution, migration and envelope) it was observed that the end results were better by including it.

#### 4.1.6. Deconvolution

The next step of processing included the deconvolution filter to improve the resolution and enhance the signal. The input parameters involved autocorrect end of 0.1 and a filter length of 4. This showed great improvement in the amplitude intensity of the reflecting areas (Figure 4.4).

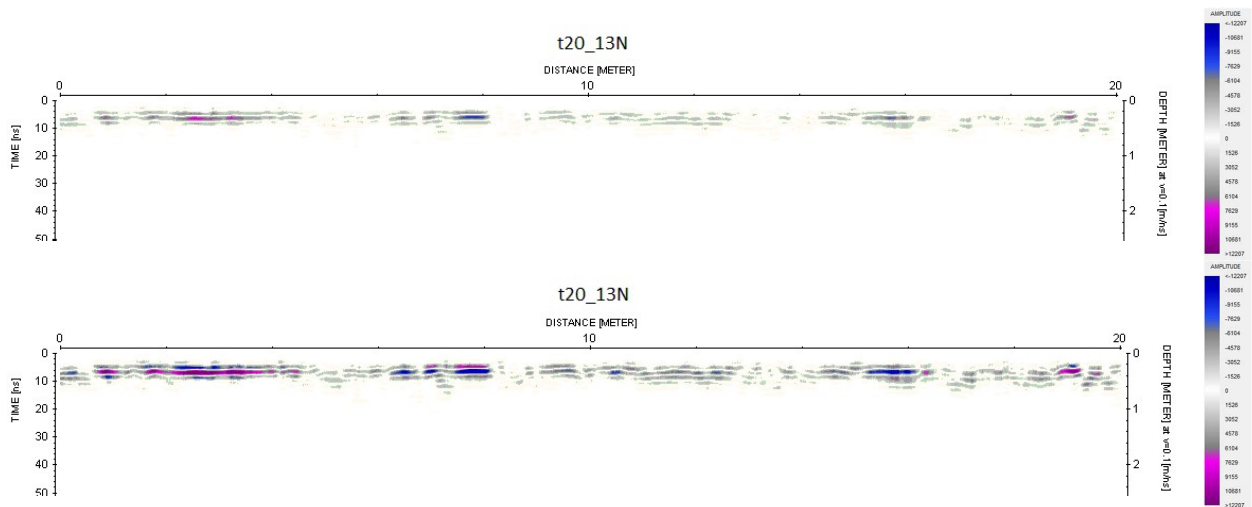


**Figure 4. 4:** The effect of spectral whitening on the radargram (up) followed by the result of deconvolution applied to it (down)

#### 4.1.7. F-k migration (Stolt)

One of the final processing steps included migration in order to distribute more evenly and accurately the position of the reflectors. In order to do so the fundamental parameter was wave propagation velocity in the medium. The environment in which the targets are buried consists mainly of clay and sand, which respectively have propagation velocities of 0.6 m/ns to 0.12 m/ns (Table 1). The filter was tested using the velocities in this range and it was concluded that the most appropriate value is 0.9 m/ns. The results of the migration filter are shown in Figure 4.5.

#### 4.1.8. Envelope

Lastly, the Hilbert transform filter or envelope was applied in order to convert the signal in the positive domain. This step provides improved visualization of highly reflective areas, which most probably represent the targets.

The total amount of processed reflection profiles can be found in the appendix.

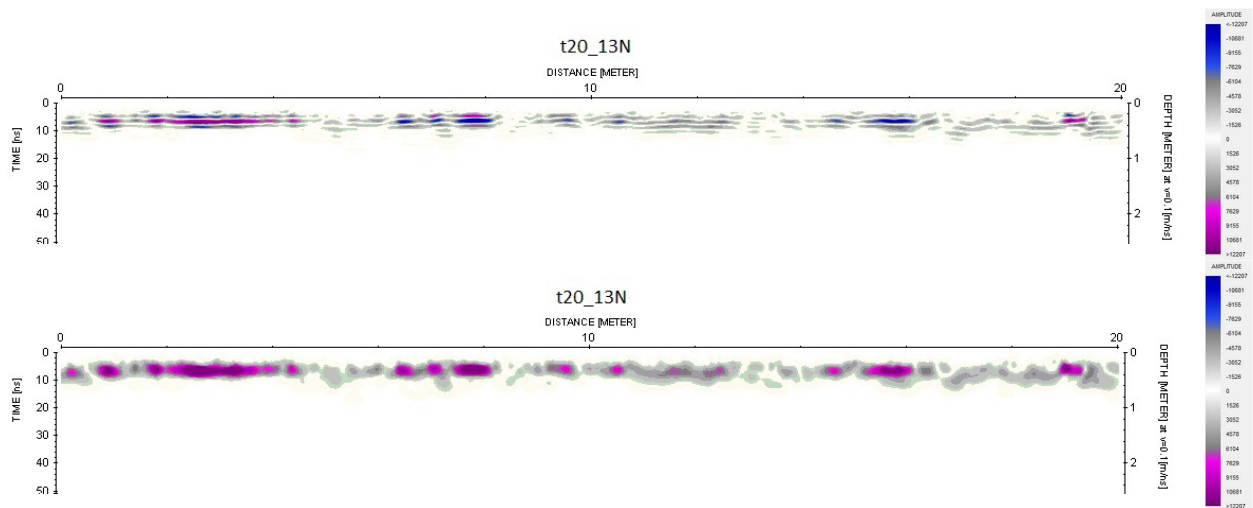


Figure 4. 5: Application of the migration filter on the data (up) and finally the envelope filter (down)

## 4.2. Volume-depth slices

In order to create volume-depth slices, also known as amplitude slices, the data from all the processed radargrams had to be compiled in one place so it could be analyzed, resampled and gridded in a specific way to construct the 3D image. As one can imagine, such big amounts of data are not easily processed with simple programs. As a result, the program that was used because of its capacity is MATLAB.

The first step of compiling the data from the processed reflection profiles, was to convert the visual data into quantities which could be tampered. This meant exporting the recorded and processed data of the B-scan in the form of a table with X (distance), Y (depth) and Z (envelope amplitude) parameters for each point of the radargram. This can be achieved by exporting the ASCII file using ReflexW. The next step includes georeferencing the data. As it was previously mentioned, the equipment that was used did not have a built-in GPS system. Therefore to georeference the data with as much accuracy as possible, the coordinates measured at the beginning and end of each GPR section were used to assign coordinates to each data point. This operation was accomplished by using MATLAB. The following processing step involved asserting the depth range that was of importance to this study. This action is performed in order to set the dimensions of each amplitude slice and to exclude any unnecessary data, so that the total volume of the data can be decreased. The best way to achieve this is by creating a diagram that depicts the distribution of the signal's amplitude according to its depth (Figure 4.6). Assuming that the highest amplitudes represent the targets of this study, it can be seen from the diagram that their distribution is located in depths 0.10m-0.60m. As a result, the creation of six volume-depth slices was selected, each of which represented an amplitude map of 10cm in the mentioned range. More specifically, the data volumes from depths 10-20cm, 20-30cm, 30-40cm, 40-50cm and 50-60cm were extracted as separate sets of data that included their X, Y and Z parameters by using an algorithm in MATLAB. These data sets were then imported as grids in Surfer to create the corresponding amplitude slice maps (Figure 4.7). It must be noted that the amplitude of the data was normalized during processing to equalize the scale for all data and to highlight targets of amplitudes higher than 10,000.

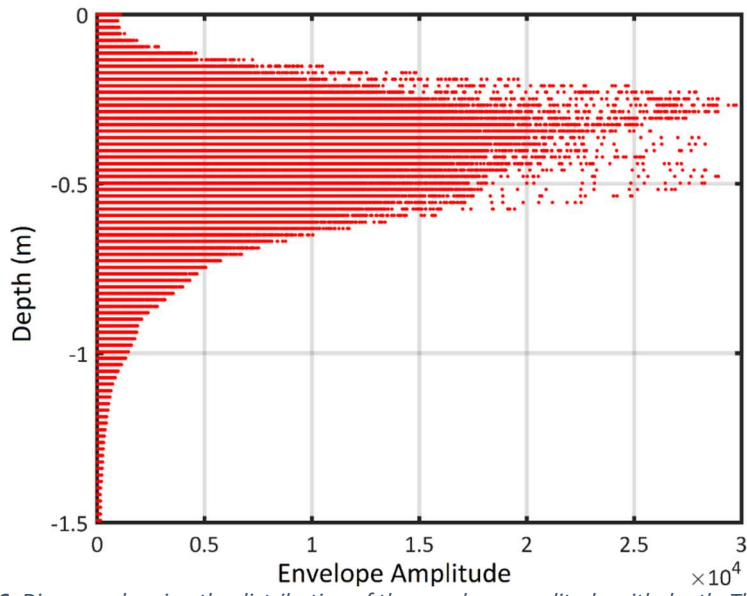


Figure 4. 6: Diagram showing the distribution of the envelope amplitude with depth. The data from the total amount of processed radargrams was used.

20-30cm GPR Volume-depth Slice  
(NE & SE data)

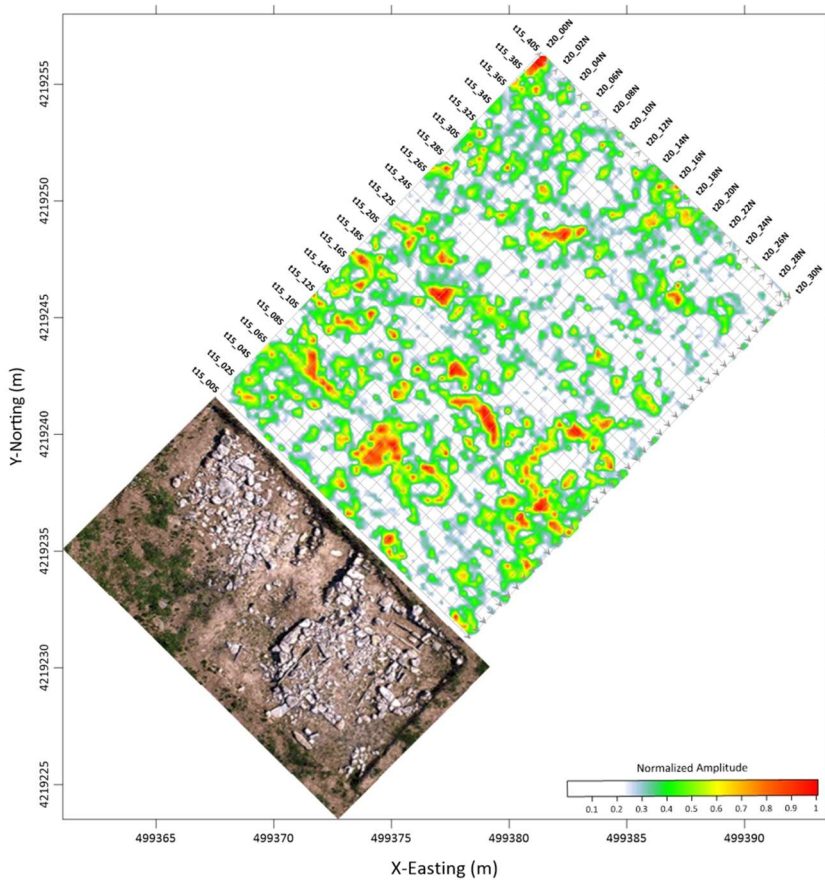


Figure 4. 7: 20-30cm Volume-depth slice

## 5. Results and Conclusions

For the presentation of the results, in order to interpret them, two ways of visualization were chosen, which include fence diagrams and volume-depth slices.

Three fence diagrams were created with the purpose of asserting and comparing the data recorded in different directions. Therefore, Figure 5.1 represents the fence diagram of the reflection profiles recorded in a NE direction, Figure 5.2 displays the fence diagram of the sections acquired in a SE direction and finally, Figure 5.3 depicts the fence diagram of the reflection profiles in both directions. It is important to mention that in this case, this type of presentation does not provide valuable information regarding the depth of the targets, it is used only to assess the position of the strongest reflections. Additionally, the position of the fence diagrams does not coincide with the true direction, in accordance to North, but are fitted in a position that shows best the results.

As previously mentioned, the amplitude of the data has been tampered in a way that highlights strong reflections of an amplitude higher than 10,000. This is visually represented by the warm colors, whilst the colder colors indicate lower amplitude values. Taking this into account, two major areas of strong reflections can be observed in all of the fence diagrams. For the sake of description, the area outlined with a blue dashed line will be called area 1 and the area outlined with the red dashed line will be called area 2.

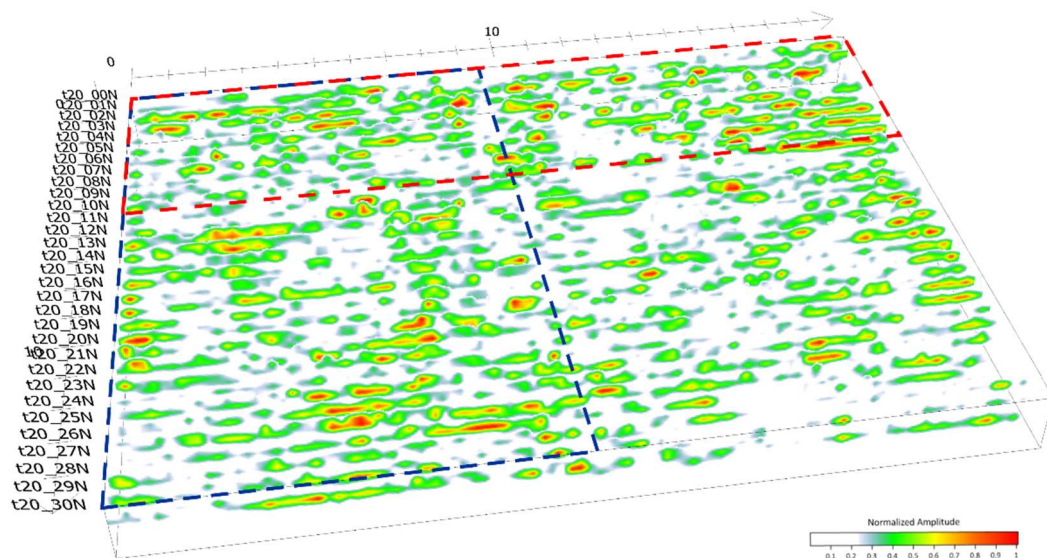


**Figure 5. 1:** Fence diagram of the reflection profiles recorded in the NE direction. The dashed lines indicate areas of interest, due to the observed strong reflections. The existing excavation where the archaeological remains were found is situated on the left hand side.

In Figure 5.1 high amplitudes, characterized by orange and red colors, are observed in both area 1 and area 2. One can see that for the most part they extend along the direction of the section which indicates a linear target was recorded that has the same NE direction. On the other hand, the high amplitudes recorded in the form of points might indicate either individual targets or that the response was recorded perpendicularly to a buried structure.

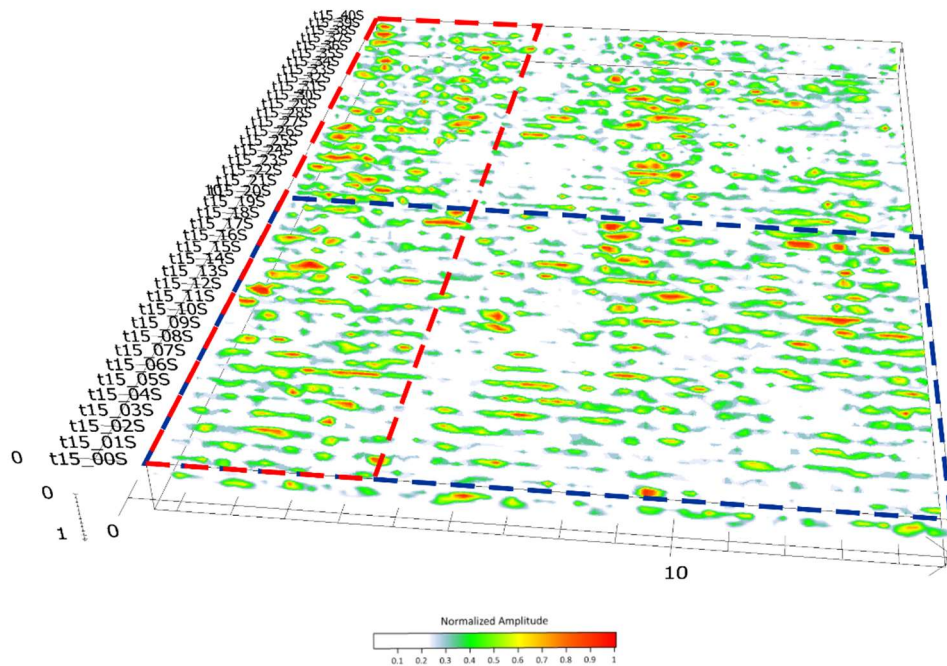


**Figure 5. 2:** Fence diagram of the reflection profiles recorded in the SE direction. The dashed lines indicate areas of interest, due to the observed strong reflections. The existing excavation where the archaeological remains were found is situated at the bottom of the image.

The fence diagram of the SE direction sections (Figure 5.2) is mainly characterized by spot focused reflections, meaning that the probable targets are for the most part perpendicular to the GPR line's direction. This is also confirmed by the interpretation of Figure 5.1. Less powerful linear reflections are observed and mostly at the lower part of both area 1 and area 2.

To complete the observations, it is best to use the gridded data of both directions (Figure 5.3). It shows that the locations of high amplitude reflections coincide, which is a good sign that acquisition and processing were done properly. In addition, it gives a bigger picture on the structure of the targets. A big linear formation is observed extending along area 2 in a NE direction. In area 1 various straight-shaped formations are observed both in NE and SE directions.

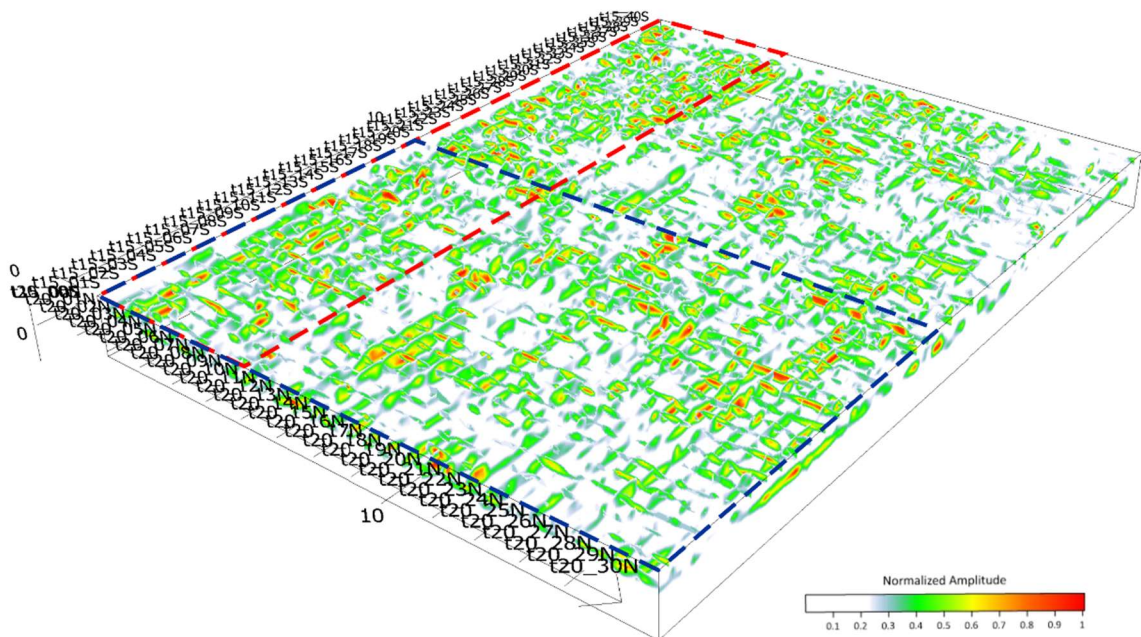


*Figure 5.3: Fence diagram of the radargrams recorded in both NE and SE directions. The location of the archaeological excavation is in the bottom left corner.*

Six volume-depth slices were produced, each of which displays a volume of data for 10cm of depth (Figures 5.4-5.8). The first amplitude map from 10-20cm (Figure 5.4) does not provide much insight, since not much data of significant amplitude is present. Areas of interest start to appear at 20-30cm of depth (Figure 5.5). More specifically, the same area (area 1) that was observed in the fence diagrams emerges. The amplitude map gives the opportunity of a more detailed interpretation, due to better resolution and distribution of data. On that note, high amplitude values are observed mainly in the center and eastern part of area 1. In the center a dense structure with somewhat linear boundaries can be found close to the excavation and NE of it a half-moon shaped figure is present. In the eastern corner an almost perfect rectangular formation can be seen. Exploring deeper (Figure 5.6) into the volume-depth slice from 30-40cm, the structures mentioned continue to appear and with an increased amplitude. Additionally, at this depth anomalies in area 2 start to emerge, with a characteristic linear shape extended in a SW-NE direction. The concentration of anomalies from both area 1 and area 2 continue to exist in depths 40-50cm (Figure 5.7), although a fade in the intensity of the reflection is noticeable. Finally, in depths between 50cm and 60cm (Figure 5.8) a very small amount of reflections in area 2 persevere.

### 10-20cm GPR Volume-depth Slice (NE & SE data)

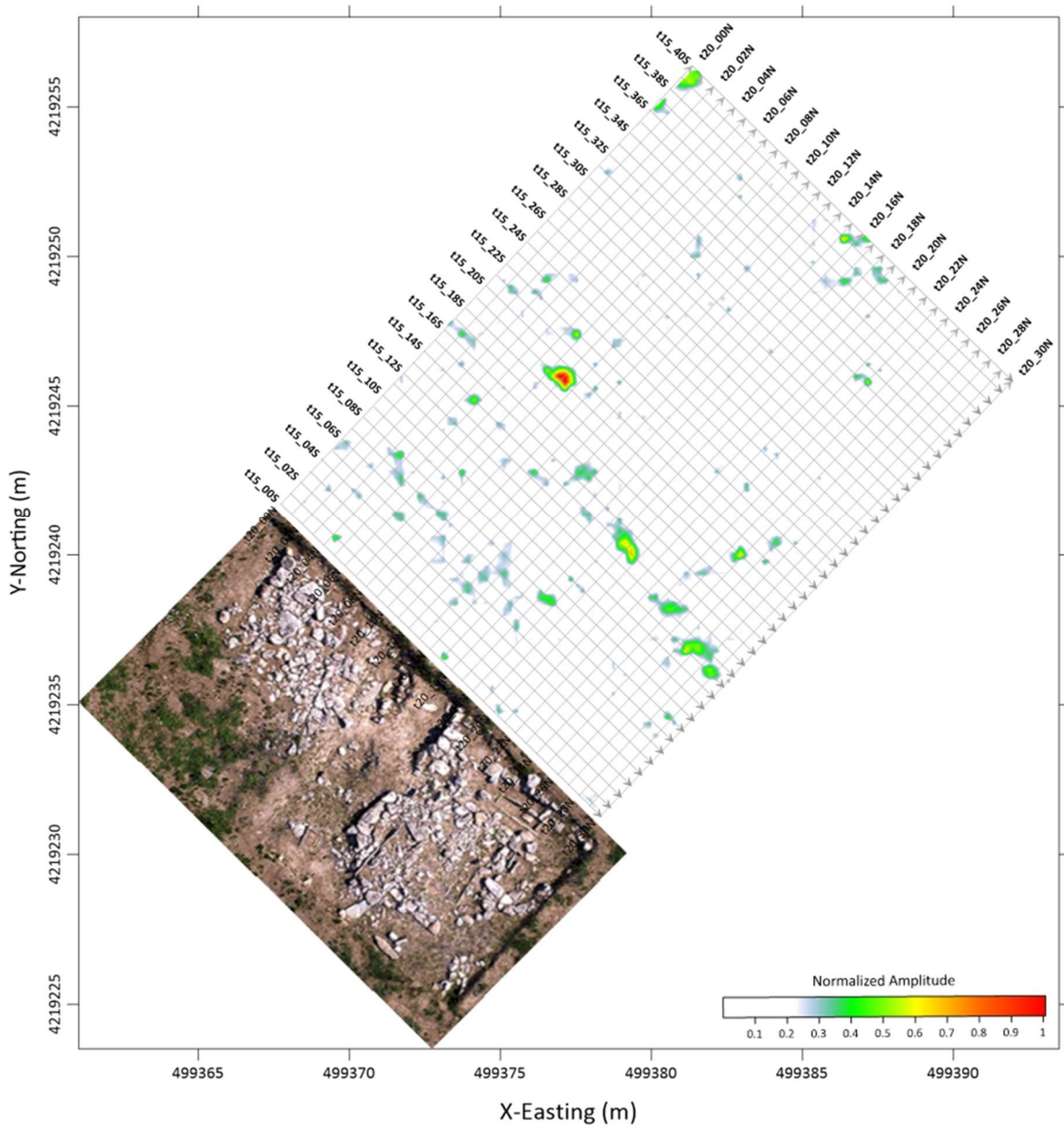


*Figure 5. 4: 10-20cm Volume-depth slice*

### 20-30cm GPR Volume-depth Slice (NE & SE data)

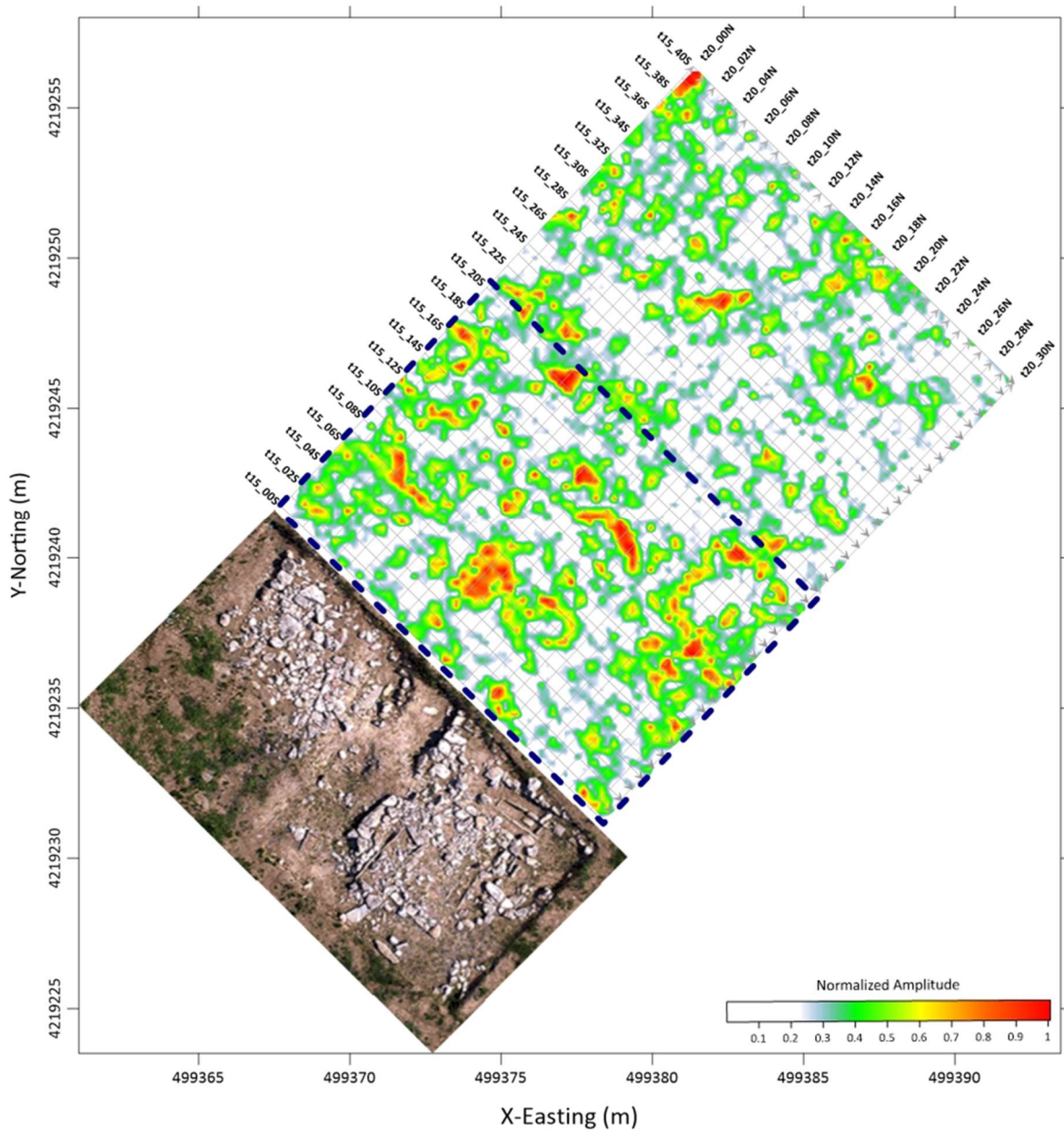


*Figure 5. 5: 20-30cm Volume-depth slice. The area outlined in a blue dashed line represents an area of interest (area 1), also depicted in the fence diagrams.*

### 30-40cm GPR Volume-depth Slice (NE & SE data)

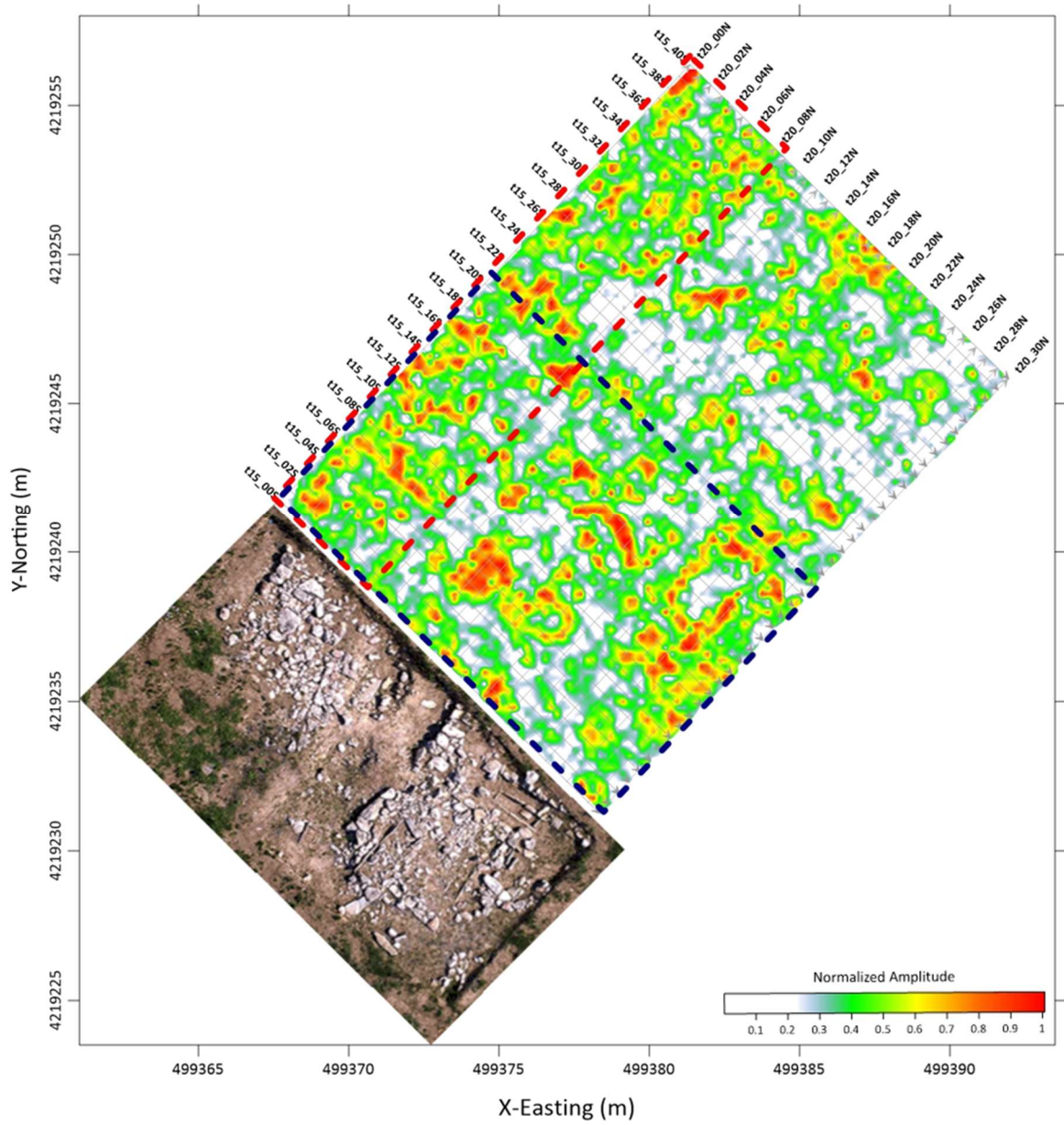


*Figure 5. 6: 30-40cm Volume-depth slice. The areas outlined in a blue dashed line (area 1) and a red dashed line (area 2) represent areas of interest, also depicted in the fence diagrams.*

### 40-50cm GPR Volume-depth Slice (NE & SE data)

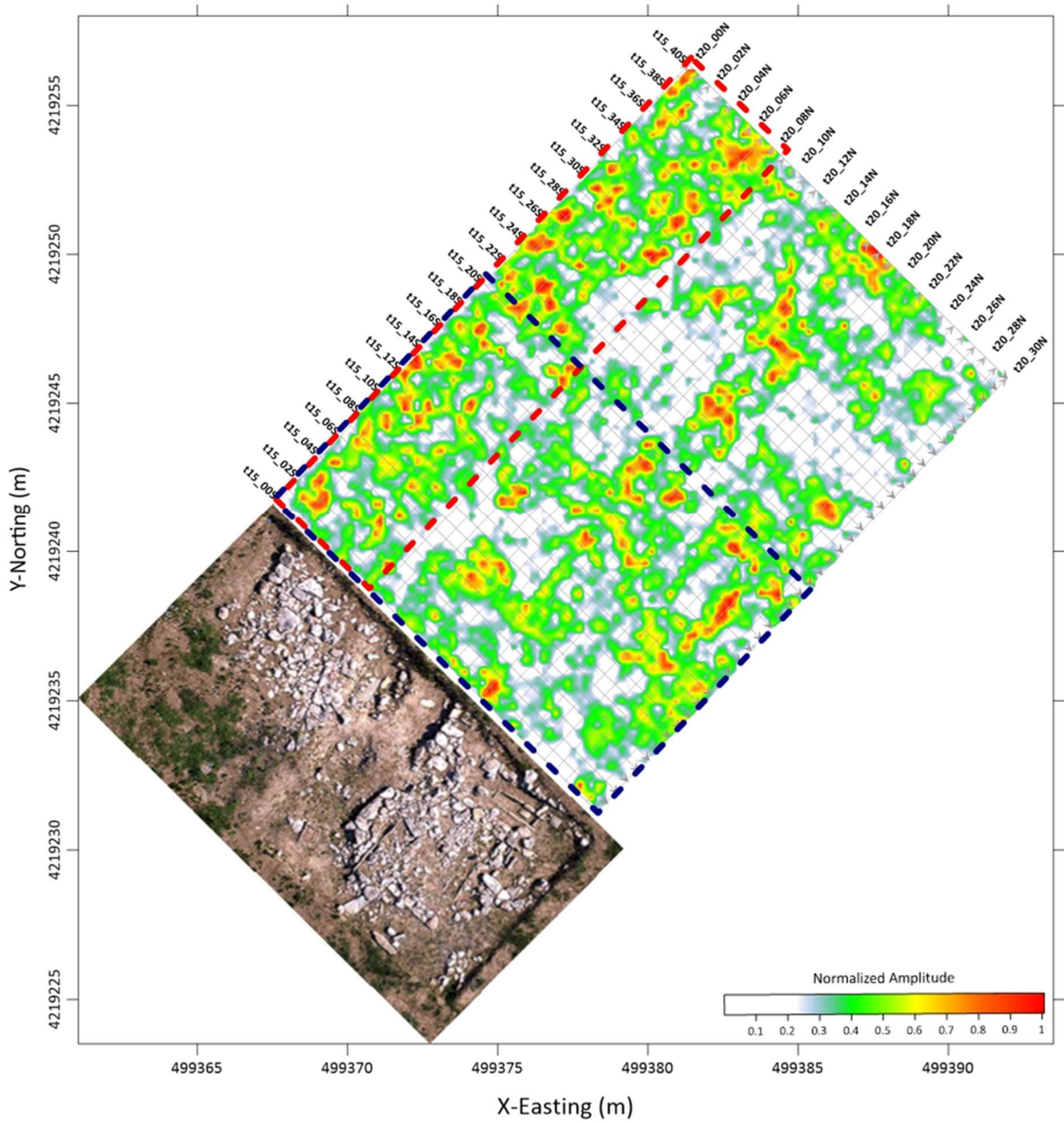


*Figure 5. 7: 40-50cm Volume-depth slice. The areas outlined in a blue dashed line (area 1) and a red dashed line (area 2) represent areas of interest, also depicted in the fence diagrams.*

### 50-60cm GPR Volume-depth Slice (NE & SE data)

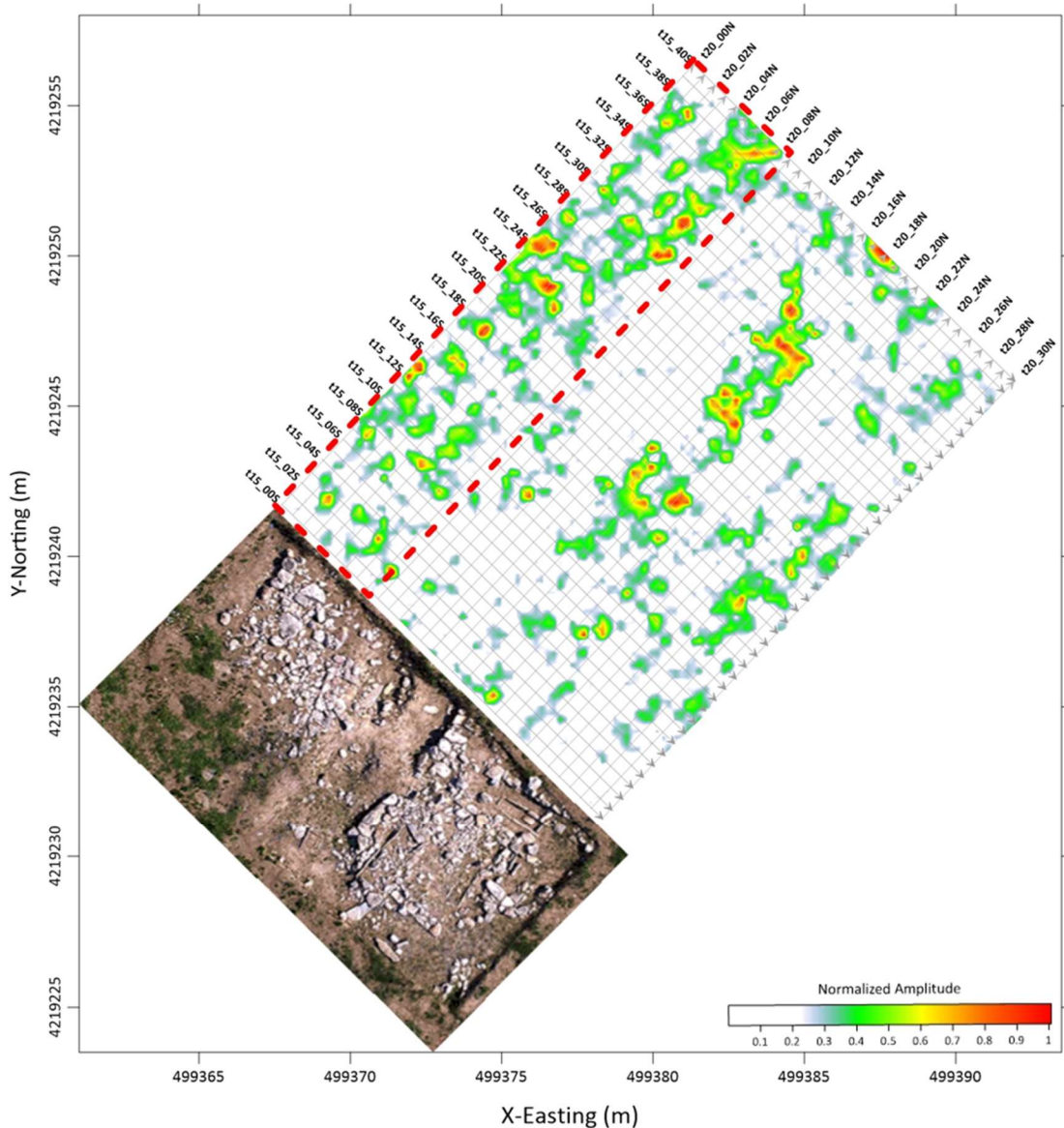


*Figure 5. 8: 50-60cm Volume-depth slice. The area outlined in a red dashed line (area 2) represents an area of interest, also depicted in the fence diagrams.*

In conclusion, the GPR method is a useful technique for archaeological surveys due to its non-invasive nature. Provided that a dense grid with a small transect separation is designed, the resolution of the data can be quite accurate. Depending on the time given to conduct a study at an archaeological site, the best data acquisition is done with transect separation of 0.50m and less and if possible in two directions, perpendicular to each other, to create a cross-sectioned grid. This is also the most time-consuming process. If less time is at hand, the transect separation must remain the same, but the GPR lines could be recorded in one direction, selected to cross targets perpendicularly, in order to acquire a more accurate location.

Nevertheless, the ground-penetrating radar survey by itself does not always present reliable results. It is usually applied using different center frequency antennas, to examine different

depths, in combination with other non-destructive geophysical methods such as the Electrical Resistivity Tomography (ERT).

In this study case many anomalies were observed that present a linear shape coinciding with the wall formations from the excavation. Area 1 and area 2 present the most concentrated anomalies and are therefore the suggested areas for expanding the excavation.

## References

- Annan, P., 2009. Electromagnetic principles of ground penetrating radar. In: H. M. Jol ed. *Ground Penetrating Radar Theory and Applications*, Oxford: Elsevier Science Limited. pp. 3-40.
- Annan, P., 2003. Ground penetrating radar: Principles, procedures & applications, Sensors & Software Inc., Technical Paper.
- Arcone, S., 2009. Glaciers and ice sheets. In: H. M. Jol ed. *Ground Penetrating Radar Theory and Applications*, Oxford: Elsevier Science Limited. pp. 361-392.
- Bailey, J.T., Evans, S. and Robin G. de Q., 1964. Radio echo sounding in polar ice sheets: *Nature*, Vol. 204, No. 4957, pp 420-421.
- Benedetto, A., Tosti, F., Ciampoli, L. B. and D'Amico, F., 2017. An overview of ground-penetrating radar signal processing techniques for road inspections, *Signal Processing*, Volume 132, pp. 201-209. <https://doi.org/10.1016/j.sigpro.2016.05.016>
- Bentley, C.R., 1964. The structure of Antarctica and its ice cover: *Research in Geophysics*, Vol. 2: Solid Earth and Interface Phenomena, Cambridge Mass., Technology Press of Massachusetts Institute of Technology, pp. 335-389.
- Bodechtel, J. and Papadeas, G., 1968. Tectonic aerial interpretation in the Mediterranean region exemplified by the metamorphic series at eastern Greece, near Marathon, *Photogrammetria*, 26, pp. 201-210.
- Bristow, C., 2009. Ground penetrating radar in aeolian dune sands. In: Harry M. Jol (ed.) *Ground Penetrating Radar Theory and Applications*, Oxford: Elsevier Science Limited. pp. 247–297
- Buynevich, I., Jol, H. M. and FitzGerald, D., 2009. Coastal environments. In: Harry M. Jol (ed.) *Ground Penetrating Radar Theory and Applications*, Oxford: Elsevier Science Limited. pp. 299-322.
- Conyers, L. B., 2004. Ground-penetrating radar for archaeology, Walnut Creek, California: AltaMira Press.
- Conyers, L. B., 2016. Ground-penetrating radar for geoarchaeology, Wiley Blackwell, 147pp (can be found at: <https://onlinelibrary.wiley.com/doi/book/10.1002/9781118949993>)
- Davis, J.L. and Annan, P., 1989. Ground penetrating radar for high-resolution mapping of soil and rock stratigraphy. *Geophysical Prospecting*, Vol. 37, pp. 531–551.
- Dojack, L., 2012. Ground Penetrating Radar Theory, Data Collection, Processing, and Interpretation: A Guide for Archaeologists. Graduate Research [Non-Thesis], <http://dx.doi.org/10.14288/1.0086065>
- Dolphin, L.T., et al., 1978. Radar Probing of Victorio Peak, New Mexico: *Geophysics*, Vol. 43, No. 7, pp. 1441-1448.

Doolittle, J., Butnor, J., 2009. Soils, peatlands and biomonitoring. In: H. M. Jol ed. *Ground Penetrating Radar Theory and Applications*, Oxford: Elsevier Science Limited. pp. 179-202.

El Said, M.A.H., 1956, Geophysical prospection of underground water in the desert by means of electromagnetic interference fringes, *Pro. I.R.E.*, Volume 44, pp. 24-30 and 940.

Goodman, D. and Piro, S., 2013. *GPR remote sensing in archaeology*. Heidelberg, Berlin: Springer-Verlag.

Goodman, D., Piro, S., Nishimura, Y., Schneider, K., Hongo, H., Higashi, N., Steinberg, J. and Damiata, B., 2009. GPR Archaeometry. In: H. M. Jol ed. *Ground Penetrating Radar Theory and Applications*, Oxford: Elsevier Science Limited. pp. 479-508

Lozios, S., 1993. Tectonic analysis of the metamorphic rocks in NE Attica. Unpublished PhD Thesis. Department of Geology. National and Kapodistrian University of Athens, 299pp. (in Greek)

Morey, R.M., 1974. Continuous Subsurface Profiling by Impulse Radar: Proceedings of Engineering Foundations Conference on Subsurface Exploration for Underground Excavations and Heavy Construction, Henniker, N.H. pp. 213-232.

Neubauer, W., Eder-Hinterleitner, A., Seren, S., Melichar, P., 2002. Georadar in the Roman civil town Carnuntum, Austria: An approach for archaeological interpretation of GPR data, *Archaeological Prospection*, Volume 9. pp. 135-156 (can be found at: <https://onlinelibrary.wiley.com/doi/pdf/10.1002/arp.183>)

Orlando, L., 2007. Georadar data collection, anomaly shape and archaeological interpretation— a case study from Central Italy, *Archaeological Prospection*, Volume 14. pp. 213-225 (can be found at: <https://onlinelibrary.wiley.com/doi/pdf/10.1002/arp.311>)

Redman, J., 2009. Contaminant mapping. In: H. M. Jol ed. *Ground Penetrating Radar Theory and Applications*, Oxford: Elsevier Science Limited. pp. 247-269.

Saarenketo, T., 2009. NDT transportation. In: H. M. Jol ed. *Ground Penetrating Radar Theory and Applications*, Oxford: Elsevier Science Limited. pp. 396-444.

Sandmeier, K.J. Introduction to the processing of GPR-data within REFLEXW, Sandmeier geophysical software, REFLEXW guide (can be found at: [https://www.sandmeier-geo.de/Download/gpr\\_2d\\_import\\_processing.pdf](https://www.sandmeier-geo.de/Download/gpr_2d_import_processing.pdf))

Slater, L. and Xavier, C., 2009. The contribution in ground penetrating radar to water resource research. In: H. M. Jol ed. *Ground Penetrating Radar Theory and Applications*, Oxford: Elsevier Science Limited. pp. 203-246.

Utsi, E.C., 2017. *Ground Penetrating Radar*, Oxford: Butterworth-Heinemann. 224 pp, <https://doi.org/10.1016/B978-0-08-102216-0.00016-3>

Waite, A.H. and Schmidt, S.J., 1961. Gross errors in height indication from pulsed radar altimeters operating over thick ice or snow, *IRE International Convention Record*, Part 5, pp. 38-54.

Walford, M.E.R., 1964. Radio echo sounding through an ice shelf: *Nature*, Vol. 204, No. 4956, pp. 317-319.

Yarovoy, A., 2009. Landmine and unexploded ordnance detection and classification with ground penetrating radar. In: H. M. Jol ed. *Ground Penetrating Radar Theory and Applications*, Oxford: Elsevier Science Limited. pp. 445-478.

## Additional Bibliography

Angelis, D., Tsourlos, P., Tsokas, G., Vargemezis, G., Zacharopoulou, G. and Power, C., 2018. Combined application of GPR and ERT for the assessment of a wall structure at the Heptapyrgion fortress (Thessaloniki, Greece), *Journal of Applied Geophysics*, Volume 152, pp. 208-220. <https://doi.org/10.1016/j.jappgeo.2018.04.003>.

Barone, P. M., Ruffel, A., Tsokas, G. and Rizzo, E., 2019. Geophysical Surveys for Archaeology and Cultural Heritage Preservation, *Heritage*. <https://doi:10.3390/heritage2040174>

Ninje, D. J., 2017. Treatment, processing and interpretation of GPR data acquired from the archeological site of Castro de Ul, northern Portugal. MSc Thesis. University of Porto.

Ortega-Ramírez, J., Bano, M., Cordero-Arce, M.T., Villa-Alvarado, L.A. and Chavez-Fraga, C., 2020. Application of non-invasive geophysical methods (GPR and ERT) to locate the ancient foundations of the first cathedral of Puebla, Mexico. A case study, *Journal of Applied Geophysics*, Volume 174. <https://doi.org/10.1016/j.jappgeo.2020.103958>.

Sala, J. and Linford, N., 2012. Processing stepped frequency continuous wave GPR systems to obtain maximum value from archaeological data sets, *Near Surface Geophysics*, 10, 3-10. <https://doi:10.3997/1873-0604.2011046>

Schultz, J.J. and Martin, M.M., 2011. Controlled GPR grave research: Comparison of reflection profiles between 500 and 250 MHz antennae, *Forensic Science International*, 209, pp. 64-69. <https://doi.org/10.1016/j.forsciint.2010.12.012>

Souglakos, N., 2019. Detailed geophysical survey at the university's archaeological excavation, Marathon, Attica (Plasi site). MSc Thesis. National and Kapodistrian University of Athens.

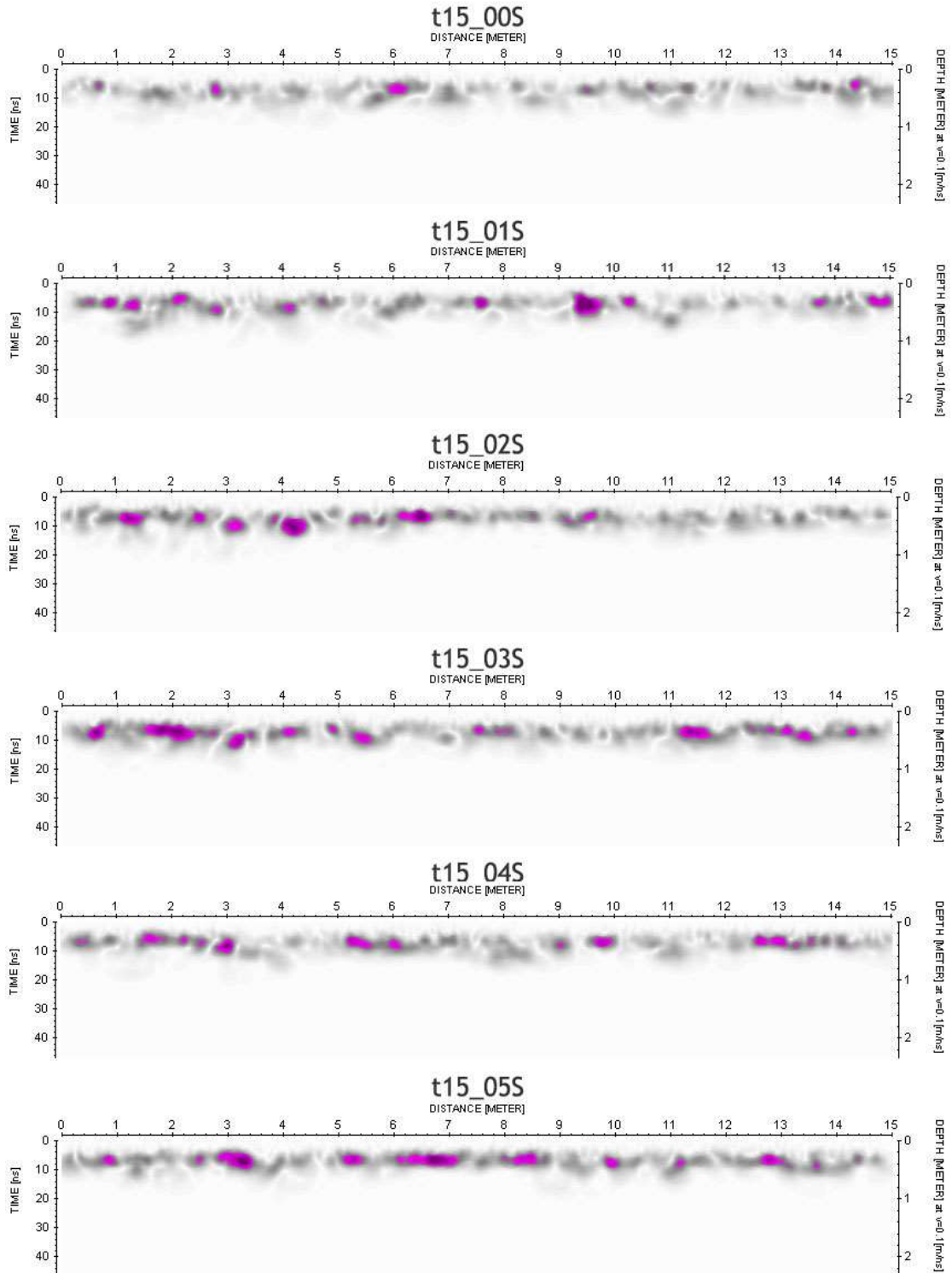
Yilmaz, S., Balkaya, Ç., Çakmak, O. and Oksum, E., 2019. GPR and ERT explorations at the archaeological site of Kılıç village (Isparta, SW Turkey), *Journal of Applied Geophysics*, Volume 170, Article 103859. <https://doi.org/10.1016/j.jappgeo.2019.103859>

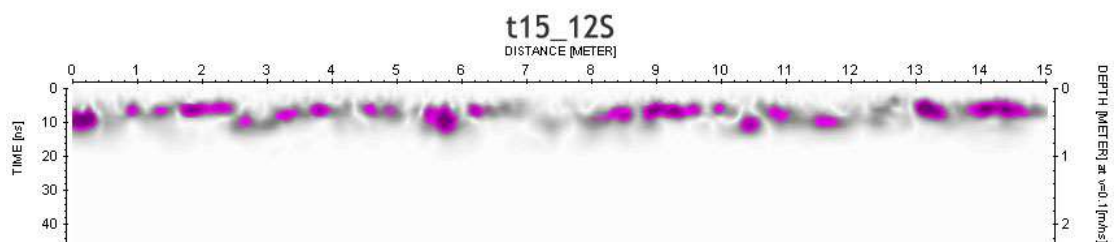
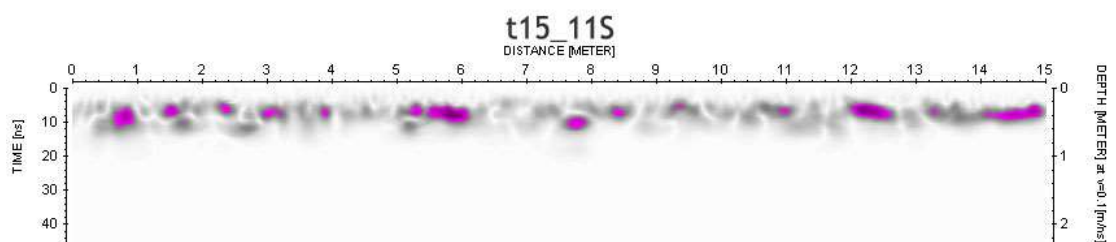
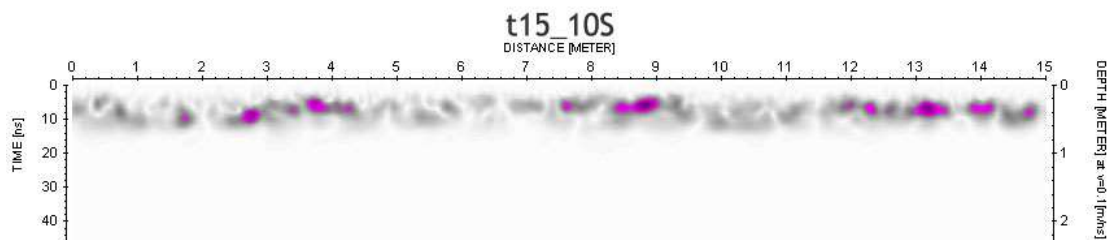
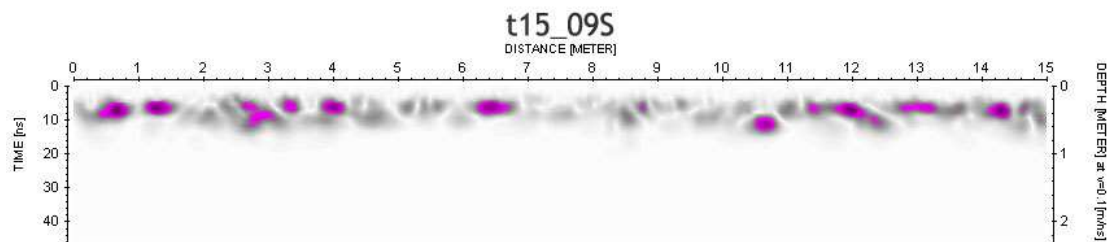
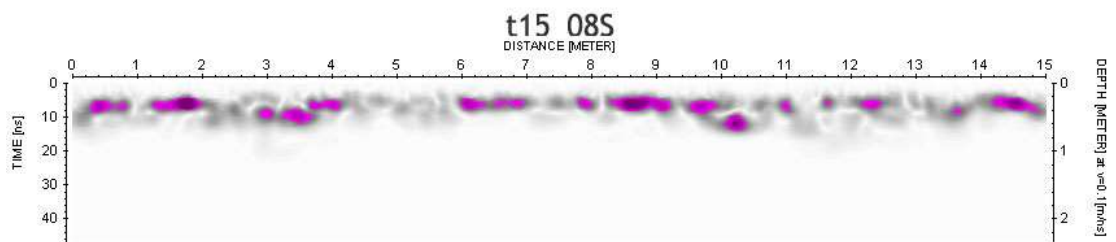
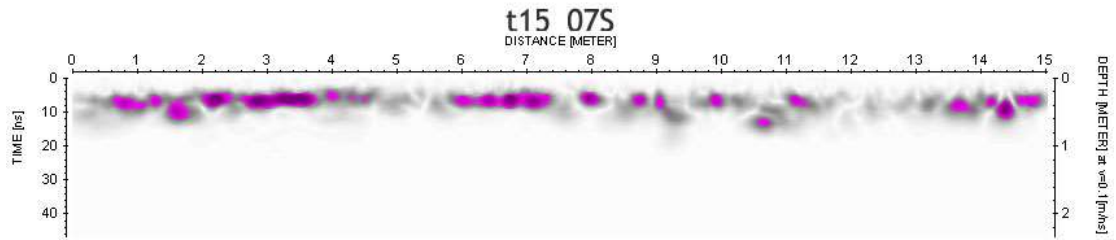
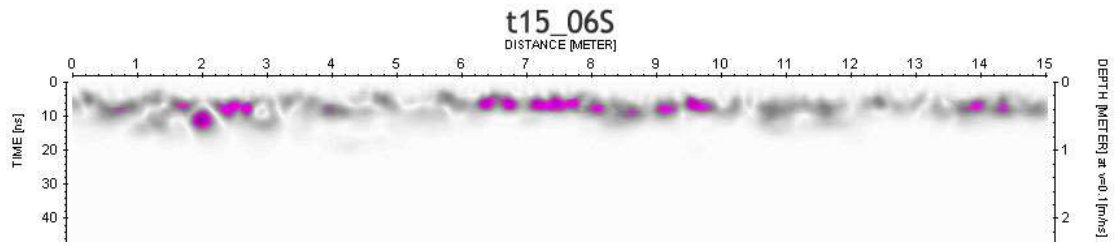
Zhao, W., Forte, E., Fontana, F., Pipan, M. and Tian, G., 2018. GPR imaging and characterization of ancient Roman ruins in the Aquileia Archaeological Park, NE Italy, *Measurement*, Volume 113, pp. 161-171. <https://doi.org/10.1016/j.measurement.2017.09.004>

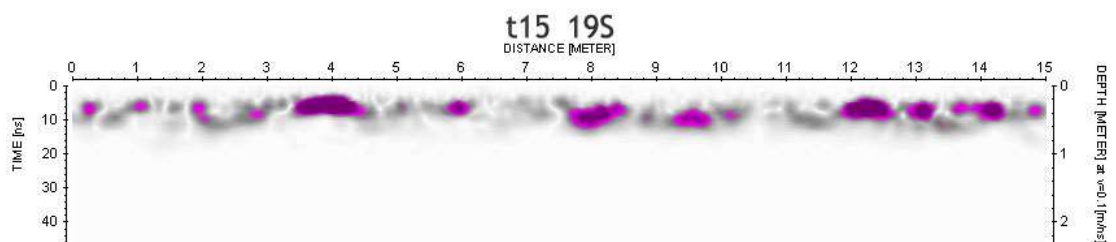
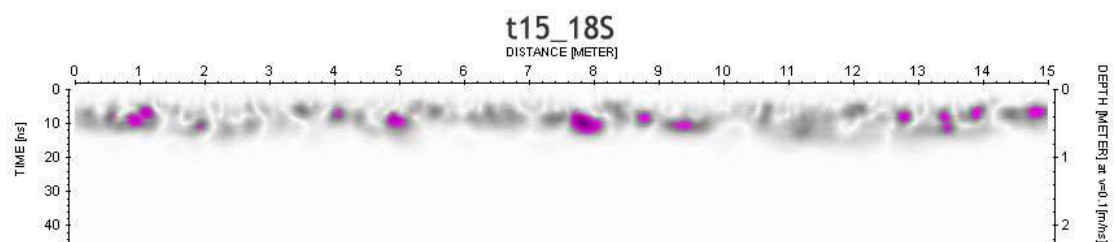
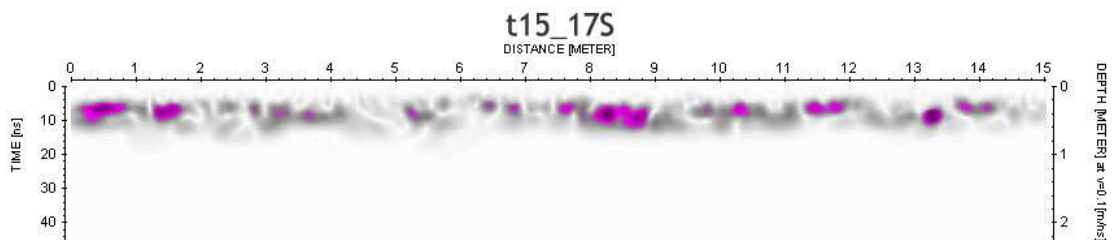
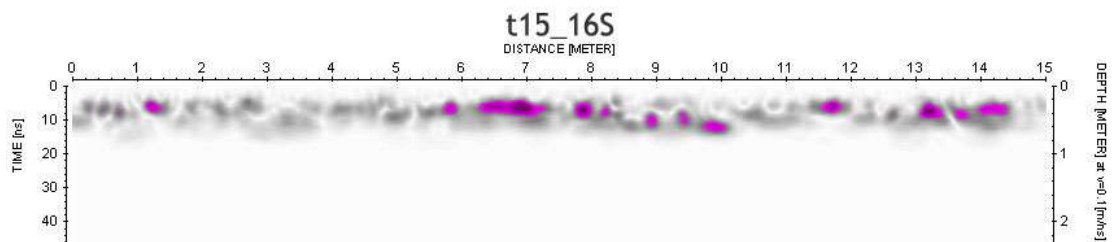
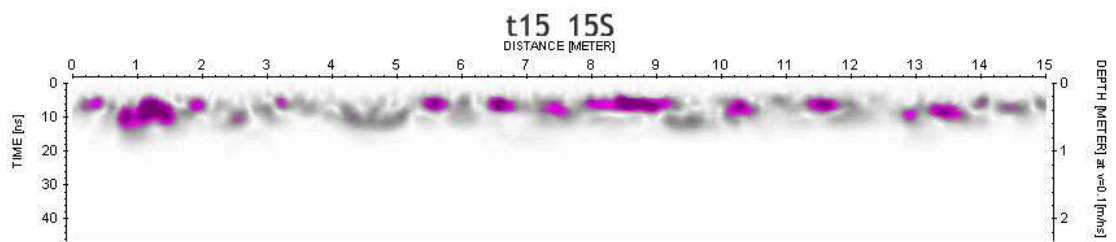
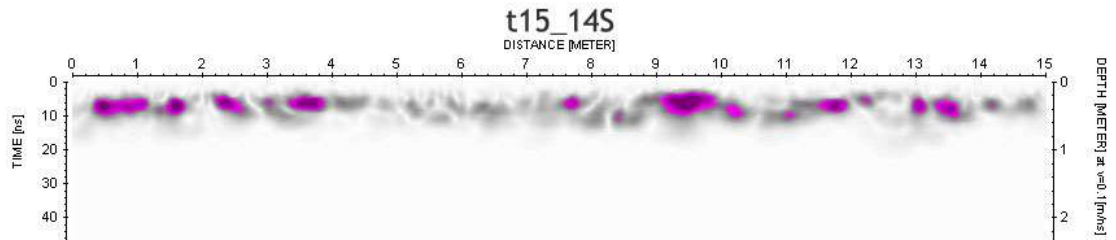
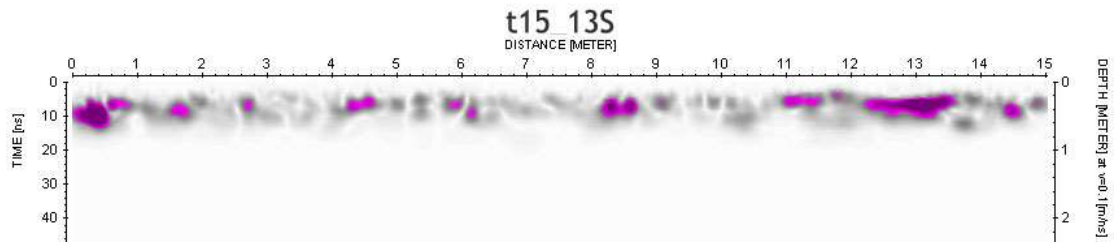
Zhao, W., Forte, E., Pipan, M. and Tian, G., 2013. Ground Penetrating Radar (GPR) attribute analysis for archeological prospection, *Journal of Applied Geophysics*, 97, pp. 107-117. <http://dx.doi.org/10.1016/j.jappgeo.2013.04.010>

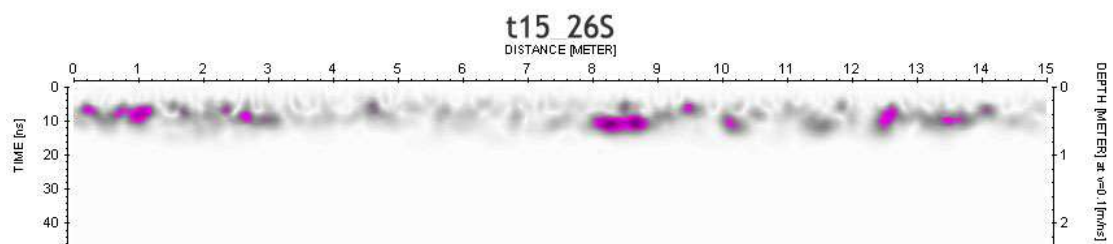
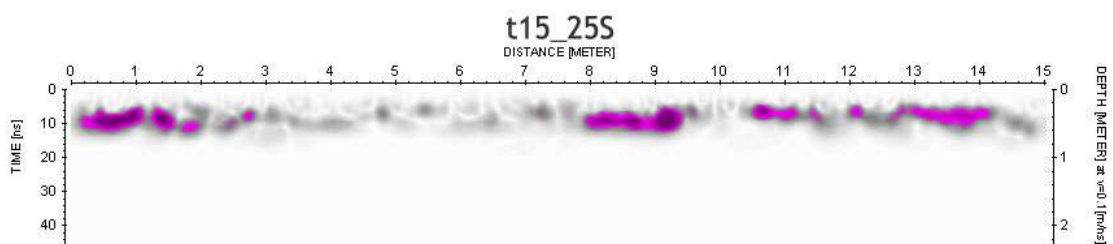
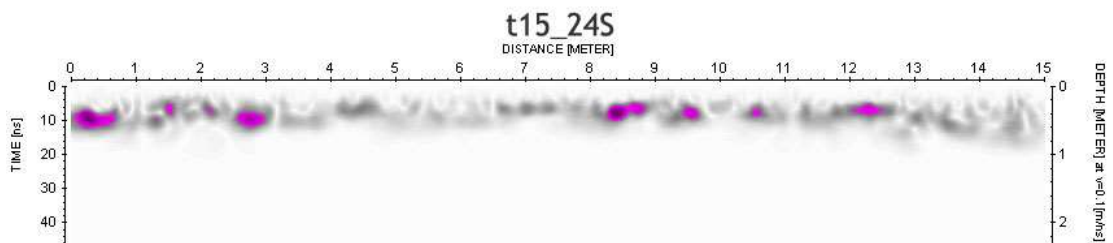
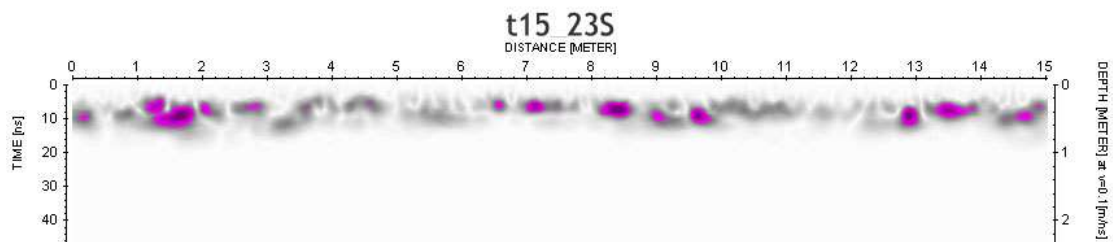
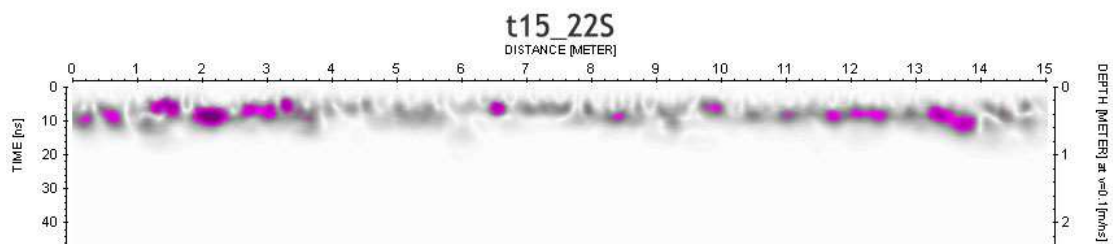
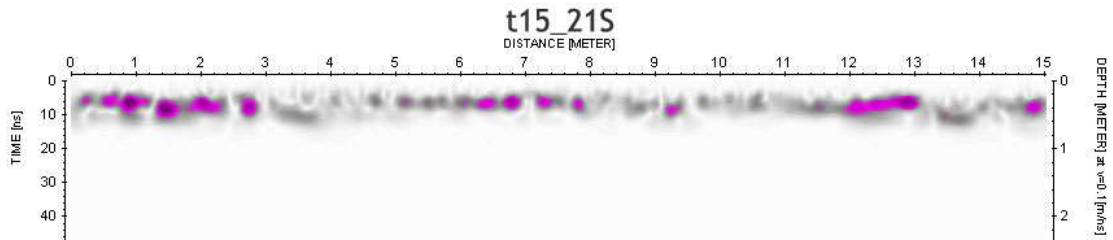
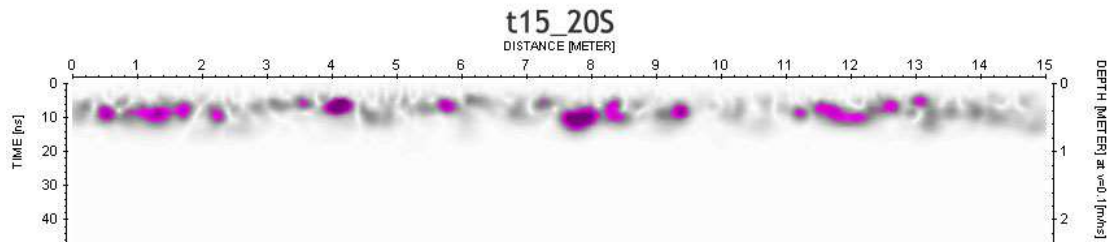
Zhao, W., Forte, E., Levi, S.T., Pipan, M. and Tian, G., 2015. Improved high-resolution GPR imaging and characterization of prehistoric archaeological features by means of attribute analysis, *Journal of Archaeological Science*, Volume 54, pp. 77-85. <https://doi.org/10.1016/j.jas.2014.11.033>.

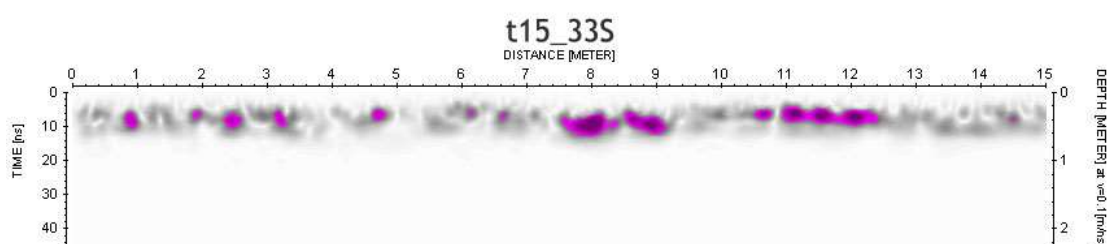
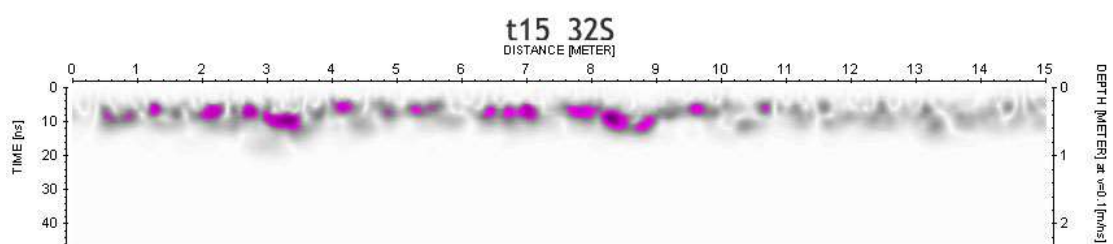
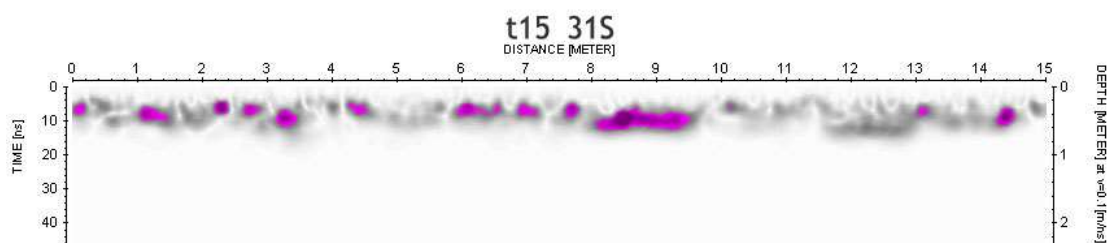
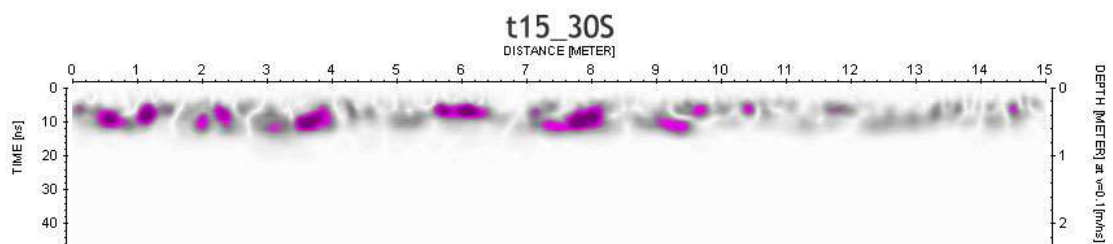
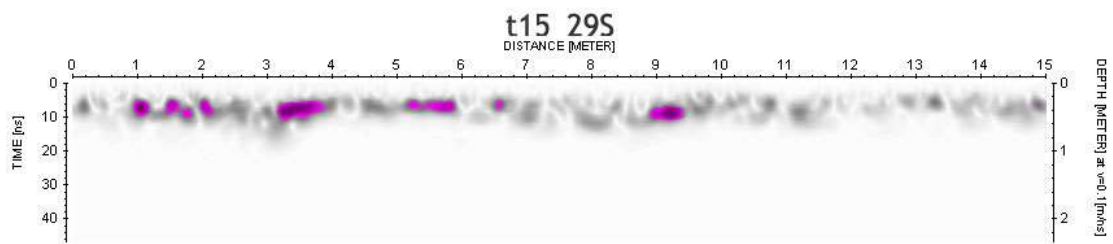
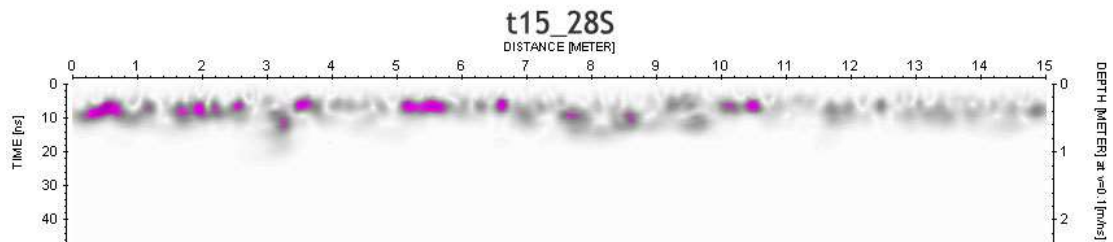
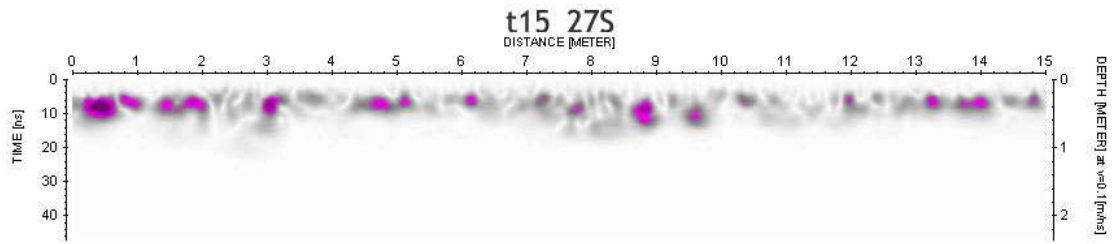
# Appendix

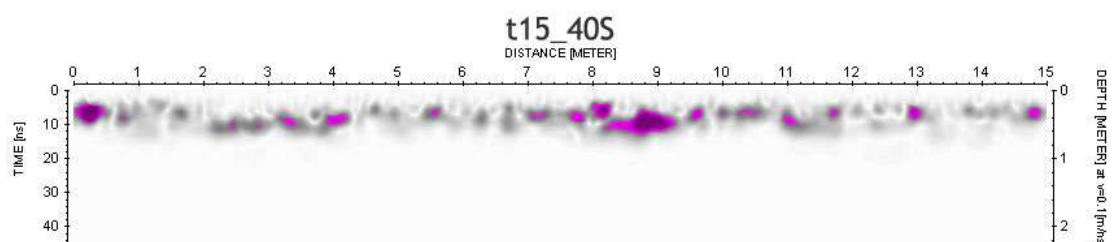
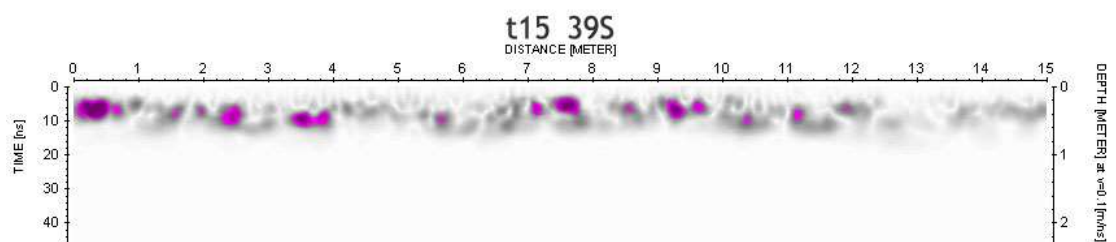
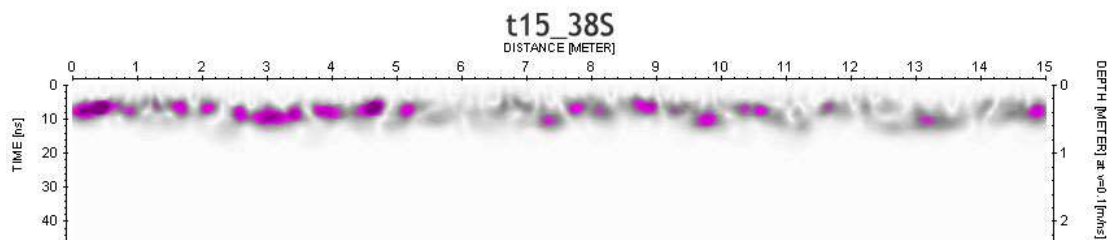
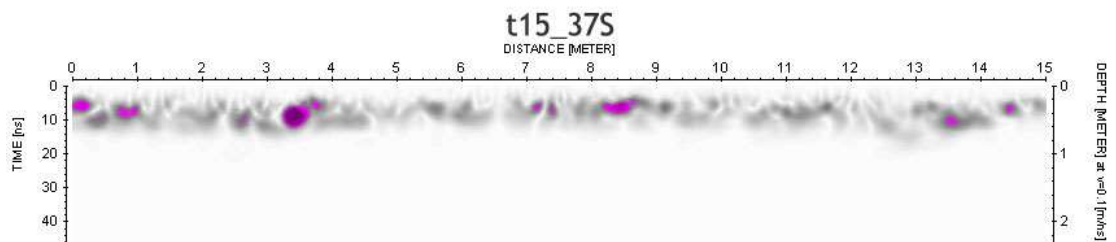
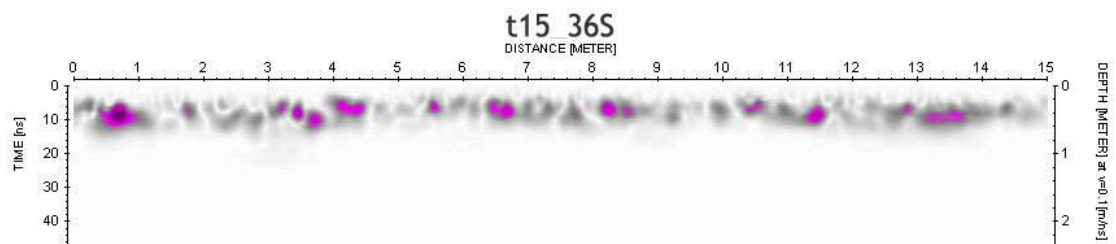
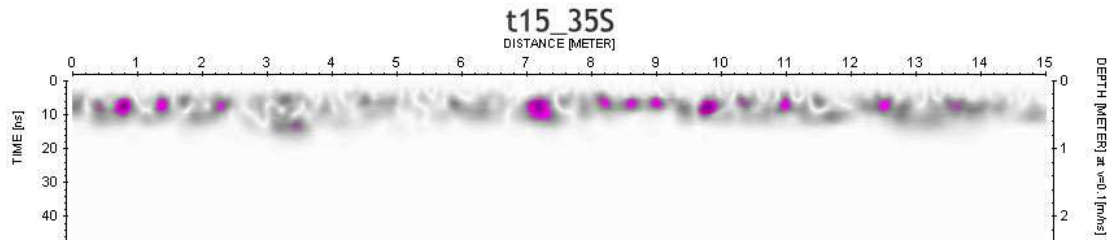
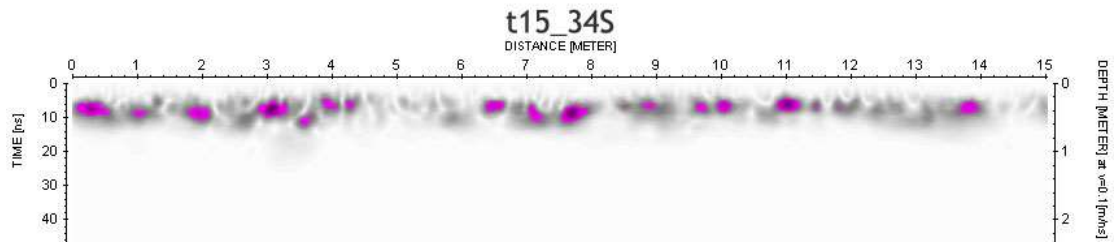


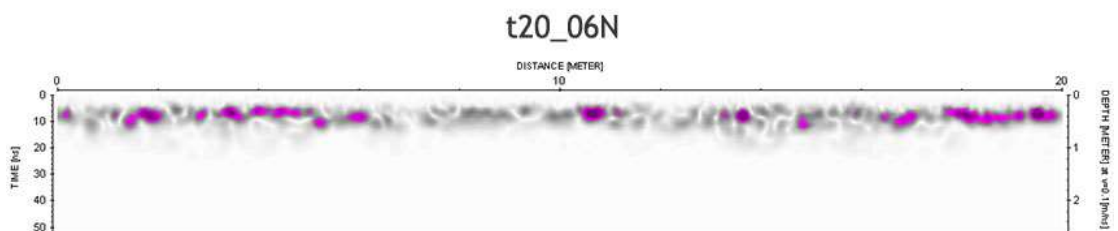
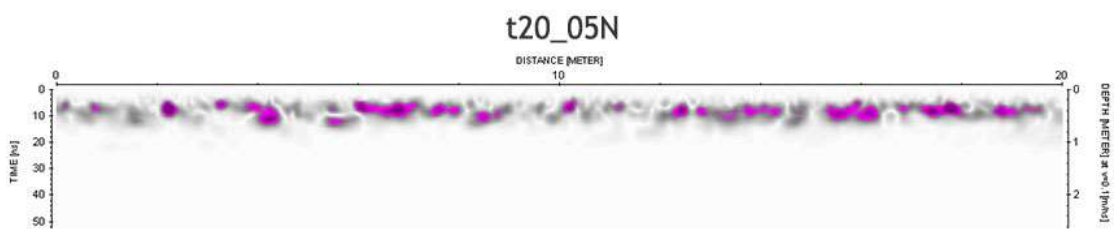
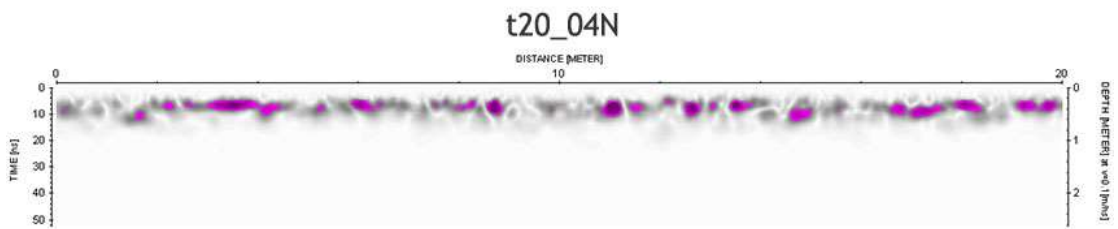
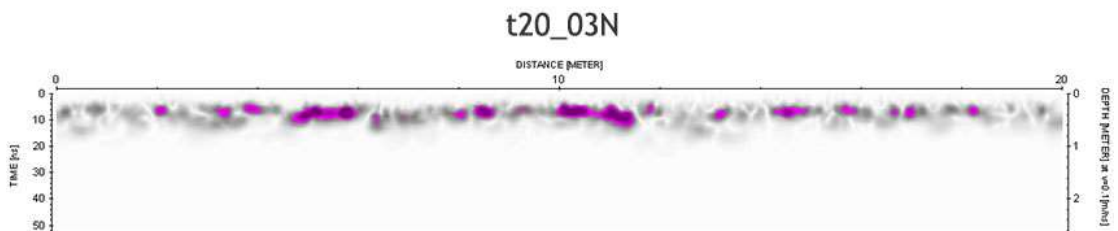
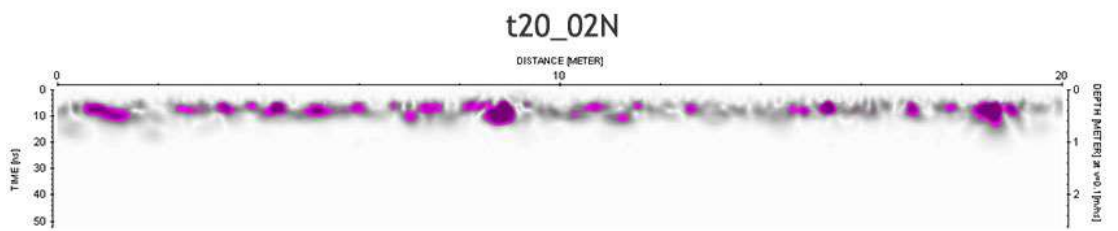
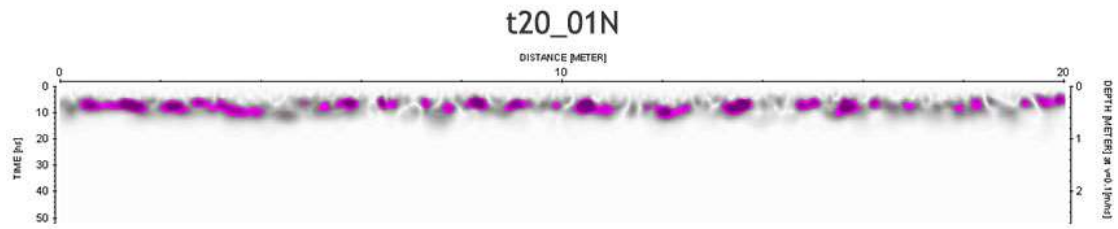
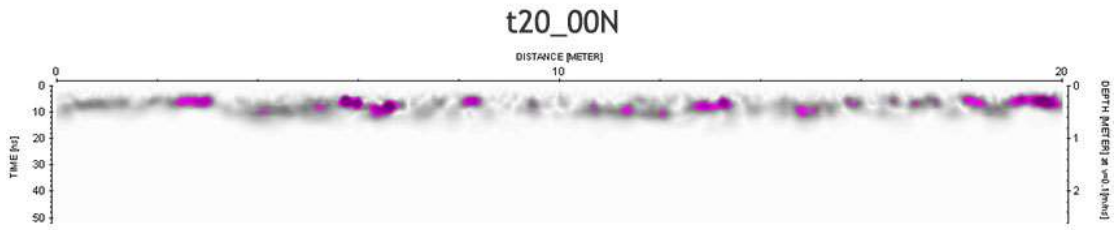




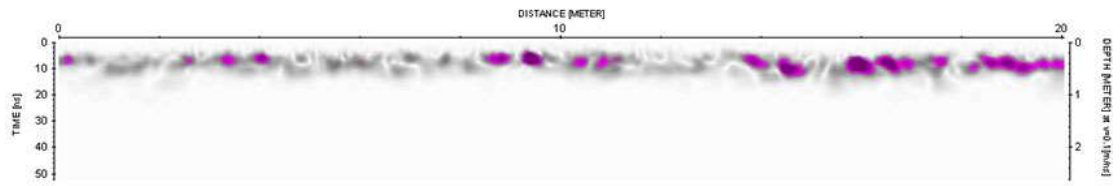




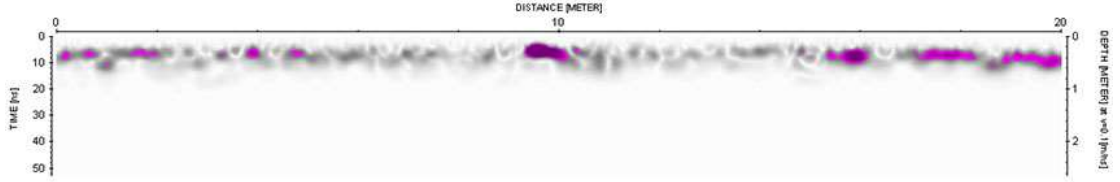




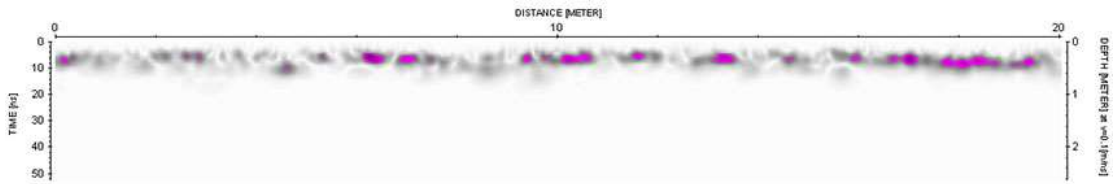
t20\_07N



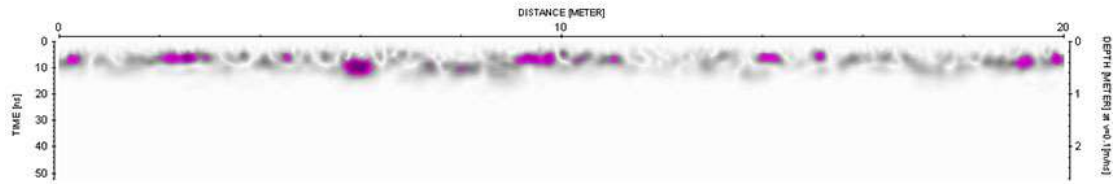
t20\_08N



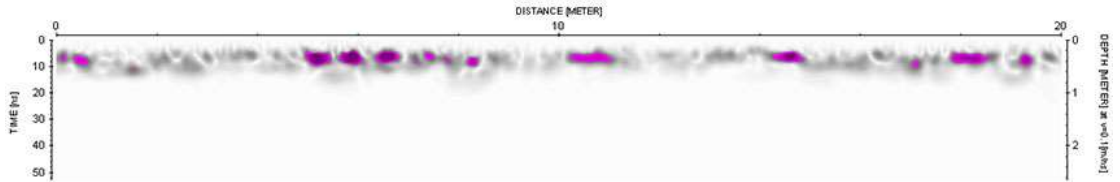
t20\_09N



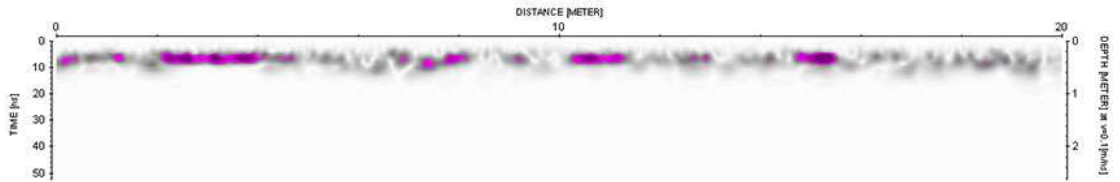
t20\_10N



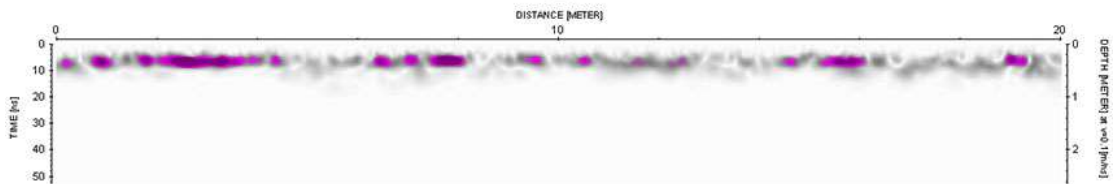
t20\_11N

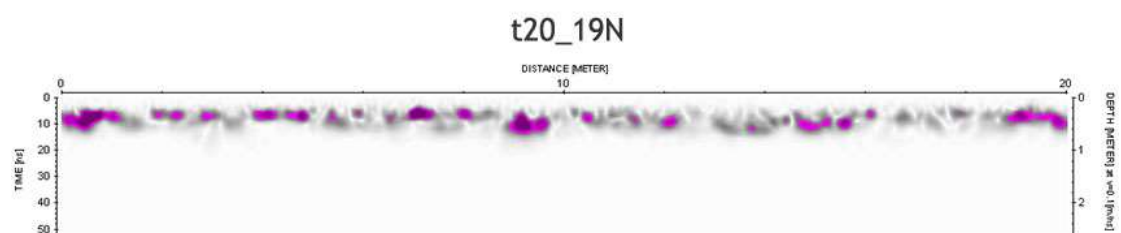
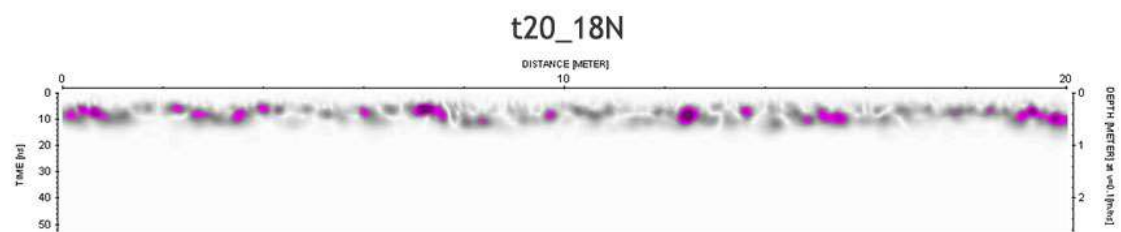
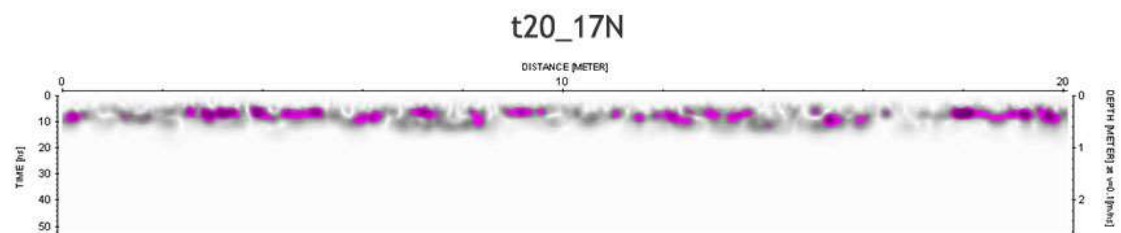
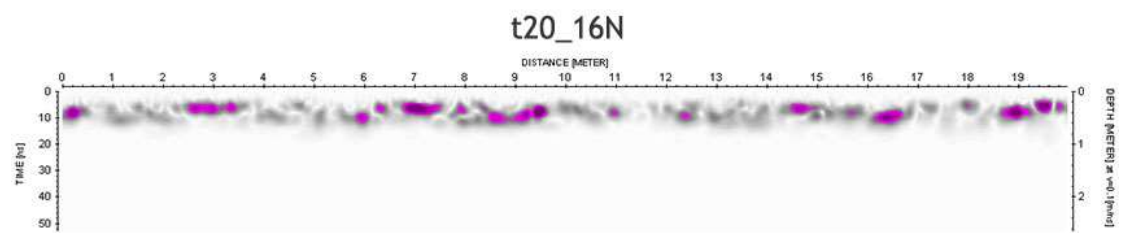
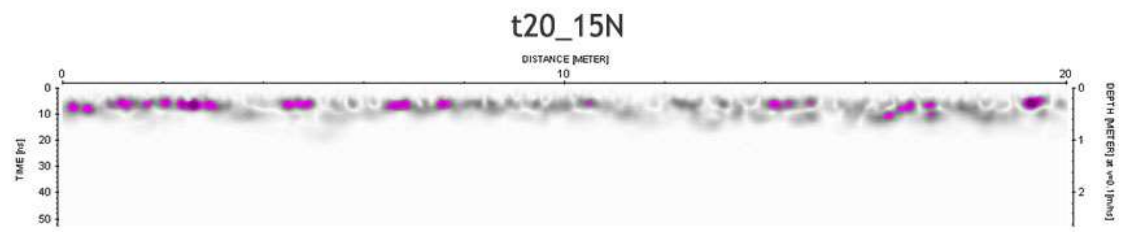
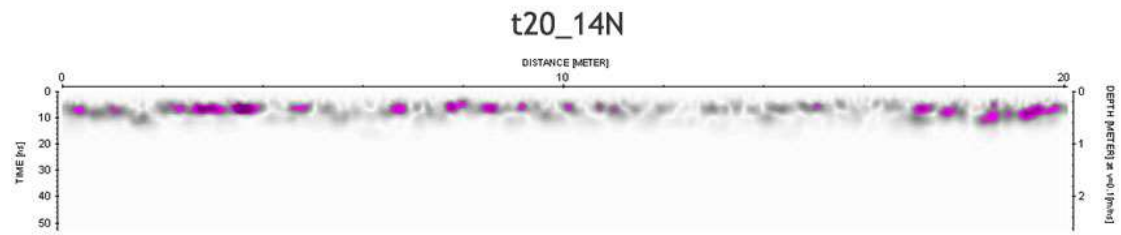


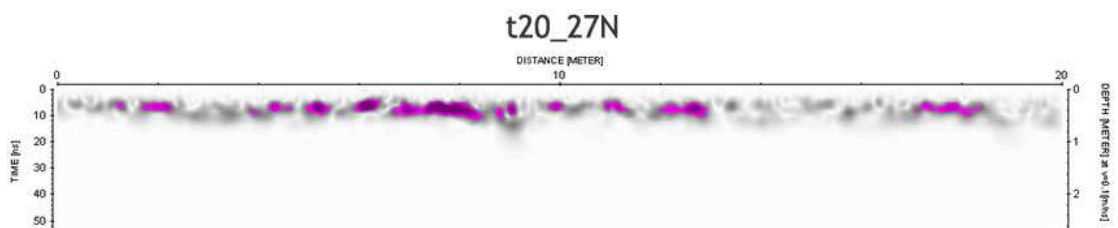
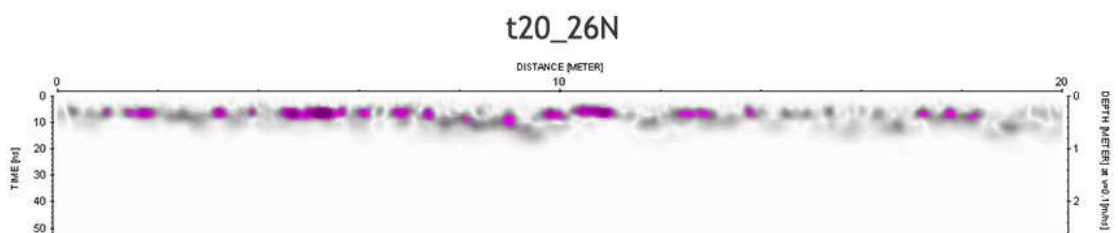
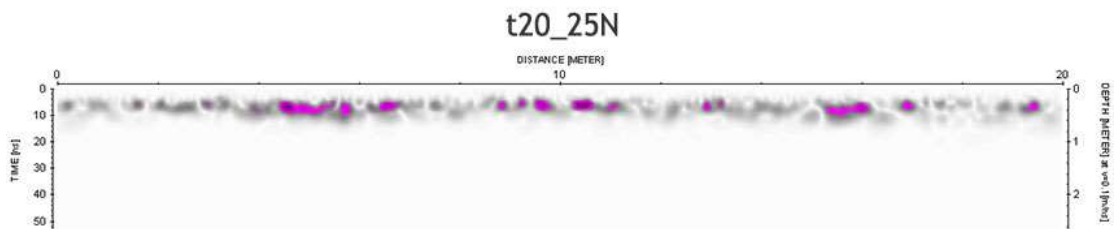
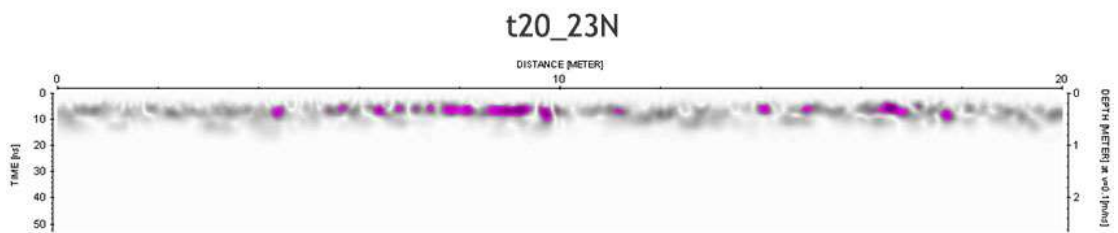
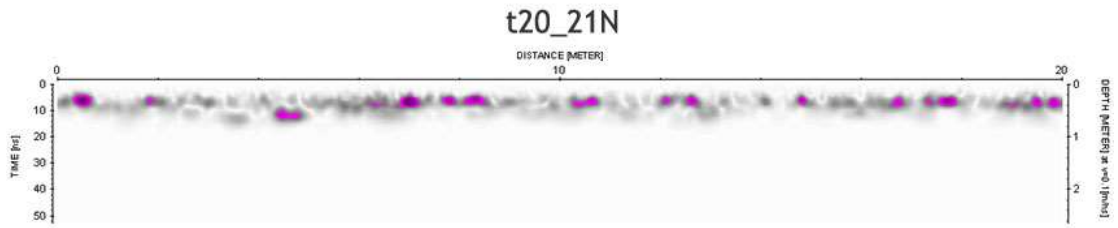
t20\_12N



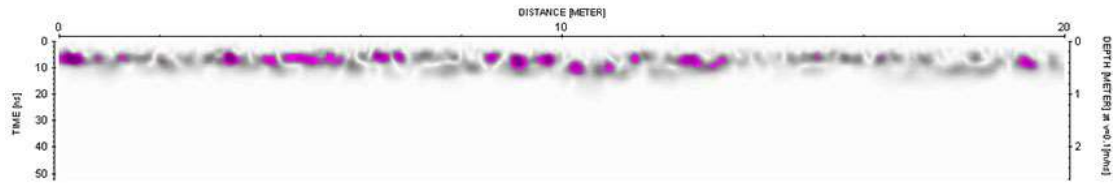
t20\_13N



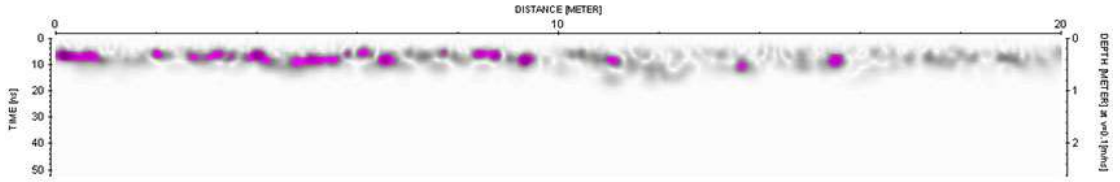




t20\_28N



t20\_29N



t20\_30N

